



Universiteit Utrecht



UTRECHT UNIVERSITY

INSTITUTE FOR THEORETICAL PHYSICS

MASTER'S THESIS

---

# Thermodynamic signatures of topological phases

---

*“If someone points out to you that your pet theory of the universe is in disagreement with Maxwells equations – then so much the worse for Maxwells equations. If it is found to be contradicted by observation – well these experimentalists do bungle things sometimes. But if your theory is found to be against the second law of thermodynamics I can give you no hope; there is nothing for it but to collapse in deepest humiliation.”*

Sir Arthur Stanley Eddington (1927)

*Author:*

Sander KEMPKE

3473554

*Supervisors:*

Prof. Dr. Cristiane

MORAIS SMITH

Anton QUELLE, M.Sc.

June 30, 2016

---

## Abstract

For a long time, it was believed that the Ginzburg-Landau formalism was able to classify all different types of phase transitions [1, 2]. This view changed with the discovery of the quantum Hall effect [3] and topological insulators [4]. Topological insulators (superconductors) are materials that host symmetry-protected metallic edge states in an insulating (superconducting) bulk [5, 6]. Although topological insulators are well understood by now, a thermodynamic description of their behavior remained elusive, firstly because the edges are lost in the thermodynamic limit, when the system size goes to infinity, and secondly because topological quantum field theories involve non-local order parameters, and hence cannot be captured by the conventional Ginzburg-Landau formalism. Recently, this challenge has been overcome: by using Hill thermodynamics [7] to describe the paradigmatic Bernevig-Hughes-Zhang model in two dimensions, it has been shown that at the topological phase change the thermodynamic potential does not scale extensively due to the boundary effects [8]. Here, we extend this thermodynamic approach firstly to the Kitaev chain in one-dimension and then to different topological models in various dimensions (the Su-Schrieffer-Heeger model in one dimension, the Kane-Mele model in two dimensions and the Bernevig-Hughes-Zhang model in three dimensions) at zero temperature. Surprisingly, we find that all these models exhibit the same universal behavior in the order of the topological-phase transition, which depends on the dimensionality of the system. Next, we use this thermodynamic approach to describe topological phases at finite-temperatures. We calculate the entropy and heat capacity for the Kitaev chain and verify its behavior in comparison with conformal field theory. Furthermore, we extend the topological phase transition to finite-temperatures, by numerically deriving the topological phase diagram for the bulk of the system, and show that it displays a good agreement with the one calculated analytically from the Uhlmann phase. Finally, we calculate measurable quantities such as the density of states and the heat capacity for different topological insulators. Our work reveals unexpected universalities and opens the path to a thermodynamic description of systems with a non-local order parameter, provided that nonlinear terms are appropriately taken into account for the thermodynamic extensive variables.

---

## Preface

In front of you lies the Master's thesis titled "Thermodynamic signatures of topological phases", written to obtain the degree Master of Science. In the past year, I have worked on this project together with my supervisors Anton Quelle and Cristiane Morais Smith and I am very happy that I have chosen this project. In our first meeting, Anton was already able to inspire me with his knowledge in physics and his eagerness to start the project. Together with the unstoppable enthusiasm and excellent guidance of Cristiane, I knew this was going to be an interesting project. Especially the particular way in which thermodynamics is applied on finite-size systems got my attention, and although I did not know a lot about topological materials, I am glad to have had the opportunity to study these materials for the past months and got to understand them better and better.

Like any physics student, I was already acquainted with thermodynamics. I started my student career in Science & Innovation Management, where I was introduced to the intriguing concept of entropy in the course Physical Chemistry. Entropy, as the teacher of this course, Andrew Bale, described it, can be explained in two ways. To start with, it can be thought of as (1) the amount of chaos in the only closed system we will ever know: the universe. Or it can be seen as (2) when I leave my child in his bedroom and come back after five minutes. Unfortunately, this was the only course where I could encounter this fascinating concept of entropy in Science & Innovation Management, and therefore I started to study Physics & Astronomy as well, perhaps one of the best decisions in my life. In my Bachelor's project, I investigated the thermodynamics of "Blue energy", and due to these interesting projects and the challenging subjects, I continued my Master in theoretical physics.

I am very glad that I was able to use my knowledge about thermodynamics in this Master's project. However, this time, thermodynamics was put in a very different perspective than I was used to, because the finite-size becomes important for topological materials. Therefore, perhaps one of the most interesting parts of this thesis is how to describe topologically protected edge states within a thermodynamic framework. Thermodynamics in principle does not know about topology, but, when the boundaries are appropriately taken into account, it turns out that thermodynamics is able to capture the correct behavior.

As usual in research, the answers to the initial questions only give rise to more questions and new ideas. Currently, we are working on projects to connect the described framework to conformal field theories and topological entanglement entropy in order to verify our results and to better understand the concepts at stake. I am excited that I have the opportunity to continue to work on these questions in the upcoming years, and, hopefully, this has not been my last effort in this field of research.

Sander Kempkes, 28-06-2016

# Contents

<b>1</b>	<b>Introduction</b>	<b>5</b>
<b>2</b>	<b>Topological materials and experiments</b>	<b>9</b>
2.1	Topological Materials . . . . .	10
2.1.1	Quantum Hall effect and quantum spin Hall effect . . . . .	10
2.1.2	An example: the Kitaev chain . . . . .	16
2.1.3	Topological invariants . . . . .	28
2.1.4	Topological insulators in 2D . . . . .	29
2.1.5	Topological insulators in 3D . . . . .	35
2.1.6	The tenfold way . . . . .	37
2.2	Experiments on topological materials . . . . .	40
2.2.1	Scanning Tunneling Microscopy (STM) . . . . .	40
2.2.2	Transport . . . . .	46
2.2.3	Angle-Resolved PhotoEmission Spectroscopy (ARPES) . . . . .	48
2.3	Conclusion . . . . .	52
<b>3</b>	<b>Hill thermodynamics: thermodynamics of finite-size systems</b>	<b>54</b>
3.1	Theories of phase transitions . . . . .	56
3.1.1	Ehrenfest classification . . . . .	56
3.1.2	Landau theory of symmetry breaking . . . . .	59
3.1.3	Quantum and topological phase transitions . . . . .	62
3.2	Hill thermodynamics . . . . .	66
3.2.1	Gibbs thermodynamics . . . . .	67
3.3	Thermodynamics and statistical physics . . . . .	68
3.4	The topological phase transition for the Kitaev chain . . . . .	69
3.5	Conclusion . . . . .	71
<b>4</b>	<b>Classification of topological phase transitions: universalities</b>	<b>73</b>
4.1	One dimension . . . . .	73
4.1.1	Su-Schrieffer-Heeger model . . . . .	73
4.2	Two dimensions . . . . .	74
4.2.1	Kane-Mele model . . . . .	74
4.2.2	Bernevig-Hughes-Zhang model . . . . .	75
4.3	Three dimensions . . . . .	77
4.3.1	Bernevig-Hughes-Zhang model . . . . .	77
4.4	Conclusion . . . . .	77

<b>5</b>	<b>Finite-temperature effects</b>	<b>79</b>
5.1	Finite-temperature effects in the Kitaev chain . . . . .	79
5.1.1	Entropy and heat capacity . . . . .	79
5.1.2	Finite-temperature phase diagram . . . . .	81
5.2	Heat capacity and density of states . . . . .	85
5.2.1	The Bernevig-Hughes-Zhang model in two dimensions . . . . .	85
5.2.2	The Kane-Mele model in two dimensions . . . . .	86
5.3	Conclusion . . . . .	87
<b>6</b>	<b>Conclusion and discussion</b>	<b>89</b>
<b>7</b>	<b>Appendix</b>	<b>92</b>

# 1 Introduction

Thermodynamics has contributed greatly to our understanding of materials and their phase transitions. A phase transition describes how a material goes from one state of matter into another, such as when gas transforms into a liquid upon decreasing temperature. For a long time, the Ginzburg-Landau theory of symmetry breaking was believed to be able to describe all possible orders in materials and their phase transitions [1, 2]. This view changed with the discovery of the quantum Hall effect [3] and topological insulators [4], which opened up a whole new area of research into *topological phases*. The term topological phase designates a material with an insulating bulk and a metallic edges, which are protected by topology. This new kind of topological phase is richer than the usual quantum phase because the topology of a system comes into play together with quantum effects. Nowadays, topological systems, such as topological superconductors and topological insulators, are frequently investigated because of their interesting and exotic properties.

One of the most interesting properties of the topological phase is the difference between the bulk and the boundary of a system. For instance, topological insulators exhibit an insulating bulk, but metallic edge states, with quantized conductivity. The effect is driven by a strong spin orbit coupling, and was first predicted to occur in graphene [4] and later in HgTe/CdTe quantum wells [9]. Moreover, topological superconductors were predicted to host Majorana bound states at its edges, but not in the bulk [10], and these can be used as building blocks for quantum computing. Topological superconductors are usually created by putting a topological insulator on top a conventional superconductor, and inducing supercurrents via the proximity effect.

Some of these theoretical predictions have been verified by experiments. At the moment, three different techniques are used to identify topological phases, which are Scanning Tunneling Microscopy (STM), transport, and Angle-Resolved PhotoEmission Spectroscopy (ARPES). With the help of these methods, great contributions to the understanding of these materials have been made, such as the discovery of topological insulators and the quantum spin Hall effect by the group of Molenkamp in Würzburg [11], the experimental verification of topological insulators in three dimensions [12], the discovery of Majorana bound states in Delft [13] and, a recent hot topic in condensed matter, the discovery of Weyl fermions [14].

Although these experiments have proven their value in identifying topological phase transitions, it seems peculiar that it is not possible to describe these topological phases in the way we were used to describe phase transitions within thermodynamics. Thermodynamics is one of the most fundamental theories in physics, which is also reflected by the quote of Sir Arthur Stanley Eddington on the front page. Therefore, we should be able to describe this

---

type of topological phase transition in the conceptual framework of thermodynamics. However, this turns out not to be so easy. In example, in ordinary thermodynamics, it is possible to identify a phase transition by analyzing the pressure as a function of temperature of a material. The kink in the phase diagram indicates the point of the phase transition. This cannot be done for a topological phase change since these types of transitions do not seem to break any of the underlying symmetries. The Ginzburg-Landau classification breaks down, because it makes use of local order parameters, and topological insulators can only be described by non-local order parameters such as Chern numbers. Moreover, and more intuitively, it is not possible to simply use thermodynamics in describing topological-phase changes, because thermodynamics is about *infinitely* large systems, whereas topological-phase changes involve *finite-size* systems due to the presence of edge states.

However, Quelle et al. [8] recently proposed a solution to this conundrum: a thermodynamic description of topological states of matter, based on the thermodynamic approach developed by Hill [7] in the 1960s for finite-size systems. In this so-called Hill thermodynamics, one can split the contributions to the thermodynamic potential of a finite-size system into the “conventional” extensive potential for an infinite system and a non-extensive subdivision potential. The bulk contribution of the topological insulator corresponds to the conventional potential, whereas the boundary and finite-size contributions can be identified with the subdivision potential. To corroborate this new method, Quelle et al. were able to find thermodynamic signatures of topological phases in the paradigmatic 2D Bernevig-Hughes-Zhang model [9] model. In this way, a topological phase transition can be described in the same way as an ordinary phase transition and therefore it has the potential to be a major breakthrough in the field. The idea of this thesis is to apply this newly developed formalism to different models and to identify interesting thermodynamic phase-change signatures.

In this thesis, we analyze different topological models with this method, and in particular a paradigmatic one-dimensional (1D) superconductor: the Kitaev chain [10]. In 2001, Alexei Kitaev proposed a toy model, the Kitaev chain, in which he shows how a 1D quantum wire can host Majorana bound-states at the edge of the wire. A Majorana fermion is a fermion that is its own antiparticle. This implies a Majorana fermion cannot have any charge or energy. In his work, Kitaev analyses the 1D chain and finds two different topological phases, of which one hosts unbound Majoranas at the edges. Due to these unbound Majoranas and the coupling of the Majoranas at different sites, the system is unlikely to pick up an arbitrary phase. These Majorana bound states can therefore be used as qubits, and are the best-known candidate for the building blocks of quantum computers.

Although Majorana fermions have not been observed as an elementary particle (in the

Standard Model, only the neutrino might be a Majorana fermion, but this still has to be experimentally proven), Majorana bound states have recently been found in some superconducting materials as emerging quasiparticles [13]. In their experiment, Mourik et al. use a 1D indium antimonide nanowire contacted with one normal and one superconducting electrode and show, by using STM, that Majorana bound states emerge in this material. More specifically, when the system is exposed to an external magnetic field on the order of 100 miliTesla, the apparatus shows a mid-gap state with a peak in the electrical conductance at zero bias voltage. These mid-gap states are thought to be the bound Majorana states. The results of their experiments were quickly reproduced by other groups with similar devices [15, 16, 17, 18], but it remains difficult to undeniably prove the existence of these conjectured Majoranas because other explanations that do not involve Majoranas are available to account for these mid-gap states [19]. A new method to settle these discussions is thus required and therefore we have chosen to investigate the Kitaev chain as main model of interest with the thermodynamic method proposed by Quelle et al. [8].

Our first aim is thus to identify thermodynamic signatures of topological phases in the Kitaev chain. Although the Majorana bound-states have been experimentally identified [13], there might also exist thermodynamic signatures to detect the topological phase transitions in materials, and these thermodynamic signatures could turn out to be measured more easily than topological quantities. In order to develop such a method, we first need to understand topological phases in general and the Kitaev chain more specifically.

The second aim is to continue the search for thermodynamic signatures in different topological models and try to find connections between the types of phase transitions. The results show that we find *universal* behavior in the order of the phase transition. By separating the bulk and the edge state with Hill thermodynamics, we find a phase transition of order  $D$  at the edge and of order  $D + 1$  in the bulk, where  $D$  is the spatial dimension of the model.

The third aim is to extend this method towards finite-temperatures. Nowadays, the zero-temperature behavior of topological phases is rather well understood, but a proper description at finite-temperatures is not yet present. Therefore, we use Hill thermodynamics to obtain the thermodynamic potential at finite-temperature, and we show the entropy, heat capacity and finite-temperature topological phase diagram for the Kitaev chain. Furthermore, we calculate the density of states and heat capacity for the  $2D$  Kane-Mele and Bernevig-Hughes-Zhang (BHZ) model.

This thesis is structured as follows. In Sec. 2, we review the work on topological phases and how to detect them. As an example, the Kitaev chain is described in Sec. 2.1.2. We present the current methods to describe topological insulators by identifying the energy spectrum of

---

the infinite Kitaev chain, show how the Majoranas emerge at the edge of the finite Kitaev chain and how to calculate topological invariants for this model. Then, in Sec. 3, we show how the formalism of Quelle et al. [8] can be used to identify topological phases in the Kitaev chain. Therefore, we discuss the most important parts of Hill thermodynamics and derive how the finite size and the edge of the systems are appropriately taken into account. At the end of this section, we describe the Kitaev chain with Hill thermodynamics to find the order of the topological phase change. In Sec. 4, the thermodynamic signatures and universalities in the order of the phase transitions for different topological models are discussed. In total, we show for five different models that the order of the phase transition depends on the dimension of the model, and is different for the bulk and the edge. This can be considered as the first main result of this thesis. We continue in Sec. 5 by extending the procedure towards finite-temperatures by showing the entropy, the heat capacity and the finite-temperature topological phase diagram for the Kitaev chain, and the heat capacity and density of states for the Kane-Mele and BHZ model. This finite-temperature extension is the second main result of this thesis. Finally, we conclude in Sec. 6 that Hill thermodynamics is a new and interesting method to describe topological insulators, even at finite-temperatures. We summarize the main findings and provide future research topics, which includes finding (an analogue of) critical exponents for topological insulators.

## 2 Topological materials and experiments

Before we immediately jump into the new topic of this thesis (using Hill thermodynamics to describe topological phases), we should first get a feeling for the materials and the method we are working with: on the one hand topological insulators and superconductors, and on the other Hill thermodynamics. This section is intended to give an introduction to topological insulators. Although this section is not a complete overview of the research in this area, it should give a clear picture of what concepts are at stake (see for excellent reviews on the topic for example Hasan and Kane [5] or Qi and Zhang [6]). As is usual with topological insulators, we will give an example (the Kitaev chain) to get acquainted with topological phases. We start by introducing the concept of topology and follow the historical route to describe the developments in this research area.

Topology is the branch of mathematics that studies the preserved properties of objects when being deformed by smooth transformations, such as the twisting and stretching, but not tearing, of the object. The word originates from the Greek  $\tau\acute{o}\pi\omicron\varsigma$  (place) and  $\lambda\acute{o}\gamma\omicron\varsigma$  (study). A classic example concerns deforming a doughnut into a coffee cup, where one object can be deformed into the other because both contain exactly one hole (also referred to as genus). When two objects can be deformed smoothly into each other, they are called homeomorphic. Objects that cannot be deformed smoothly into each other are considered to be topologically distinct. Examples of topologically distinct objects are a cylinder and a Möbius strip. It is only possible to transform the Möbius strip into a cylinder if we cut the strip and glue the edges together after twisting them as is shown in Fig. 2.1.

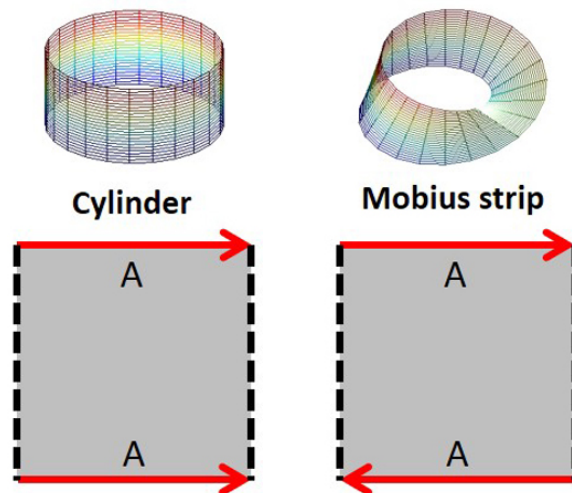


Figure 2.1: Topological differences between a cylinder and a Möbius strip. The arrows indicate where the edges A are joined together. Image retrieved from Ref. [20].

Nowadays, topology is also used by physicists to describe topological insulators and

superconductors. These kind of materials exhibit interesting properties, in which the metallic boundary modes are protected by topology. As we will see, the word “topological” gains a slightly different meaning in this context than the above description. For example, in a topological insulator, there is a circulation of edge currents whereas no smooth deformation is able to break these currents. In the literature, this phenomenon is referred to as topologically protected edge states. However, within topological systems, these smooth deformations are not related to the tearing and cutting of a material, but to symmetry breaking such as time-reversal symmetry, particle-hole symmetry and chiral symmetry. These symmetries state that the Hamiltonian of a system remains invariant (up to a minus sign) when we transform the time  $t$  to  $-t$  (time-reversal symmetry:  $\mathcal{T}$ ), the charge  $q$  to  $-q$  (particle-hole or charge-conjugation symmetry:  $\mathcal{C}$ ), or the product of these former two transformations (sublattice or chiral symmetry:  $\mathcal{S} = \mathcal{TC}$ ). These symmetries are described in the usual tenfold way to classify topological insulators and superconductors, and is the topic of Sec. 2.1.6.

As mentioned, this section is intended to give an overview of the developments in this relatively new branch of physics. The first part of this section, Sec. 2.1, provides a broad overview of the history and a theoretical description of the different types of topological materials. We start Sec. 2.1.1 with the discovery of the quantum Hall effect, the quantum spin Hall effect and topological insulators. Then, we consider an example in Sec. 2.1.2: the 1D Kitaev chain, because an example explains clearly what is interesting in these materials. Next, we discuss how to distinguish the topological phase from the trivial phase via a Chern or winding number in Sec. 2.1.3 and present the most important examples of topological materials; the 2D topological insulator in Sec. 2.1.4, and 3D topological insulators in Sec. 2.1.5. Finally, we describe the so-called ten-fold way in classifying these kind of topological systems in Sec. 2.1.6. In the second part of this section, Sec. 2.2, we present an overview of the experiments to identify topological phases; STM in Sec. 2.2.1, transport in Sec. 2.2.2 and ARPES in Sec. 2.2.3. Finally, the section ends with a brief conclusion of the most important aspects of topological materials in Sec. 2.3.

## 2.1 Topological Materials

### 2.1.1 Quantum Hall effect and quantum spin Hall effect

The first step in understanding topological insulators is to understand ordinary materials like insulators and metals. The second step is to understand topological materials in the context of the quantum (spin) Hall effect. Insulators and conductors have been known in physics and chemistry for a very long time. An insulating state is the most basic state of matter in which it takes a finite energy to dislodge an electron. However, a more detailed understanding of these materials was developed within quantum mechanics within the band theory of solids. The band theory makes use of the underlying translational symmetry of the crystals to

describe electrons in terms of their crystal momentum  $k$  in the periodic Brillouin zone. In this way, the electrons are described by the eigenstates, also called Bloch waves,  $|u_m(k)\rangle$  of the Bloch Hamiltonian  $H(k)$  in a single unit cell of the crystal, having an eigenvalue  $E(k)$ , which defines the energy bands. Within this band theory, the moving electrons and holes of a material are represented by the valence and conducting band. An insulator has an energy gap between the occupied valence band and the empty conducting band, while a conductor does not have an energy gap between these bands, as can be seen in Fig. 2.2. Due to the Pauli principle, electrons cannot be in the same state, which means every electron that is added to a system system at zero temperature must be in a higher energy state than the others. The highest energy of the electrons is given by the so-called Fermi-energy, the difference between the highest and lowest energy level of non-interacting electrons at zero temperature. In metals, the Fermi energy is precisely within a band of allowed energies and therefore electrons are easily excited. Insulators have a gap at the Fermi energy between the valence and conducting band, due to which it takes a finite energy to excite electrons.

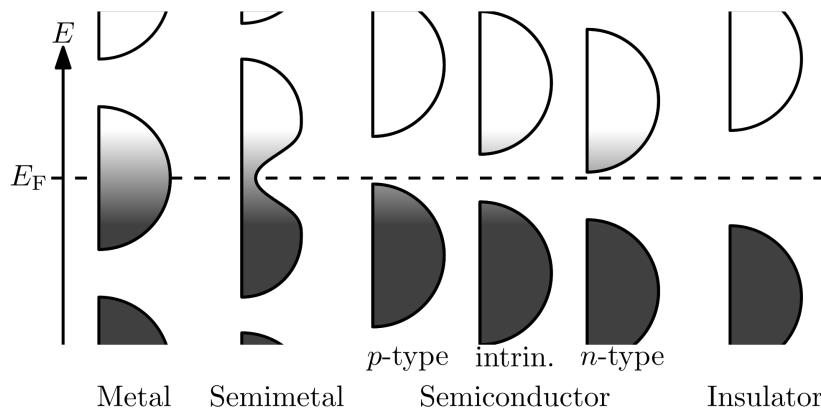


Figure 2.2: The filling of electronic density of states for different materials. The vertical axes shows the energy level of the electrons and the horizontal axes the electronic density of states for different materials. The Fermi level is within the electronic density of states for a metal and a semimetal, but is between the valence and conducting band for a semiconductor and an insulator. Doping a semiconductor with electron accepting impurities (p-type) moves the valence band up, and doping a semiconductor with electron donating impurities moves the conducting band down. Image retrieved from Ref. [21]

Besides metals and insulators, more exotic states of matter have been identified such as semiconductors and semimetals. A semiconductor has a smaller band-gap than an insulator and therefore electrons can be excited to the conducting band. As temperature increases, the semiconductor becomes more conducting, which is opposite to a metal. Furthermore, doping can be used to increase the conductivity of a semiconductor. Doping introduces controlled impurities in the sample and these impurities either release or accept electrons from the valence band of the semiconductor. It is common to distinguish the p-type (acceptor impurities) which moves the valence band towards the Fermi level and the n-type (donor

impurities) semiconductor, which moves the conducting band towards the Fermi level in Fig. 2.2. In semimetals, the electronic density of states is very small at the Fermi level. Therefore a semimetal does not have zero conductivity at zero temperature. This is opposite to semiconductors and insulators, which do have zero conductivity at zero temperature. Moreover, in semimetals, both the holes and the electrons contribute to conductivity, whereas in a metal only the electrons in the conducting band contribute to the conductivity of the material.

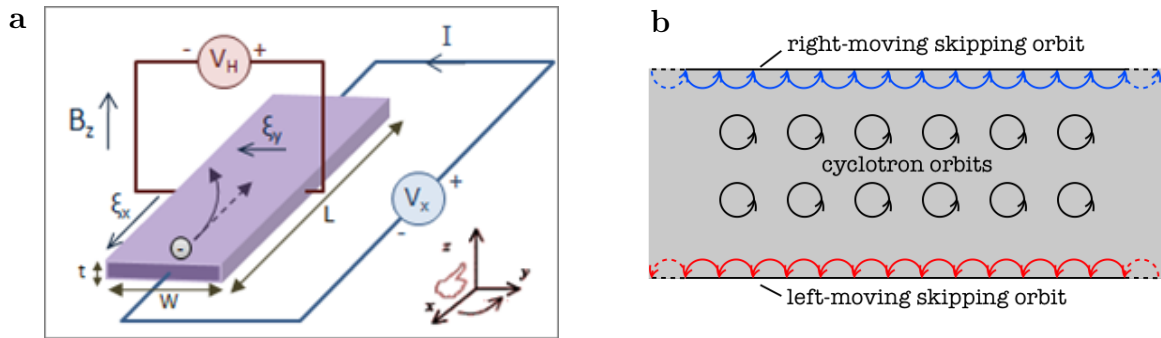


Figure 2.3: **a** Experimental setup how to measure the Hall conductance. A magnetic field  $B$  in the  $z$ -direction deflects electrons traveling in the  $x$ -direction due to the Lorentz force. Therefore the electrons move to the left, creating a voltage difference (Hall voltage  $V_H$ ) in the  $y$ -direction. From this the Hall conductivity can be measured. Image retrieved from Ref. [22]. **b** Classical description of the edge states in the quantum Hall effect. In the presence of a perpendicular magnetic field, the electrons in the system will move in an orbit with the cyclotron radius due to the Lorentz force. However, near the edge of the system the electrons get deflected by the edge making a so-called skipping-orbit. These skipping orbits result in chiral edge currents, which are currents in opposite direction for opposite sides. Image retrieved from Ref. [23].

Where does topology come into play? We describe this by considering the insulating and semiconducting state. We can smoothly deform the Hamiltonian (energy levels) of the insulator, in such a way that the band gap does not close, to obtain the semiconducting state [5]. This is what is called topology for electronic systems: all states that can change into each other without closing the band gap are the same states of matter. This not only makes an insulator the same as a semiconductor, but also the same as the vacuum. The question we now want to answer is whether there might exist electronic states with an energy gap that are not topologically equivalent to the vacuum. And, indeed, there exist such states of matter that we call topological phase. The quantum Hall effect is the first example of such a topological phase. We will discuss this effect below.

Research on topological materials already started in 1975, the year when there has been the first theoretical prediction of a quantized Hall conductance [24]. After this prediction, multiple experiments were performed in order to find this quantized conductance, until five

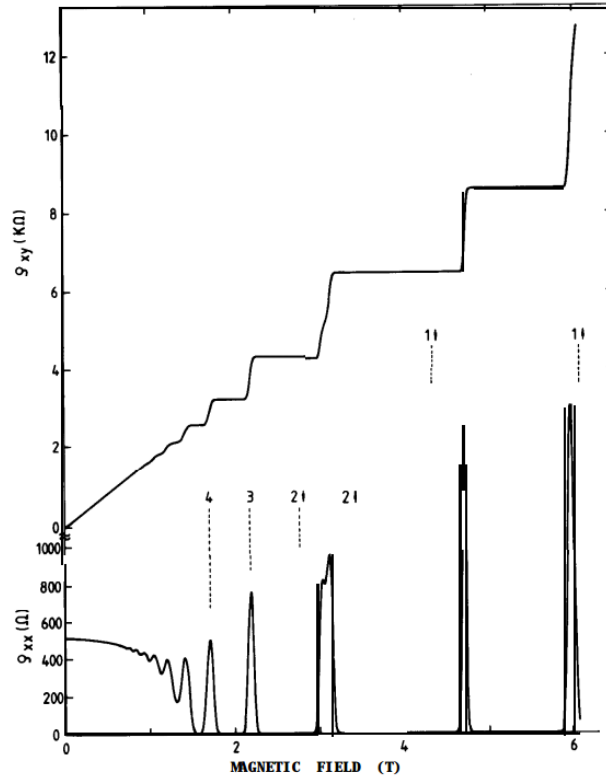


Figure 2.4: The quantum Hall effect [25]. The resistivity is shown with respect to the magnetic field at a temperature of  $8mK$ . The Landau levels can be clearly seen, the horizontal lines, and are characterized by  $h/(e^2n)$ .

years later the group of Klaus von Klitzing indeed discovered what is known as the quantum Hall effect [3].

The quantum Hall effect describes how a two-dimensional (2D) electron system at low temperatures responds to a strong perpendicular magnetic field, see Fig. 2.3a. When one applies a voltage difference in the plane, the electrons will be deflected perpendicularly to the potential difference and to the magnetic field, due to the Lorentz force. This will lead to a transverse current in the  $xy$  direction, which is quantized by integer conductance plateaus  $\sigma_{xy} = ne^2/h$  at low temperatures. Here,  $e$  and  $h$  are the electric charge and the Planck constant and  $n$  is the so-called Landau level. This Hall conductance has been measured with a very large accuracy of  $10^{-9}$ , and is therefore one of the most well-known experiments nowadays. Especially due to the fact that the Hall resistivity can be understood in fundamental constants and an integer number was unexpected. The group of Klaus von Klitzing experimentally measured the resistivity and was awarded the Nobel Prize in 1985. The quantized Landau plateaus are visible in Fig. 2.4.

Besides the quantized conductivity, the quantum Hall effect also gives rise to so-called chiral

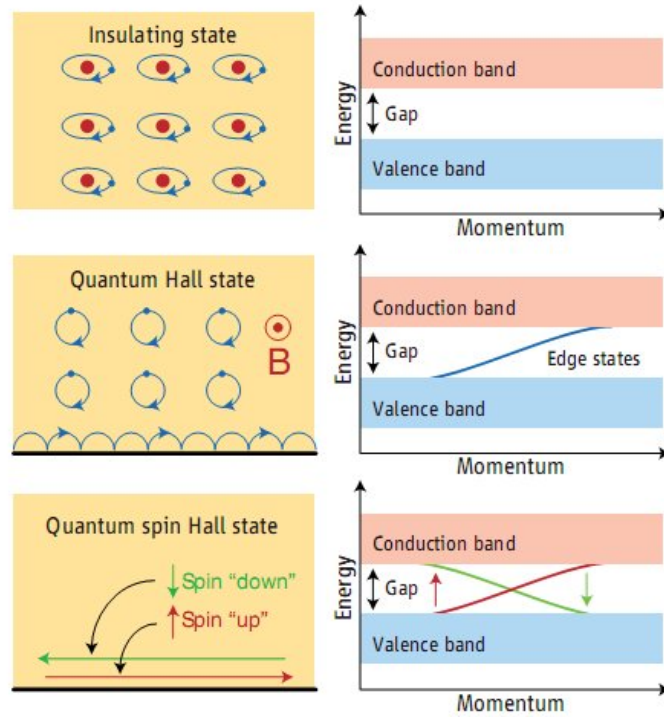


Figure 2.5: The normal insulator, the quantum Hall effect and the quantum spin Hall effect. On the left side, we see the representation in real space, and on the right in  $k$ -space. The insulating state does not have any edge modes and the electrons are stuck to an atom. When applying a perpendicular magnetic field, the electrons circulate and we observe chiral edge states. Without a magnetic field and a strong spin orbit coupling, we obtain the quantum spin Hall effect, where a helical spin current is observed at the boundary of the system.

edge states. Classically, one can think about these edge states as is shown in Fig. 2.3b. The electrons in the center move with a certain velocity in a certain direction, but are deflected by the perpendicular magnetic field and therefore will move in a circular orbit, where the radius is given by the cyclotron radius. Near the edge, when the distance of the electron and the edge is smaller than the cyclotron radius, the electrons cannot exit the system, and will be deflected back into the system by making a so-called skipping orbit. Note that the current on one side is in the opposite direction compared to the other side, which is usually referred to as chiral edge states.

If  $N$  Landau energy levels are filled, there is a finite-energy gap between the occupied and empty energy states, which is similar to an insulator. The energy levels are given by  $E_n = \hbar\omega_c(n + 1/2)$ , where  $\omega_c$  is the cyclotron frequency. However, the chiral edge currents are something rather different and are not observed in a normal insulating state, and this is what is topologically different between the quantum Hall state and a normal insulator. The difference can be calculated explicitly via a Chern or winding number, which is an integer

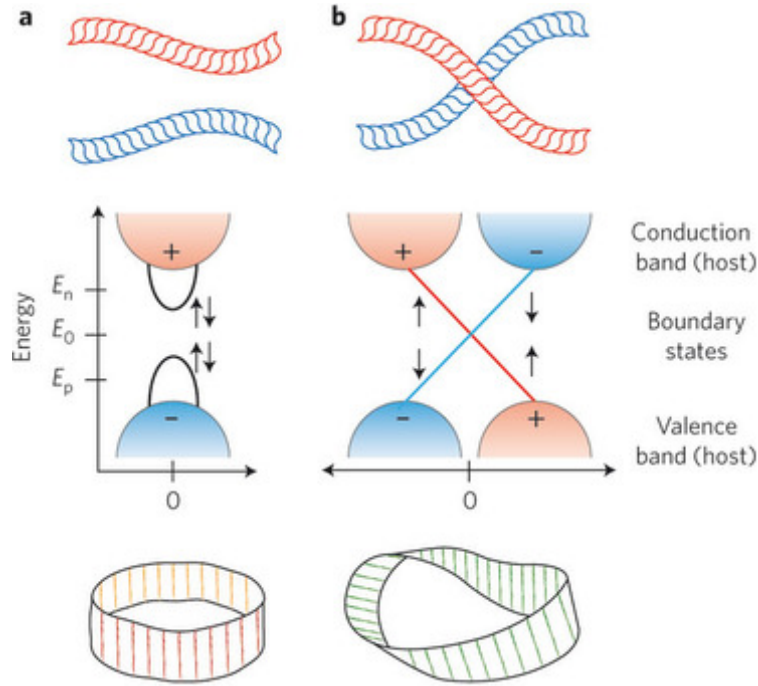


Figure 2.6: Band inversion for a topological insulator [26]. The energies  $E_0$ ,  $E_n$  and  $E_p$  denote the Fermi energies of the neutral, negatively and positively doped solids respectively. The drawings above and below the energies are useful to illustrate the twisting of the energy bands and can be compared with the mathematical description of topology. **a** A normal insulator. **b** Due to a strong spin-orbit coupling and tuning some parameter, a valence band gets a higher energy than its corresponding conduction band, inducing a band-inversion. This band-inversion gives rise to a topologically protected spin current at the boundary of the material.

number indicating whether the system is in the topological or trivial state. In the quantum Hall effect, the Chern number is equal to the Landau level  $n$ , and counts the number of chiral edge states. We will show how to calculate a winding number in the example of the Kitaev chain.

In order to obtain the quantum Hall state, the group of Klitzing made use of a magnetic field, which breaks the time reversal symmetry of the Hamiltonian. In the experiments, the magnetic field was in the order of 15 Tesla, to compensate for the relatively high temperature. This triggered new theories about how to obtain a topological phase without using a magnetic field. The first breakthrough was made by Kane and Mele in 2005 [4]. By making use of the spin-orbit coupling, they were able to theoretically predict the closing of the gap in graphene, giving rise to the quantum spin Hall effect. We summarize the normal insulator, the quantum Hall effect and the quantum spin Hall effect in Fig. 2.5.

The main idea of the quantum spin Hall effect is to use the intrinsic spin-orbit coupling of a material as a “magnetic field”. The spin-orbit coupling denotes that a particles spin interacts

with its motion and therefore influences the energy of the particle. For an electron, spin up and spin down, this means that  $L \cdot S$  either gives a positive or negative contribution to the energy of the particle, which in its turn lifts the energy degeneracy. For large values of the spin-orbit coupling the bands are separated, and it can be the case that the energy for some valence band is higher than the energy for the conducting band, making these two bands invert (see Fig. 2.6b). By inverting the two bands, the energy gap closes and opens again: these two states topologically distinct and give rise to spin currents at the boundary.

The quantum spin Hall effect was predicted to occur in graphene, a 2D system, which indeed has an intrinsic spin orbit coupling. However, the spin-orbit coupling was too small to actually induce the inversion of the bands. Quickly after this theoretical prediction, another prediction was made by Bernevig-Hughes-Zhang, who made use of this idea of spin-orbit coupling by inverting the energy bands and inducing spin currents in quantum wells [9]. After this prediction, the group of Molenkamp were able to measure the quantum spin Hall effect, establishing topological insulators as a new and exciting field in condensed matter physics [11].

To get a better intuition for these topological phases, we explicitly show an example of a topological superconductor. Then, we continue our description of topological phases by giving an introduction to topological invariants (such as Chern and winding numbers) and discuss the main models for the 2D and 3D topological insulators.

### 2.1.2 An example: the Kitaev chain

Topological phases are best understood via an explicit example where the edge states appear in the model. The Kitaev chain is a well-known, paradigmatic one-dimensional (1D) chain, which hosts two phases: one trivial and one topological phase [10]. Especially the topological phase is considered to be of great interest, since this is the phase that hosts unbound Majorana edge states, which can be used for quantum computation. In this part, we show the energy spectrum and how to distinguish the topological phase from the trivial phase.

Unlike the materials we described before, the Kitaev chain is a topological superconductor rather than an insulator, giving rise to a superconducting bulk. It was shown in 2008-2009 that the topological classifications also hold for superconductors [27, 28, 29], where the energy gap is created by the superconducting pairing  $\Delta$ . With a BCS mean-field theory of a superconductor, these materials have an intrinsic particle-hole symmetry than can be used as a protective symmetry for the edge states. Therefore, by closing the gap, there occurs a topological phase transition in the same sense as in topological insulators.

We first consider the motivations for Kitaev to introduce, what is currently known as, the

Kitaev chain: quantum computing. One of the major challenges in quantum computation is the probability of random errors in the calculations and, therefore these errors need to be suppressed. One of the options for this fault-tolerant quantum computing is based on the physical level of the quantum bits, in which non-Abelian anyons are used. Inspired by this proposal, Kitaev introduced a new kind of model, where unbound Majoranas at the edge are immune to any kind of error.

The idea is as follows. Quantum states are sensitive to errors of two kinds: a classic and a phase error. When the classic error  $\sigma_j^x$  acts on a state at position  $j$ , the operator changes a quantum bit (qubit)  $|0\rangle$  into a  $|1\rangle$  and vice versa. A phase error  $\sigma_j^z$  changes the sign of all qubits at position  $j$  with state  $|1\rangle$  relative to all  $|0\rangle$  states at position  $j$ . In general, one of the errors can be removed from the system rather easily, but removing both errors is difficult.

Therefore Kitaev proposes to use Majoranas as qubits. In the proposed system an electron at a site is resembled by a  $|1\rangle$  and a hole by a  $|0\rangle$ . In this way, the system is immune to classic errors due to charge conservation. However, two classic errors might still occur when an electron jumps from one site to another. Two (or a multiple of two) classic errors can be prevented if the fermionic sites are placed far from each other and the medium between the electrons has an energy gap in the excitation spectrum. In this system, we can also prevent a phase error to occur. As we will see, we can introduce Majorana-operators, which can be considered to be both electron and hole. Each fermionic site, normally described in terms of  $a_j$  and  $a_j^\dagger$ , can be expressed in terms of two Majorana operators  $\eta_j$  and  $\gamma_j$ ,

$$a_j = \frac{1}{2}(\eta_j + i\gamma_j), \quad a_j^\dagger = \frac{1}{2}(\eta_j - i\gamma_j), \quad (j = 1, 2, \dots, N), \quad (2.1)$$

with  $N$  the total number of sites. The Majorana operators  $\eta_j$  and  $\gamma_j$  belong to different Majorana sites. These operators indeed satisfy the Majorana criterion

$$\eta_j = \eta_j^\dagger \quad \gamma_j = \gamma_j^\dagger \quad (2.2)$$

and the anti-commutation relations  $\{\eta_i, \gamma_j\} = 0$ . Now, a phase error can be expressed as  $a_j^\dagger a_j = 1/2(1 + i\gamma_j \eta_j)$  and this shows that a phase error can only occur when there is an interaction between two Majorana-sites. Possibly, it can be avoided that there is such an interaction, and therefore Kitaev argues that this kind of error is unlikely to occur. Moreover, an isolated Majorana operator cannot appear in the Hamiltonian because it does not obey the fermionic parity. Thus, an isolated Majorana site is immune to any kind of error and can be perfectly used as a qubit for computations.

As an example to detect these isolated Majoranas, Kitaev describes a rather unrealistic but

simple model where unbound Majorana edge states show up at the boundary in the topological phase of a 1D chain. In this section, we will describe the model that he introduced and show how the Majorana edge modes appear. We first start to get a feeling for these topological phases by analyzing the spectrum of the infinite Kitaev chain, which can be solved analytically, and how to find the Green's functions of this chain, which could be measured via STM (see Sec. 2.2.1). Then, we describe the finite Kitaev chain and how the unbound Majoranas appear at the edges of the chain in the topological phase. Finally we show how the bulk-boundary correspondence can be used by analyzing the bulk to obtain information about the boundary via the winding number.

**The infinite Kitaev chain** We start by showing the energy spectrum of the Kitaev chain in the bulk. In his article, Kitaev considers a 1D chain on a superconducting surface and the electrons in the chain are assumed to be spinless [10]. The Hamiltonian is

$$H = -\mu \sum_{i=1}^N a_i^\dagger a_i - \sum_{i=1}^{N-1} [t(a_i^\dagger a_{i+1} + a_{i+1}^\dagger a_i) - \Delta a_i a_{i+1} - \Delta^* a_{i+1}^\dagger a_i^\dagger], \quad (2.3)$$

where  $N$  is the number of sites,  $\mu$  is the chemical potential,  $t \geq 0$  is the hopping parameter,  $\Delta$  and  $\Delta^* \geq 0$  are superconducting gaps (pairing energies) and  $a_i$  ( $a_i^\dagger$ ) are fermionic destruction (creation) operators at position  $i$ , satisfying the anti-commutation relation  $\{a_i, a_j^\dagger\} = \delta_{i,j}$ . In order to describe the energy spectrum of this system, it is useful to perform a Fourier transformation. By using Bloch's theorem, we introduce Fourier expansions of the operators

$$a_j = \frac{1}{\sqrt{N}} \sum_k e^{iklj} a_k, \quad a_j^\dagger = \frac{1}{\sqrt{N}} \sum_k e^{-iklj} a_k^\dagger, \quad (2.4)$$

where  $l$  is the distance between two neighboring sites and  $-\pi m/(Nl) \leq k \leq \pi m/(Nl)$ , with  $|m| \leq N/2$ . We can substitute these expressions into Eq. (2.3) and use the definition of the delta function  $\delta_{k,k'} = 1/N \sum_j e^{ij(k-k')}$  for an infinite Kitaev chain ( $N \rightarrow +\infty$ ), to obtain

$$H = \sum_k [\epsilon_k a_k^\dagger a_k + \Delta a_{-k} a_k e^{ikl} + \Delta^* a_k^\dagger a_{-k}^\dagger e^{-ikl}], \quad (2.5)$$

where  $\epsilon_k = -\mu - 2t \cos(kl)$ , which satisfies  $\epsilon_k = \epsilon_{-k}$ . It is convenient to rewrite Eq. (2.5) using a matrix notation. Because we sum over all the values of  $k$ , one obtains a  $\sin(kl)$  in the matrix notation, where  $k > 0$ :

$\sum_k a_{-k} a_k e^{ikl} = 1/2 \sum_k a_{-k} a_k e^{ikl} + a_k a_{-k} e^{-ikl} = 1/2 \sum_k a_{-k} a_k (e^{ikl} - e^{-ikl}) = i \sum_k a_{-k} a_k \sin(kl)$ . By a similar calculation for  $a_k^\dagger a_{-k}^\dagger$ , we find

$$H = \frac{1}{2} \sum_k \left[ \begin{pmatrix} a_k^\dagger & a_{-k} \end{pmatrix} \begin{pmatrix} \epsilon_k & -2i\Delta^* \sin(kl) \\ 2i\Delta \sin(kl) & -\epsilon_k \end{pmatrix} \begin{pmatrix} a_k \\ a_{-k}^\dagger \end{pmatrix} + \epsilon_k \right], \quad (2.6)$$

and the extra  $\epsilon_k$  comes from the anti-commutation relations for the fermionic operators. In order to find the quasiparticle excitations of the infinite Kitaev chain, we want to obtain the action and determine the poles of the Green's function [30]. Furthermore, by obtaining the Green's function we are able to calculate the density of states for the Kitaev chain. Therefore, we go back to the original second quantized Hamiltonian Eq. (2.3) and introduce the field operators

$$\phi(x) = \sum_i a_i \chi_i(x), \quad \phi^\dagger(x) = \sum_i a_i^\dagger \chi_i^*(x), \quad (2.7)$$

which annihilate and create a particle at position  $x$ . The wave function  $\chi(x)$  represents a full set of eigenstates in space coordinates. For these relations, we can obtain the anti-commutation relations for the field operators

$$\{\phi(x), \phi(x')\} = \{\phi^\dagger(x), \phi^\dagger(x')\} = 0, \quad \{\phi(x), \phi^\dagger(x')\} = \delta(x - x'), \quad (2.8)$$

where we used the anti-commutation relations for  $a_i$  and  $a_i^\dagger$ , the completeness relation  $\sum_j \chi_j(x) \chi_j^*(x') = \delta(x - x')$  and the relations from Eq. (2.7). Normally, the action for the fields  $\phi$  is given by

$$S[\phi^*, \phi] = \int dt d^3x \mathcal{L}(\phi, \nabla\phi, \frac{\partial\phi}{\partial t}), \quad (2.9)$$

but now, by using a Wick rotation  $t \rightarrow -i\tau$ , we can rewrite this action into the Euclidean space

$$S_E[\phi^*, \phi] = \int_0^{\hbar\beta} d\tau \int d^3x \left\{ \phi^*(x, \tau) \hbar \frac{\partial}{\partial \tau} \phi(x, \tau) + H[\phi^*(x, \tau), \phi(x, \tau)] \right\}. \quad (2.10)$$

which is more convenient because the time component can be treated in the same way as the space components. It is helpful to introduce a Matsubara expansion to evaluate the action. We expand the operators not only in space coordinates, but also in imaginary frequency space

$$\phi(x, \tau) = \sum_i \sum_{n=-\infty}^{+\infty} a_{i,n} \chi_i(x) \frac{e^{-i\omega_n \tau}}{\sqrt{\hbar\beta}}, \quad (2.11)$$

where  $\omega_n = \pi(2n + 1)/(\hbar\beta)$  for the fermionic fields. It is now possible to substitute this expression in Eq. (2.3) for the field operators. We can Fourier transform this expression again, using Eq. (2.4), which yields

$$S_E = -\frac{1}{2} \sum_{k,n} \begin{pmatrix} a_k^\dagger & a_{-k} \end{pmatrix} \begin{pmatrix} +i\hbar\omega_n & 0 \\ 0 & +i\hbar\omega_n \end{pmatrix} \begin{pmatrix} a_k \\ a_{-k}^\dagger \end{pmatrix} + H := -\frac{1}{2} \sum_{k,n} \begin{pmatrix} a_k^\dagger & a_{-k} \end{pmatrix} \hbar G^{-1}(k, \omega_n) \begin{pmatrix} a_k \\ a_{-k}^\dagger \end{pmatrix}, \quad (2.12)$$

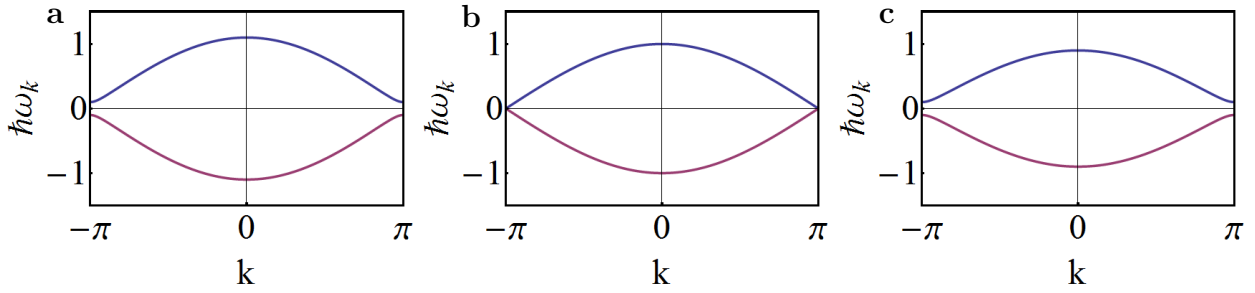


Figure 2.7: The energy spectrum for the Kitaev chain, where  $t = \Delta = \Delta^* = 0$  and **a**  $\mu = 0.6$ , **b**  $\mu = 0.5$  and **c**  $\mu = 0.4$ . A phase transition occurs when going from the trivial phase **a** to the topological phase **c**.

where

$$G^{-1} = \begin{pmatrix} -\epsilon_k/\hbar + i\omega_n & +2i\Delta^* \sin(kl)/\hbar \\ -2i\Delta \sin(kl)/\hbar & +\epsilon_k/\hbar + i\omega_n \end{pmatrix} \quad (2.13)$$

is the inverse Green's function. The Green's function is the inverse of this matrix

$$G = -\frac{1}{V} \sum_k \frac{1}{2\hbar\omega_k} \begin{pmatrix} +\epsilon_k + \hbar\omega_k & +2i\Delta \sin(kl) \\ -2i\Delta^* \sin(kl) & -\epsilon_k + \hbar\omega_k \end{pmatrix} [1 - 2N_{\text{FD}}(\hbar\omega_k)], \quad (2.14)$$

where we have summed over the Matsubara frequencies. Furthermore, the energy is  $(\hbar\omega_k)^2 = \epsilon_k^2 + 4|\Delta|^2 \sin^2(kl)$ . First, we look at the energy spectrum of the Kitaev chain and later, we show how to calculate the Green's function. The poles of the Green's function, which resemble the single particle excitations of the Kitaev chain, are given by

$$\hbar\omega_k = \pm \sqrt{[\mu + 2t \cos(kl)]^2 + 4|\Delta|^2 \sin^2(kl)}. \quad (2.15)$$

This energy spectrum is shown in Fig. 2.7 for a fixed value of  $t = \Delta = \Delta^* = 0.25$  and for varying  $\mu$ . By varying the chemical potential  $\mu$ , it is possible to close the energy gap and therefore find two topologically different phases; one trivial phase (Fig. 2.7a) and one topological phase (Fig. 2.7c). The phase transition occurs when  $\mu = \pm 2t$ . Furthermore, the superconducting pairing  $\Delta$  opens up a gap in the energy spectrum. When observing the figures, no clear distinction can be made between the energy spectrum in the trivial or topological phase, but when we discuss these phases further in Sec. 2.1.2, we will see one phase hosts zero-energy states whereas the other does not. It can also be seen in the figure that the Kitaev chain has an intrinsic particle-hole symmetry, which is indicated by a positive and negative energy value for each value of  $k$ .

Let us calculate  $G_{12}$  as an example by summing over the Matsubara frequencies. First, we

observe that

$$G_{12} = \sum_{n,k} \frac{2i\Delta \sin(kl)}{\hbar^2\beta V(-\epsilon_k^2/\hbar^2 - 4|\Delta|^2 \sin^2(kl)/\hbar^2 - \omega_n^2)} = -\frac{\hbar}{\hbar\beta V} \sum_{n,k} \frac{2i\Delta \sin(kl)}{(\hbar\omega_n)^2 + (\hbar\omega_k)^2}, \quad (2.16)$$

Now, we are in a position to perform the sum over the fermionic Matsubara frequencies. It is possible to rewrite the component of the Green's function as

$$-\frac{\hbar}{\hbar\beta V} \sum_k i\Delta \sin(kl) \sum_n \frac{1}{\hbar^2\omega_k} \left[ \frac{1}{\omega_k + i\omega_n} + \frac{1}{\omega_k - i\omega_n} \right]. \quad (2.17)$$

In order to calculate this integral, we can use contour integration [30], to find that

$$\lim_{\eta \downarrow 0} \frac{1}{\hbar\beta} \sum_n \frac{e^{i\omega_n\eta}}{i\omega_n - \omega_k} = \lim_{\eta \downarrow 0} \frac{1}{2\pi i} \int_C dz \frac{e^{\eta z}}{z - \omega_k} \frac{-1}{e^{\hbar\beta z} + 1} \quad (2.18)$$

by considering a contour which goes around the Matsubara frequencies, as shown in Fig. 2.8. The contour  $C$  encloses the entire imaginary axis for which the function  $\hbar\beta/(\exp[\hbar\beta z] + 1)$  has poles at the Matsubara frequencies  $\omega_n$ . We can freely add infinite arcs  $C'$  to the contour  $C$ . This can be seen by considering the right hand side of Eq. (2.18). The integrand behaves as  $\exp[(-\hbar\beta - \eta) \text{Re}(z)]/|z|$  for  $\text{Re}(z) \rightarrow \infty$  and  $-\exp[-\eta \text{Re}(z)]/|z|$  for  $\text{Re}(z) \rightarrow -\infty$ . This means that the integrand always vanishes must faster for  $0 < \eta < \hbar\beta$ , namely exponentially fast, and thus we can add the contour  $C'$  because it gives no contribution. However, if we now consider the contours formed by  $C$  and  $C'$ , we observe a pole for  $1/(z - \omega_k)$ , and not for the Matsubara frequencies anymore. We can use this different contour and obtain

$$\lim_{\eta \downarrow 0} \frac{1}{2\pi i} \int_{C+C'} dz \frac{e^{\eta z}}{z - \omega_k} \frac{-1}{e^{\hbar\beta z} + 1} = +\frac{1}{e^{\hbar\beta\omega_k} + 1}. \quad (2.19)$$

by using the residue theorem. This expression is also known as the Fermi-Dirac distribution  $N_{\text{FD}}(\hbar\omega_k)$ . Finally, we can perform the sum over the Matsubara frequencies by identifying a proper contour integration to end up with

$$G_{12} = -\frac{1}{V} \sum_k \frac{\Delta \sin(kl)}{\hbar\omega_k} [1 - 2N_{\text{FD}}(\hbar\omega_k)]. \quad (2.20)$$

This final result states that the Green's function of the infinite Kitaev chain can be rewritten in terms of the Fermi-Dirac distribution. The other components of the Green's function can be treated in a similar manner and will yield similar results as can be seen in Eq. (2.14).

As is shown in Sec. 2.2.1, the Green's function is related to the spectral function and hence the local density of states of a sample. By calculating the Green's, function we therefore gain insight in the electron distribution of the Kitaev chain and can predict what the tunneling

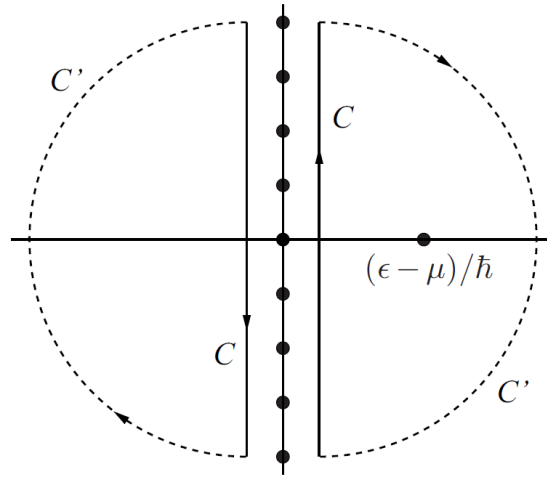


Figure 2.8: Illustration of the contours that are used for the calculation of the sum over the Matsubara frequencies. The black dots refer to the poles in Eqs. (2.18) and (2.19). The poles for the Matsubara frequencies are displayed on the y-axis, whereas the pole for  $z - \omega_k$  corresponds in the figure to the pole at  $(\epsilon - \mu)/\hbar$ .

conductance will be in an STM experiment.

**Majorana zero modes** Although the Majorana bound states have not been observed in the investigation of the infinite Kitaev chain, we have already seen how to derive the Green's function and calculated the energy spectrum of the Kitaev chain in the two distinct topological phases. Now, we want to make a connection with Majoranas by considering the finite Kitaev chain.

It is possible to numerically diagonalize the Hamiltonian of a finite system, such as given by Eq. (2.3). Therefore, the Hamiltonian is first rewritten as

$$H = \frac{1}{2} \begin{pmatrix} a_1^\dagger & a_1 & a_2^\dagger & a_2 & \cdots & a_N^\dagger & a_N \end{pmatrix} \begin{pmatrix} -\mu & 0 & -t & -\Delta^* & \cdots & 0 & 0 \\ 0 & +\mu & \Delta & t & \cdots & 0 & 0 \\ -t & \Delta^* & -\mu & 0 & \cdots & 0 & 0 \\ -\Delta & t & 0 & +\mu & \cdots & 0 & 0 \\ \vdots & \vdots & \vdots & \vdots & \ddots & \vdots & \vdots \\ 0 & 0 & 0 & 0 & \cdots & -\mu & 0 \\ 0 & 0 & 0 & 0 & \cdots & 0 & +\mu \end{pmatrix} \begin{pmatrix} a_1 \\ a_1^\dagger \\ a_2 \\ a_2^\dagger \\ \vdots \\ a_N \\ a_N^\dagger \end{pmatrix} - \mu N/2, \quad (2.21)$$

of which the energies (eigenvalues) can be numerically calculated. The energies for a Kitaev chain with  $N = 250$  are depicted in by Fig. 2.9 for  $t = \Delta = \Delta^* = 0.25$ , and varying  $\mu$  (the same parameters as before to identify the phase transition). In these figures, the particle-hole symmetry can be observed immediately, since there are two symmetric energy branches for

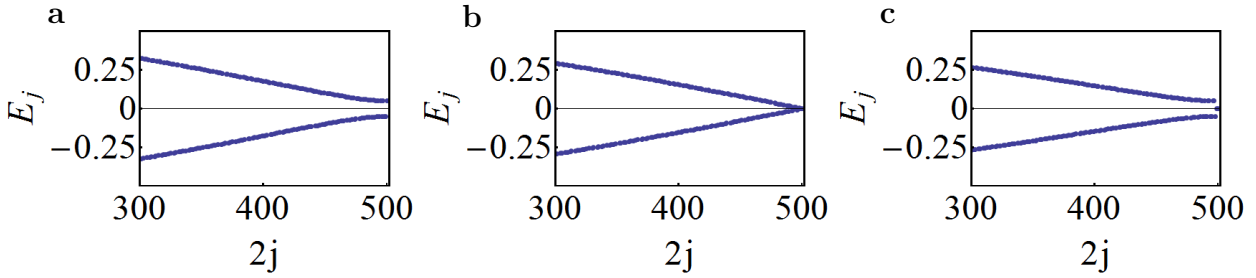


Figure 2.9: The energy spectrum for the finite Kitaev chain for  $t = \Delta = \Delta^* = 0.25$  and **a**  $\mu = 0.6$ , **b**  $\mu = 0.5$  and **c**  $\mu = 0.4$ . A phase transition occurs when going from the trivial phase in **a** to the topological phase **c**. In **c**, Majorana zero modes appear in the spectrum.

each lattice site  $j$ . Furthermore, the energies in Fig. 2.9a are all finite, whereas in Fig. 2.9c, there exists two phases with zero energy. Since Majoranas cannot have a finite energy, these two zero-energy states are the Majoranas at the edge of the finite Kitaev chain and indeed, they only emerge in the topological phase.

Another way to observe the Majorana zero modes is to introduce Majorana-fermion operators  $\eta_j$  and  $\gamma_j$  at position  $j$ . Recall from Eq. (2.1) that  $a_j = 1/2(\eta_j + i\gamma_j)$  and  $a_j^\dagger = 1/2(\eta_j - i\gamma_j)$ . Due to these unique properties, it is no longer possible to conceive a Majorana state as being empty or filled in a similar way as is usual for other fermions. Moreover, every fermionic operator can be rewritten into pairs of Majorana operators, which means that the Majorana zero modes always come in pairs (although these pairs may be spatially isolated from each other). Substituting these Majorana operators into the Hamiltonian from Eq. (2.3), we find

$$H = \frac{i}{2} \left[ \sum_i^N -(\mu\eta_i\gamma_i) + \sum_i^{N-1} (|\Delta| + t)\gamma_i\eta_{i+1} + (|\Delta| - t)\eta_i\gamma_{i+1} \right] - \mu N/2. \quad (2.22)$$

As shown by Kitaev [10], this Hamiltonian leads to two special phases that deserve further inspection. In Eq. (2.22), we observe an energy competition between Majorana operators on a single site ( $\eta_j\gamma_j$ ) and Majorana operators on neighboring sites ( $\eta_j\gamma_{j+1}$  or  $\gamma_j\eta_{j+1}$ ). This competition leads to two distinct phases, in which the coupling between the Majorana bound states is either within a lattice site or between lattice sites. It is possible to Fourier transform the Majorana operators and to diagonalize the obtained Hamiltonian, to find the same energy spectra shown in Fig. 2.7. We will analyze these two different phases below.

1.  $\mu < 0$  and  $t = |\Delta| = 0$ , Fig. 2.10.

This is the trivial case, in which the Majorana operators of the same site are connected to each other. The Hamiltonian takes the form  $H = -\frac{i}{2} \sum_j^N \mu\eta_j\gamma_j$  and the ground state has occupation number zero.

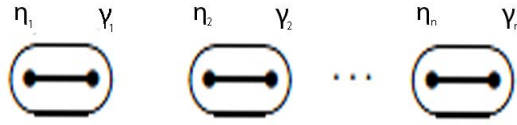


Figure 2.10: The trivial phase of the Kitaev chain

2.  $\mu = 0$  and  $t = |\Delta| \neq 0$ , Fig. 2.11.

In this case, the Hamiltonian can be written as  $H = it \sum_j^{N-1} \gamma_j \eta_{j+1}$  and Majorana operators at *different* sites couple to each other. Note that the Hamiltonian does not depend on  $\gamma_N$  and  $\eta_1$ , which indeed is a signature of the unbound Majoranas at the edges of the chain. When  $t = -|\Delta|$ , the situation is the same ( $H = it \sum_j^{N-1} \eta_j \gamma_{j+1}$ ), although the Majorana zero modes have switched sides.

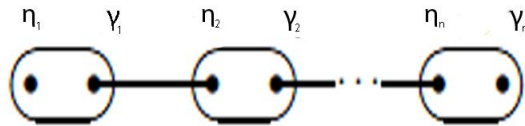


Figure 2.11: The topological phase of the Kitaev chain

These two cases represent two different topological phases, which can be easily transformed into each other via a redefinition of the Majorana operators  $\eta_{i+1} \leftrightarrow \eta_i$ . This transformation shows that the bulk properties of both phases are very similar. However, the edges are rather different, since only the second case contains Majoranas at the boundaries. In general, the Kitaev chain is in the trivial phase for  $|\mu| > 2t$  and in the topological phase for  $|\mu| < 2t$ , the band gap closing is at  $|\mu| = 2t$ . Now, we diagonalize the Hamiltonian (2.22) to obtain the energy spectrum in real space for the Majorana operators. We obtain the same values for the energy spectrum as previously in Fig. 2.9, where one can distinguish the Majorana bound states at the edge of the system. Moreover, these Majoranas are protected by the particle-hole symmetry. Due to this symmetry, every positive energy needs to have a corresponding negative energy (a particle and a hole). One interpretation of the Kitaev chain is that every single unit site now has a particle and a hole. In the topological phase, the Majoranas at the boundary do not have a partner, which means that they need to have zero energy to obey this particle-hole symmetry. Since they are at the other side of the chain, these states do not communicate, and as a result one edge state cannot have a finite energy, because the other edge state would not know that it should have the same negative energy. This effect implies that the boundary modes cannot change unless the band gap is closed and

a topological phase transition occurs. The robust edge states in the topological phase are protected by the particle-hole symmetry.

**Topological invariants** An interesting question is how to determine whether the chain is in the topological or trivial state, without looking at the boundaries of the system. This is reflected in the bulk-boundary correspondence. In principle, there are two main ways of classifying this in the Kitaev chain. The first method was proposed by Kitaev and involves counting the number of Majorana zero-modes at the edge of the system [10]. The second method, which is the one that is mainly used, calculates the winding number of the model. We present both methods, starting with the counting of Majoranas.

Kitaev starts by defining a Majorana number  $\mathcal{M} = \pm 1$ , which is  $-1$  when there are Majorana bound-states in the chain and  $+1$  when these modes are absent. When we connect two independent chains, the Majorana number should satisfy  $\mathcal{M}(H_1 \oplus H_2) = \mathcal{M}(H_1)\mathcal{M}(H_2)$ , where  $\oplus$  means we connect two independent chains given by  $H_1$  and  $H_2$ , see also Fig. 2.12. In the end, the trick is to connect this number to the fermionic parity  $P$ , which is measured via the operator  $P = \prod_i -i\eta_i\gamma_i$ . The Majorana number can be used to study the boundary modes by looking at the bulk properties of the system. Therefore, we connect two different chains of length  $L_1$  and  $L_2$ , close the chain and assume periodic boundary conditions. Kitaev proofs that for such a system of length  $L = L_1 + L_2$ , the ground state parity

$$P(H(L_1 + L_2)) = \mathcal{M}(H)P(H(L_1))P(H(L_2)), \quad (2.23)$$

where  $H(L)$  denotes the Hamiltonian of the system with length  $L$ . For systems of equal length  $L_1 = L_2$ , this equation simplifies to  $\mathcal{M}(H) = P(H(L))$ .

The Majorana number can be related to the Pfaffian of an anti-symmetric matrix. In terms of the Majorana operators, the Kitaev chain Hamiltonian in general has the form

$H = i/2 \sum_{i,j} \eta_i A_{i,j} \gamma_j$ , where  $A_{i,j}$  is a real, anti-symmetric matrix. Via a Jordan-Wigner transformation, this matrix can be rewritten in a form

$$A_{i,j,J} = W A W^T = \text{diag}_\lambda \begin{pmatrix} 0 & \epsilon_\lambda \\ -\epsilon_\lambda & 0 \end{pmatrix}, \quad (2.24)$$

where  $W$  is a orthogonal matrix and  $\text{diag}_\lambda$  denotes that the diagonal of the  $2N \times 2N$  matrix is this  $2 \times 2$  block matrix. Now, the value of  $\det[W] = \pm 1$  determines whether there is an even (+1) or odd parity (-1) in the system. By considering Eq. (2.24), we can write  $\text{Pf}A_J = \prod_\lambda \epsilon_\lambda$  and, because of the relation  $\text{Pf}[W A_J W^T] = \det[W] \text{Pf}[A]$ , we obtain  $P(H) = \text{sgn} \text{Pf}[A] = \text{sgn} \det[W] = \pm 1$ .



Figure 2.12: The Majorana number is conserved when connecting two independent closed chains  $L_1$  and  $L_2$  [10].

For the Kitaev chain, we have particle-hole symmetry, which means that every positive energy  $E(k)$  has a negative energy  $-E(-k)$ . There are only two points where the band gap closes and which can be projected into itself:  $k = 0$  and  $k = \pi$ . This implies we can only focus on these specific points and derive

$$\mathcal{M} = \text{sgn}(\text{Pf}[\tilde{A}(0)]\text{Pf}[\tilde{A}(\pi)]) = \det[\tilde{W}(0)]\det[\tilde{W}(\pi)], \quad (2.25)$$

where the  $\tilde{A}$  and  $\tilde{W}$  represent the Fourier transform in  $k$  space of  $A$  and  $W$  respectively. The value of  $\mathcal{M}$  determines whether we are in the topological ( $\mathcal{M} = -1$ ) or in the trivial phase ( $\mathcal{M} = +1$ ) and is undefined at the gap closing. By cutting the wire into two parts, the Majorana bound states remain present or absent. By taking the product of these Pfaffians, we are comparing the fermionic parity at  $k = 0$  and  $k = \pi$ , which only results in a topological phase if the parity at these points is different. The Majorana operator  $\mathcal{M}$  only changes when there is a continuous deformation between the  $\tilde{A}(0)$  and  $\tilde{A}(\pi)$  in which the gap closes, and this is indeed what is needed for a topological invariant.

Perhaps a less complicated construction of a topological invariant for the Kitaev chain is based on the winding number. In general, one can attach a global parameter to a topological system which measures whether the bulk is in the topological or trivial phase. When the model has chiral symmetry, this quantity is a winding number, otherwise it is a Chern number [31].

For the Kitaev chain, we will now find the winding number  $w$ . We first consider Eq. (2.6) and observe that we can rewrite the Hamiltonian in the block form

$$H = \frac{1}{2} \sum_k \left[ \begin{pmatrix} a_k^\dagger & a_{-k} \end{pmatrix} \mathcal{H} \begin{pmatrix} a_k \\ a_{-k}^\dagger \end{pmatrix} \right], \quad (2.26)$$

where

$$\mathcal{H} = h(k) \cdot \sigma = h_y \sigma_y + h_z \sigma_z, \quad (2.27)$$

and we have  $h_y = 2\Delta \sin(kl)$ ,  $h_z = \epsilon_k = -\mu - 2t \cos(kl)$  and  $\sigma_i$  the Pauli matrices ( $i \in \{x, y, z\}$ ).

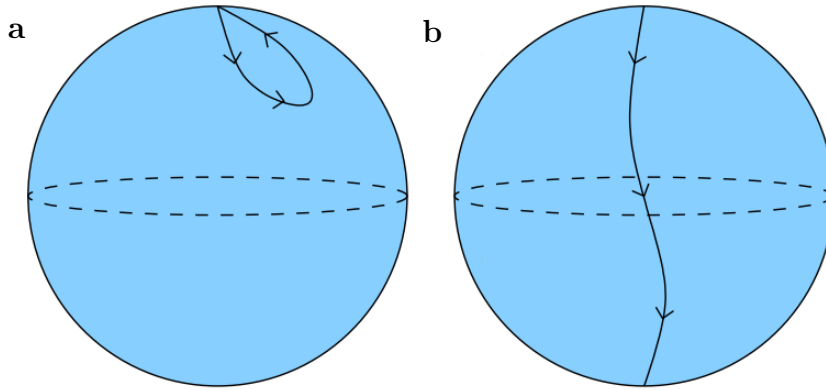


Figure 2.13: Illustration of the mapping of  $\hat{h}$ . **a** The trivial phase in which  $\hat{h}$  has the same sign for  $k = 0$  and  $k = \pi$ . **b** The topological phase where the sign is different for the two values of  $k$ . Image retrieved via Ref. [32]

The unit vector  $\hat{h} = h(k)/|h(k)|$  now maps the half Brillouin zone  $k \in [0, \pi]$  to the 2-sphere  $S^2$ . At  $k = 0, \pi$  the normal  $\hat{h}$  points either to the north or the south pole (only  $\hat{z}$ -direction is nonzero). In this case, two things can happen. Either  $\hat{h}$  has the same sign at  $k = 0$  and  $k = \pi$ , which is in the trivial phase ( $|\mu| > 2t$ ), or it has opposite sign, which is in the topological phase ( $|\mu| < 2t$ ). This reasoning is visualized in Fig. 2.13. If the system is gapped, the normal is not well defined, and the system goes through a phase transition when going from the north to the south pole.

The winding number can then be calculated via an integral over the Brillouin zone

$$w = \frac{1}{2\pi} \int dk \left( \hat{h}_z \frac{\partial \hat{h}_y}{\partial k} - \hat{h}_y \frac{\partial \hat{h}_z}{\partial k} \right), \quad (2.28)$$

which counts how many times  $h$  wraps around the unit sphere (which is indeed a winding number). The winding number is either 0 when the system is in the trivial phase or 1 in the topological phase. In this way it is possible to use the bulk information (bulk Hamiltonian) to derive information about the edge states (the presence or absence of Majoranas).

By considering the Kitaev chain, we have shown an explicit example of topological phases and how the protected edge states emerge in these materials. We have also seen how to rewrite the Hamiltonian in terms of Majorana operators and calculated the energy spectrum in real space, where the zero energy states were easily observed. Finally, we discussed how to find topological invariants for the model, where we also discussed how to calculate the winding number. The winding number forms a part of the more general topological invariants, which is the topic of the next section.

### 2.1.3 Topological invariants

In general, topological phases are identified with a Chern number that can either be interpreted as an integral of the Berry phase or as a winding number in the case we have seen in the previous section [5, 6]. We already mentioned the Chern number in the discussion of the quantum Hall effect, which is one of the first examples in condensed matter where the Chern number indicates whether the system is in the trivial or nontrivial phase. We will give a short introduction to these topological invariants in this section.

The use of the Chern number in topological insulators can be related back to the Thouless, Kohmoto, Nightingale and Den Nijs (TKNN) invariant [33]. In 1982, TKNN found that the filling fraction  $n$  in the quantum Hall effect, the Landau levels, is related to an integer topological invariant: the Chern number. Originally, the Chern number comes from the mathematical theory of fiber bundles [34], but is more easily understood in physics with the Berry phase. When the vector  $k$  is transported around a closed loop, the eigenstate  $|\psi_m(k)\rangle$  can obtain a Berry phase  $A_m$ , which is given by the line integral  $A_m = i \langle \psi_m(k) | \nabla_k | \psi_m(k) \rangle$ , where  $\nabla_k = (\partial/\partial k_1, \dots, \partial/\partial k_n)$ . The Chern number can then be expressed as the total Berry flux in the Brillouin zone (BZ)

$$C_m = \frac{-i}{2\pi} \int_{\partial\text{BZ}} dk \langle \psi_m(k) | \nabla_k | \psi_m(k) \rangle, \quad (2.29)$$

which can also be rewritten by Stokes theorem as an integral over the Brillouin zone of the Berry curvature

$$C_m = \frac{1}{2\pi} \int_{\text{BZ}} d^2k F, \quad (2.30)$$

where  $F = \nabla \times A$  is the Berry flux or Berry curvature. According to the Chern theorem, this integral of the Berry curvature over a closed manifold is quantized in units of  $2\pi$ , and therefore, the Chern number is a quantized integer. The total Chern number of a system is given by the bulk-boundary correspondence  $C = \sum_m C_m$ , which is found by summing over all occupied bands  $m$ . TKNN compared the Chern number and the quantized Hall conductivity  $\sigma_{xy}$ , calculated via the Kubo formula, and showed that the Chern number  $C$  is equal to the number of filled Landau levels  $n$ . This observation also explains why the quantized conductivity is robust: the Chern number is a quantized value and cannot change when the Hamiltonian is smoothly varied.

In principle, a Chern number can indeed be calculated for the bulk Hamiltonian for topological phases. In a similar way as above, the Chern number explains the quantized conductivity in the quantum spin Hall effect, and therefore  $C$  is a topological invariant that can be used to differentiate the topological phase from the trivial phase. This means that one

can retrieve information about the boundary (edge modes) via the bulk, because when there is a nonzero Chern number, the system is in a topological phase. This is often referred to as the bulk-boundary correspondence.

#### 2.1.4 Topological insulators in 2D

Now we have seen an example with a topological and trivial phase and how topological invariants can be calculated, we consider different types of topological insulators that have had a great impact in the past years. In 2D, these are the Kane-Mele model for graphene and the 2D Bernevig-Hughes-Zhang (BHZ) model. The Kane-Mele model was already introduced together with the quantum spin Hall effect. Here, we will show what the model looks like and why it indeed gives the required result of two copies of the quantum Hall effect, one for spin up and one for spin down. Next, we consider the BHZ model, which is developed shortly after the Kane-Mele model to measure the quantum spin Hall effect.

**The Kane-Mele model** The Kane-Mele model predicts a quantum spin Hall effect in graphene. In the time when the model was developed, graphene already had a good model to account for the honeycomb lattice and the massless Dirac fermions in the system. This model was developed by Haldane in 1988, who introduced the spinless Hamiltonian

$$H_{\text{Haldane}} = \sum_{\langle ij \rangle} t c_i^\dagger c_j + m \sum_i \epsilon_i c_i^\dagger c_i + t_2 \sum_{\langle\langle ij \rangle\rangle} e^{-i\nu_{ij}\phi} c_i^\dagger c_j, \quad (2.31)$$

where the first term describes the nearest-neighbor hopping with amplitude  $t$ , the second describes a staggered on-site potential  $m$  with opposite signs  $\epsilon_i = \pm 1$  for sublattices  $A$  and  $B$ , and the third describes the next-nearest neighbor (NNN) hopping, where  $\nu_{ij} = -\nu_{ji} = \pm 1$  are clock- or counter-clockwise electron hoppings and a flux  $\phi$  which sums up to zero over each unit cell [35]. This model was able to describe a quantum Hall effect without the Landau level structure in graphene. Moreover, the first term describes the famous Dirac cones in graphene. By calculating the energy bands for this term, one obtains a linear dispersion at the points  $K$  and  $K'$ , the analogues of sublattices  $A$  and  $B$  in reciprocal space. This dispersion is exactly the same as the one obtained for a massless relativistic fermion in a 1D Dirac equation, hence the name Dirac cone. These Dirac cones are frequently observed in the quantum spin Hall effect, because as the bands invert, the energy spectrum has a Dirac cone. In 3D topological insulators, these Dirac cones have been observed via ARPES, which we will encounter in Sec. 2.2.3.

Especially the last term is important for the quantum spin Hall effect, the NNN-hopping, since it breaks the time-reversal symmetry without using a magnetic field. Following Haldane, we define lattice vectors between the NNN sites such that  $b_1 = \delta_2 - \delta_3$ ,  $b_2 = \delta_3 - \delta_1$  and

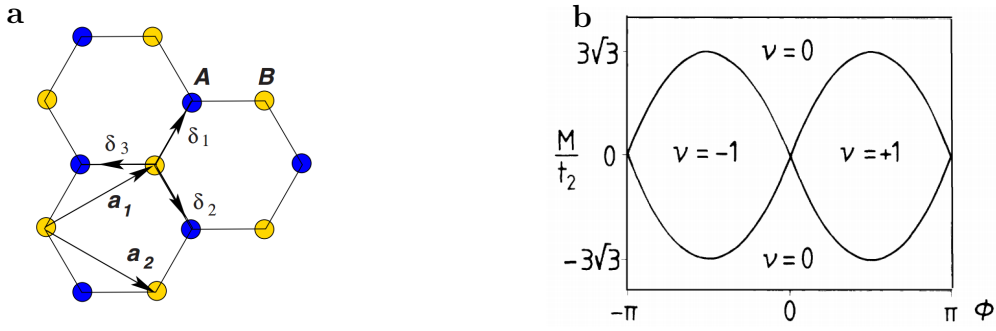


Figure 2.14: **a** Graphene is often displayed in a honeycomb lattice, both in real space as in reciprocal space, leading to interesting properties. Figure adapted from [36]. **b** The Chern number  $\nu$  for the topological phase ( $\nu = \pm 1$ ) and the trivial phase ( $\nu = 0$ ). The phase transition occurs at the Haldane mass  $m = \pm 3\sqrt{3}t_2 \sin(\phi)$ . In the figure, Haldane used  $M$  instead of  $m$  [35].

$b_3 = \delta_1 - \delta_2$  (see Fig. 2.14), and we rewrite Eq. (2.31) in  $k$ -space

$$H(k) = 2t_2 \cos(\phi) \left[ \sum_i \cos(k \cdot b_i) \right] \mathbb{1} + t \left[ \sum_i [\cos(k \cdot \delta_i) \sigma_x + \sin(k \cdot \delta_i) \sigma_y] \right] + \left[ m - 2t_2 \sin(\phi) \left[ \sum_i \sin(k \cdot b_i) \right] \right] \sigma_z, \quad (2.32)$$

with  $\sigma_i$  the usual Pauli matrices. Haldane shows that there is now a lifted degeneracy in the bands when either  $m$  or  $2t_2 \sin(\phi)$  is nonzero (the last term of Eq. (2.32)). More explicitly, the  $\sigma_z$ -contribution changes the sign between the different valleys  $K$  and  $K'$  (in reciprocal space), which breaks the time-reversal symmetry and opens a gap in the energy spectrum. Hence, a phase transition occurs between a trivial phase and a topological phase, and one can show that this happens exactly at the Haldane mass  $m = \pm 3\sqrt{3}t_2 \sin(\phi)$  by calculating the Chern number (see Fig. 2.14). Therefore, without using a magnetic field to break time-reversal symmetry, there exists topological phases in graphene when considering NNN-hopping.

Moreover, the Hamiltonian of Eq. (2.32) can be rewritten in the Bloch form  $H(k) = h(k) \cdot \sigma$ , and this can be used to interpret the Hall conductivity in this model. As was the case for the Kitaev chain, the Chern number for these kind of systems can be seen as a winding number (but now in  $2D$ )

$$n = \frac{1}{4\pi} \int d^2 k \hat{h} \cdot \left[ \frac{\partial \hat{h}}{\partial k_x} \times \frac{\partial \hat{h}}{\partial k_y} \right], \quad (2.33)$$

where  $n$  is the winding number and  $\hat{h} = h(k)/|h(k)|$  is a unit vector. In the insulating state, the sum of the winding numbers cancels and therefore there is no quantized current, but in the

quantum Hall state, the winding numbers add and contribute to the conductivity  $\sigma_{xy} = e^2/h$ .

Kane and Mele were inspired by this work to make a double copy of the model, by introducing spin in the system, eventually leading to the spin quantum Hall effect [4]. This quantum spin Hall effect differs from the quantum Hall effect by Haldane because it is *invariant* under time-reversal symmetry and gives rise to helical, counter-propagating spin currents at the edge. A simple way to describe the model of Kane and Mele is to have the Haldane model for a spin up and a spin down

$$H = \begin{pmatrix} H_{\uparrow} & 0 \\ 0 & \mathcal{T}H_{\uparrow}\mathcal{T}^{-1} \end{pmatrix}, = \begin{pmatrix} H_{\uparrow} & 0 \\ 0 & H_{\downarrow} \end{pmatrix} = \begin{pmatrix} H_{\text{Haldane}}(\phi = -\pi/2) & 0 \\ 0 & H_{\text{Haldane}}^*(\phi = \pi/2) \end{pmatrix}, \quad (2.34)$$

where  $\mathcal{T}$  is the time reversal operator. The time-reversal operator essentially does two things: it complex conjugates the wave-function and flips the spin, and this is indeed invariant for the Hamiltonian in Eq. (2.34). The Hamiltonian in Eq. (2.31) is recast due to this spin

$$H_{\text{KM}} = \sum_{\langle ij \rangle \alpha} t c_{i\alpha}^{\dagger} c_{j\alpha} + m \sum_i \epsilon_i c_i^{\dagger} c_i + it_2 \sum_{\langle\langle ij \rangle\rangle \alpha\beta} \nu_{ij} \sigma_{\alpha\beta}^z c_{i\alpha}^{\dagger} c_{j\beta}, \quad (2.35)$$

where the third term now describes the intrinsic spin-orbit coupling (SOC), with  $t_2$  the SOC parameter,  $\sigma^z$  a Pauli matrix representing the electron's spin and  $\nu_{ij} = -\nu_{ji} = \pm 1$  still describes clock- or counter-clockwise electron hopping. In the original model, also a Rashba term is included, but this term is omitted in our case since it is not necessary to describe the quantum spin Hall effect.

Whereas the quantum Hall effect gives rise to chiral edge states, here we will get two copies of these chiral edge states for different spins, leading towards a so-called helical edge state. Edge states come in so-called Kramers pairs that are derived from Kramers' theorem. The theorem proves that all eigenstates of a time-reversal invariant Hamiltonian are at least two-fold degenerate. States with an even number of Kramers pairs of edge states at one edge are considered to be topologically trivial, and with an odd Kramers pair nontrivial. The spectrum of Eq. (2.35) can be calculated by considering a strip of graphene and is shown in Fig. 2.15. We see the normal energy bands, but also a crossing of two bands at  $k_x = \pi/a$ . These crossing bands are the spin up and spin down electrons at the edge of the system, and are propagating in opposite direction (the speed can be determined via the slope of the energy band).

The SOC-term allows for a mass inversion within a valley  $K$  or  $K'$  (which breaks time-reversal symmetry in one valley, just as in the Haldane model), whereas the total electronic system is time-reversal invariant. This was also shown in Fig. 2.6, where the inversion of the bands gives rise to the helical edge states. For this to happen, the SOC must

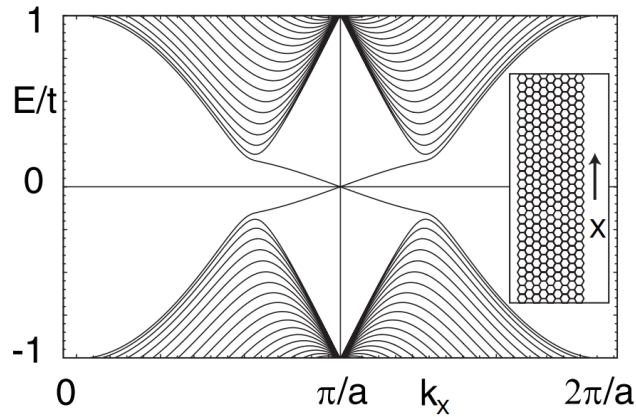


Figure 2.15: The energy spectrum of the Kane-Mele model for a strip of graphene for  $t_2/t = 0.03$  [4]. One can easily observe the counter propagating edge states that cross at  $k_x = \pi/a$  and zero energy. At  $E = 0$ , the edge states have a linear dispersion, making these electrons behave as Dirac fermions.

be large enough. Unfortunately, this was not the case in graphene. The most promising materials are those that are heavy elements and have a small band gap. The SOC is a relativistic effect and is strong for heavy elements, and furthermore, if the band gap is too large, the SOC is not able to close the gap and induce a phase transition [37]. Therefore, only specific materials have chiral edge states, and quickly after this prediction by Kane-Mele, the first topological insulator was found in the form of a quantum well.

**The Bernevig-Hughes-Zhang model** Not more than a year later, a new material was proposed by Bernevig, Hughes and Zhang (BHZ) that might have the required band inversion and, indeed, the quantum spin Hall effect was measured a year later by the group of Molenkamp [9, 11]. In a slightly different way, BHZ show how in a 2D mercury telluride (HgTe)-cadmium telluride (CdTe) quantum well the bands invert for a critical thickness  $d = d_c$  and predicted the first experimentally verified topological insulator.

The system is shown in Fig. 2.16, where the CdTe acts as a semiconductor and HgTe is a semimetal between two plates of CdTe. The crucial point is that both materials have a s-type  $\Gamma_6$  and a p-type  $\Gamma_8$  band, where in CdTe the  $\Gamma_6$  is above the  $\Gamma_8$  and in HgTe these bands are inverted (see Fig. 2.16). In both materials, the energy gap between the bands is the smallest near the high-symmetry  $\Gamma$  point in the Brillouin zone (the  $k = 0$  point in the  $x$ -axis). Leaving the other present band, the  $\Gamma_7$  out of the picture, BHZ wrote down a six-band model for this system, with spin up and down for the s-band and  $J = 1/2$  and  $J = 3/2$  spins for the p-band, where  $J$  is the total angular momentum.

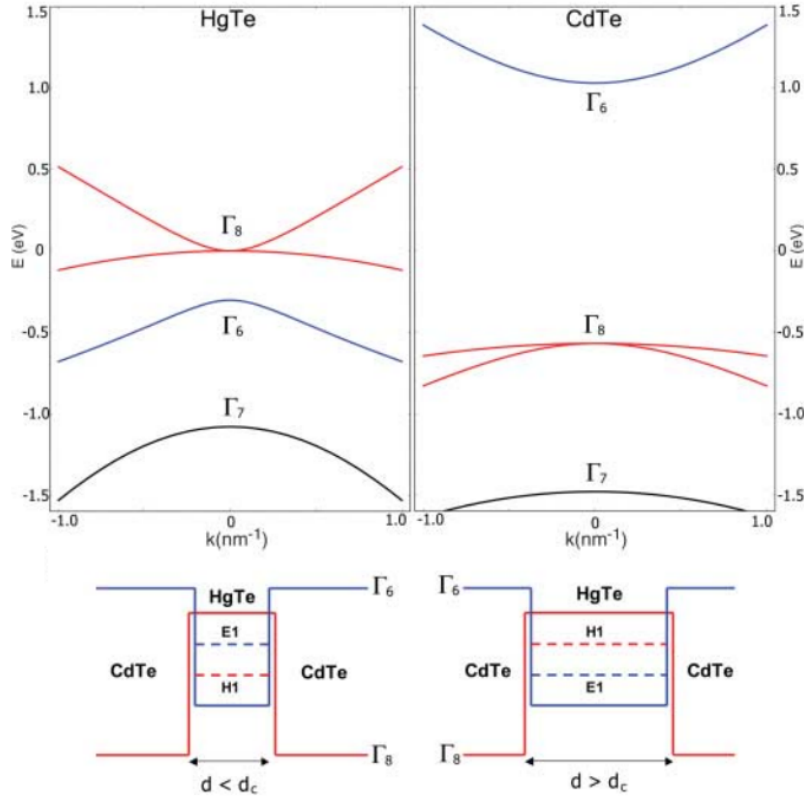


Figure 2.16: The band inversion for CdTe/HgTe quantum well [9]. Above, we see the energy bands  $\Gamma_6$ ,  $\Gamma_7$  and  $\Gamma_8$  for HgTe (left) and CdTe (right). Below, we see the increasing thickness of the quantum well, making  $\Gamma_6$  and  $\Gamma_8$  bands invert due to the presence of more HgTe or CdTe. This inversion takes place at a critical thickness  $d_c$ .

The corresponding six-components spinor can be written as

$$\Psi = (|\Gamma_6, 1/2\rangle, |\Gamma_6, -1/2\rangle, |\Gamma_8, 3/2\rangle, |\Gamma_8, 1/2\rangle, |\Gamma_8, -1/2\rangle, |\Gamma_8, -3/2\rangle). \quad (2.36)$$

A little bit before, results by the group of Molenkamp in Würzburg had shown that this combination of materials has three important energy bands derived from a six-band Kane model:  $|E1\pm\rangle$ ,  $|H1\pm\rangle$  and  $|L1\pm\rangle$  [38, 39]. The  $|E1\pm\rangle$  band corresponds to mixing of the spin  $\pm 1/2$  electrons in both  $\Gamma$  bands, and the  $|H1\pm\rangle$  is formed from the spin  $3/2$  of the  $\Gamma_8$ . By analyzing the band structure, it turns out that the  $|E1\pm\rangle$  and the  $|H1\pm\rangle$  energies have a band crossing, whereas the  $|L1\pm\rangle$  band is separated from the other two.

BHZ construct an effective Hamiltonian, based on the even parity of the  $|\Gamma_6, \pm 1/2\rangle$  and odd parity of the  $|\Gamma_8, \pm 3/2\rangle$  states under two-dimensional spatial reflection, and write down an effective Hamiltonian in the basis of the energy bands  $|E1, \pm 1/2\rangle$  and  $|H1, \pm 3/2\rangle$ . The

low-energy dynamics of the model is given by the time-reversal invariant Hamiltonian

$$H_{\text{eff}}(k_x, k_y) = \begin{pmatrix} H(k) & 0 \\ 0 & H^*(-k) \end{pmatrix}, \quad (2.37)$$

where

$$H(k) = \epsilon(k) + d_i(k)\sigma_i. \quad (2.38)$$

This Hamiltonian can be considered as a Taylor expansion (low-energy behavior) with respect to the in-plane wave vectors  $k_x$  and  $k_y$ . The whole Hamiltonian satisfies the constraining parity and time-reversal symmetries. From the even/odd parity, we can deduce that  $d_3(k)$  is an even function of  $k$  and  $d_1(k)$  and  $d_2(k)$  are odd functions of  $k$ . In general, we can write

$$d(k) = (Ak_x, Ak_y, M - B(k_x^2 + k_y^2)), \quad \epsilon(k) = C - D(k_x^2 + k_y^2), \quad (2.39)$$

where  $A$ ,  $B$ ,  $C$ ,  $D$ , and  $M$  are parameters of the model.

The inversion of the  $|E1\rangle$  and  $|H1\rangle$  bands is tuned by the parameter  $M$ , which changes sign for a critical thickness  $d_c$  of the quantum well. The quantum well is in the normal state if the CdTe is predominant, where  $E(\Gamma_6) > E(\Gamma_8)$ . As the quantum well thickens, the HgTe contribution becomes more dominant, making the  $|E1\rangle$  and  $|H1\rangle$  bands invert. At this transition point, no other bands interfere with these bands, making this model by tuning the thickness of the layer and inverting the bands sufficient to predict the quantum spin Hall effect in these type of quantum wells.

To explicitly show the emergence of the spin quantum Hall effect in the quantum wells, BHZ also calculate the quantum Hall conductance (which is related to the Chern number)

$$\sigma_{xy} = -\frac{e^2}{8h\pi^2} \iint dk_x dk_y \hat{d} \cdot \partial_x \hat{d} \times \partial_y \hat{d}, \quad (2.40)$$

which is the integral over the Brillouin zone of the unit vector  $\hat{d}$  of the vector  $d(k)$ . However, the  $d(k)$  in Eq. (2.39) is a Taylor expansion around the  $\Gamma$ -point, and therefore one needs to write down an expression, which is a tight-binding description of the same model, and in the lowest order expansion reduces to Eq. (2.39). The tight-binding model still contains time-reversal symmetry and its elements are

$$d(k) = (A \sin(k_x), A \sin(k_y), M - 2B [2 - \cos(k_x) - \cos(k_y)]) \quad (2.41)$$

$$\epsilon(k) = C - 2D [2 - \cos(k_x) - \cos(k_y)]. \quad (2.42)$$

With this description, one can calculate the Hall conductivity, and, by introducing a cut-off for the momentum at some finite point, we obtain for the spin-up electrons the quantized conductance  $\sigma_{xy} = e^2/(2h)\text{sign}(M)$ . At the phase transition,  $M$  changes sign, leading towards a total difference  $\Delta\sigma_{xy} = e^2/h$  between the trivial and topological phase. Due to the spin-down electrons, we get another contribution in  $\sigma_{xy}$ , resulting in a helical quantized edge current with  $\Delta\sigma_{xy} = 2e^2/h$ , which is indeed the correct value of the quantum spin Hall effect. In Sec. 2.2.2, we show how this effect was indeed measured in transport experiments a year later.

### 2.1.5 Topological insulators in 3D

Quickly after the theoretical prediction of the 2D topological insulator, a theoretical formulation for 3D topological insulators was made. Although the quantum Hall effect does not extend towards 3D, the quantum spin Hall effect does in a rather particular sense. In the summer of 2006, three different groups were able to identify the existence of a natural continuation of the 2D quantum spin Hall effect in 3D [40, 41, 27]. It turns out that there exist two types of topological insulators, the weak and the strong, and these also have been identified experimentally, with the material  $\text{Bi}_{1-x}\text{Sb}_x$  arising as first experimentally tested one.

These 3D topological insulators are characterized via four  $\mathbb{Z}_2$  topological invariants  $(\nu_0; \nu_1, \nu_2, \nu_3)$ , leading towards a total of 16 different types. The weak topological insulator is the one which is the easiest to understand with the previous discussion in mind. By layering 2D quantum spin Hall systems onto each other, a 3D one appears, where we can identify a  $\mathbb{Z}_2$  topological invariant for every  $x, y, z$  direction. Unfortunately, this type of topological insulator is not robust in the presence of disorder, and the physics does not change in the procedure of going 3D. However, it offers an interesting way to experimentally verify 2D physics in a 3D system. In this type of materials, a dislocation (a line-like defect) always gives rise to quantum wire in which helical spin currents flow just like in the quantum spin Hall effect. Weak topological insulators are characterized by  $\nu_0 = 0$ , whereas the other invariants can be interpreted to describe the orientation of the layers and whether these are topological or not.

In contrast, the strong topological insulator is characterized by  $\nu_0 = 1$ . A strong topological insulator is not simply layering 2D topological materials, but makes use of the band inversion and the time-reversal symmetry. In this way, we do not obtain a 1D helical edge current, but a 2D, topologically protected metallic surface. Also the dispersion relation of the Dirac fermions can be extended toward the so-called Dirac cone, which is now located at the surface of the material. In the simplest case, the Fermi circle (the 2D analogue of the Fermi level) encloses one Dirac cone at a surface. The surface structure can be compared with the Dirac cones in graphene. In contrast with graphene, which has four Dirac cones, a topological

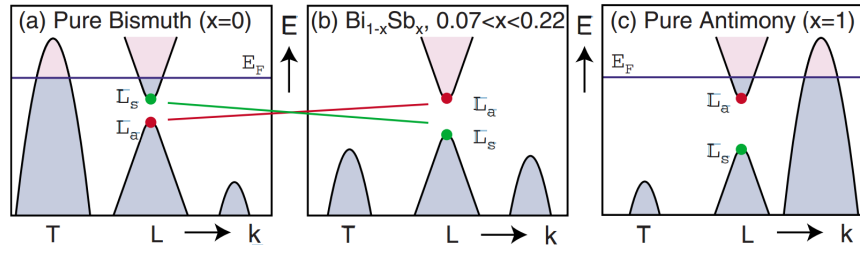


Figure 2.17: The band inversion in 3D  $\text{Bi}_{1-x}\text{Sb}_x$ . When changing the amount of bismut (Bi) and antimony (Sb), changing the value of  $x$  in previous subscript, a band inversion occurs between the bands  $L_s$  and  $L_a$  around  $x \approx 0.04$  [5]. The energy bands show the transition from a semimetal (a) to a semiconductor (b), and again back to the semimetal (c) for different values of  $x$ .

insulator has only one Dirac cone at opposing surface (making a pair of two Dirac cones in total). This isolation of a single Dirac cone had not been observed before and is perhaps one of the most interesting properties of a strong topological insulator.

The surfaces in a strong topological insulator are considered to be topological metals [5, 40]. This metal is half an ordinary metal, because in an ordinary metal the spin states are degenerate, and this is no longer the case in a topological metal. In a topological metal, time-reversal symmetry is protected, making the electrons with spin up orbiting in opposite direction from the spin down electrons around the Fermi surface. As an electron goes around the Fermi surface, it picks up a non-trivial Berry phase, which is either  $0$  or  $\pi$ . When an electron circles around a Dirac point, it obtains a phase of  $2\pi$ , leading to a non-trivial Berry curvature  $\pi$  in the topological phase.

It did not take long before the first strong 3D topological insulator was discovered:  $\text{Bi}_{1-x}\text{Sb}_x$ . This material was theoretically predicted by Fu and Kane [42] and measured via ARPES by the group of Hasan in Princeton [12], who happened to research the specific material already due to its interesting thermo-electric properties. By changing the material from more bismut (Bi) to more antimony (Sb), a band inversion takes place as is depicted in Fig. 2.17. The bands  $L_s$  and  $L_a$  invert for  $x \approx 0.04$ , and therefore a topological phase transition occurs near this point.

The calculation of the band energies was rather complex, and therefore new strong topological insulators were proposed in a quick pace. The second generation of topological insulators was more simple. The general model was proposed by Zhang et al. [43] in 2009. By using a similar Hamiltonian as BHZ, they were able to find a simple construction of the energy bands. In

reciprocal space, the Hamiltonian reads

$$H_{\text{BHZ}}(\mathbf{k}) = \epsilon_0(\mathbf{k})\mathbb{1}_{4 \times 4} + \begin{pmatrix} M(\mathbf{k}) & A_2(k_x + ik_y) & 0 & A_1k_z \\ A_2(k_x - ik_y) & -M(\mathbf{k}) & A_1k_z & 0 \\ 0 & A_1k_z & M(\mathbf{k}) & -A_2(k_x - ik_y) \\ A_1k_z & 0 & -A_2(k_x + ik_y) & -M(\mathbf{k}) \end{pmatrix}, \quad (2.43)$$

where  $\epsilon(\mathbf{k}) = C + D_1k_z^2 + D_2(k_x^2 + k_y^2)$ ,  $M(\mathbf{k}) = M - B_1k_z^2 - B_2(k_x^2 + k_y^2)$  and  $M$ ,  $A_1$ ,  $A_2$ ,  $B_1$ ,  $B_2$ ,  $C$ ,  $D_1$  and  $D_2$  are constant parameters in the model. The expression is based on the time-reversal, inversion symmetry and three-fold rotation symmetry in the  $z$ -axis. This is exactly the same Hamiltonian in low approximation as the 2D BHZ Hamiltonian, except for the terms  $A_1k_z$  on the anti-diagonal, which describe the third dimension  $k_z$ . By rewriting Eq. (2.43) into a tight-binding description, the energy bands were calculated and shown to have a band inversion at  $M = 0$ . About the same period of time, multiple concurrent groups, under which the one of Hasan, measured these band energies by using ARPES. This is described in more detail in Sec. 2.2.3.

We have seen in historical context the research in topological insulators, starting from the quantum (spin) Hall effect towards 3D strong topological insulators. Before going into the important experiments that have been done to identify these materials and the Dirac cones, we first consider one of the most important schemes to classify topological materials nowadays: the tenfold way.

### 2.1.6 The tenfold way

The tenfold way is an exhaustive classification scheme that can be used to identify which class of topological insulator (superconductor) one is describing with a certain Hamiltonian and what kind of topological behavior can be expected. The key ingredient in this scheme are the symmetries of the model. As we have seen for the Kitaev chain, the model has an intrinsic particle-hole symmetry that protects the Majorana bound-states and in the quantum spin Hall effect, time reversal symmetry is protected for the whole system. By considering these types of symmetry for the Hamiltonian, it is possible to identify the class and whether there is no topological phase (0), a topological and a trivial phase (a  $\mathbb{Z}_2$  quantity) such as in the Kitaev chain, or a number of topological phases (a  $\mathbb{Z}$  quantity) such as in the Quantum Hall effect. We will describe the symmetries at stake and how these symmetries can be used to find the correct number of topological phases of a given model.

The tenfold way characterization is based on the work by Altland and Zirnbauer in 1997, who recognized the similarities between all the possible symmetry classes of single-particle Hamiltonians and the set of large symmetric spaces of the mathematician Cartan in 1926 [44].

When topological insulator and their symmetry protected boundary states came into play, this work was extended to different dimensions in Schnyder et al. [28] (up to three dimensions) and to arbitrary dimensions via K-theory by Kitaev [29].

As mentioned, the tenfold way is based on the symmetries of the Hamiltonian [31]. What symmetries do we need to consider? When we look at the Kitaev chain, we could have easily added some extra perturbations that violate translational symmetry to obtain the topologically distinct nature, so the Hamiltonian is not translational invariant. This holds for all gapped Hamiltonians, and therefore translational invariance is not a protecting symmetry for topological insulators. This means that a classification scheme must include translationally not invariant Hamiltonians, thus one cannot rely on the ordinary symmetries, unitary operators, that commute with the Hamiltonian. However, one can rely on the anti-unitary operators, and by considering all symmetries that commute with the Hamiltonian, it is always possible to write down the Hamiltonian in a block form. It turns out that there exist only 10 symmetry-less, also called irreducible, Hamiltonians in this sense. The two important symmetries are anti-unitary operators, the time-reversal and charge-conjugation (particle-hole), when acting on the single particle Hilbert space. In second-quantization, we can always rewrite the Hamiltonian for a topological insulator in the following form

$$H = \sum_{A,B} \psi_A^\dagger \mathcal{H}_{A,B} \psi_B, \quad (2.44)$$

where  $A$  and  $B$  denote the sum over all lattices, and if relevant also the spin or other quantum numbers, and  $H_{A,B}$  is the first quantized  $N \times N$  block matrix for  $N$  sites. We have also seen that for the Kitaev chain, a similar expression was available via the Bogoliubov transformations. This holds in general for all superconductors.

The interesting question now is how time-reversal ( $\mathcal{T}$ ) and particle-hole ( $\mathcal{C}$ ) symmetry can be seen in these systems. A system is invariant under  $\mathcal{T}$  if and only if the complex conjugate of the first quantized Hamiltonian  $\mathcal{H}^*$  is equal to  $\mathcal{H}$  up to a unitary rotation  $U_{\mathcal{T}}$ . This can be exemplified by

$$U_{\mathcal{T}}^\dagger \mathcal{H}^* U_{\mathcal{T}} = \mathcal{H}. \quad (2.45)$$

A system is invariant under particle-hole symmetry if and only if the complex conjugate of the Hamiltonian  $\mathcal{H}^* = \mathcal{H}^T$  is equal to minus  $\mathcal{H}$  up to a unitary rotation  $U_{\mathcal{C}}$ . This is given by

$$U_{\mathcal{C}}^\dagger \mathcal{H}^* U_{\mathcal{C}} = -\mathcal{H}. \quad (2.46)$$

When taking these two symmetries into account, there are only ten possible ways for a system

*complex case:*

Cartan\ $d$	0	1	2	3	4	5	6	7	8	9	10	11	...
A	$\mathbb{Z}$	0	...										
AIII	0	$\mathbb{Z}$	...										

*real case:*

Cartan\ $d$	0	1	2	3	4	5	6	7	8	9	10	11	...
AI	$\mathbb{Z}$	0	0	0	$2\mathbb{Z}$	0	$\mathbb{Z}_2$	$\mathbb{Z}_2$	$\mathbb{Z}$	0	0	0	...
BDI	$\mathbb{Z}_2$	$\mathbb{Z}$	0	0	0	$2\mathbb{Z}$	0	$\mathbb{Z}_2$	$\mathbb{Z}_2$	$\mathbb{Z}$	0	0	...
D	$\mathbb{Z}_2$	$\mathbb{Z}_2$	$\mathbb{Z}$	0	0	0	$2\mathbb{Z}$	0	$\mathbb{Z}_2$	$\mathbb{Z}_2$	$\mathbb{Z}$	0	...
DIII	0	$\mathbb{Z}_2$	$\mathbb{Z}_2$	$\mathbb{Z}$	0	0	0	$2\mathbb{Z}$	0	$\mathbb{Z}_2$	$\mathbb{Z}_2$	$\mathbb{Z}$	...
AII	$2\mathbb{Z}$	0	$\mathbb{Z}_2$	$\mathbb{Z}_2$	$\mathbb{Z}$	0	0	0	$2\mathbb{Z}$	0	$\mathbb{Z}_2$	$\mathbb{Z}_2$	...
CII	0	$2\mathbb{Z}$	0	$\mathbb{Z}_2$	$\mathbb{Z}_2$	$\mathbb{Z}$	0	0	0	$2\mathbb{Z}$	0	$\mathbb{Z}_2$	...
C	0	0	$2\mathbb{Z}$	0	$\mathbb{Z}_2$	$\mathbb{Z}_2$	$\mathbb{Z}$	0	0	0	$2\mathbb{Z}$	0	...
CI	0	0	0	$2\mathbb{Z}$	0	$\mathbb{Z}_2$	$\mathbb{Z}_2$	$\mathbb{Z}$	0	0	0	$2\mathbb{Z}$	...

Figure 2.18: The tenfold way to identify topological insulators and superconductors, as shown in Ref. [31]. The class is indicated by the Cartan label and  $d$  stands for the dimension of the model. The symmetry classes are divided in a complex and real case to distinguish whether the Hamiltonian is complex or if reality conditions are imposed on it. The system either has no topological state (0), a topological or trivial state ( $\mathbb{Z}_2$ ), or an integer number of topological phases ( $\mathbb{Z}$ )

to respond to them, which is characterized by the tenfold way. In this language, the Hamiltonian can not be time-reversal invariant ( $T = 0$ ), or can be time-reversal invariant ( $T = \pm 1$ ). The  $\pm 1$  here indicates that the time reversal operator  $\mathcal{T}$  squares either to  $+1$ , or  $-1$ . This is also the case for the particle-hole symmetry, which is  $C = 0$  for a system which has no particle-hole symmetry or  $\pm 1$  for a system that has this symmetry. In this way, nine possibilities are obtained. The last one can be found by the multiplication of the two symmetries,  $\mathcal{S} = \mathcal{T} \cdot \mathcal{C}$ , which is referred to as the chiral, or sublattice symmetry. Only for the case where  $\mathcal{T} = 0$  and  $\mathcal{C} = 0$ , the chiral symmetry is not determined by the behavior of the time-reversal and particle-hole symmetry, making in total ten options available when considering these symmetries. The tenfold way is summarized for different dimensions in Fig. 2.18.

The table represents the label of the topological insulator (superconductor) for the symmetries that are incorporated in the system. In the table, the 8-fold periodicity of the symmetries for the real case is visible. This periodicity arises from the 8-fold spinor periodicity of the orthogonal groups  $SO(N)$ , and is called the Bott periodicity [31]. Furthermore, the topological insulators appear upon the diagonal lines of the table, and this can be related to homotopy groups. When one knows which symmetries are in the Hamiltonian, it is possible to derive from the table whether there is a topologically protected phase.

The tenfold way is the standard way to classify topological phases. At the moment, this table is pretty well-understood and describes the Cartan label for non-interacting topological systems, based on the time-reversal and particle-hole symmetries. Therefore, current challenges are in example to extend this table towards interacting systems. Also other extensions have been made to accompany other symmetries in the tenfold way by for instance including the crystal-lattice symmetries [45], or inversion symmetries [31]. In this sense, there is still a lot to uncover within this procedure.

## 2.2 Experiments on topological materials

A very important part of the research of topological insulators are the experiments. Due to the immediate response of several research groups on the theoretical predictions, the existence of these interesting materials was confirmed very quickly, which in its turn encouraged to develop and detect more and new types of topological insulators (such as the strong topological insulator). Especially the group of Laurens Molenkamp in Würzburg (transport) and the group of M. Zahid Hasan in Princeton (ARPES) were very influential due to their discovery of the 2D and 3D topological insulator. In this section, we will describe the most important measurement techniques currently available. In our analysis, we focus on scanning tunneling microscopy (STM), because this is the method that is used to obtain the local density of states. With the use of Hill thermodynamics (see Sec. 3), we calculate the density of states for the 2D Kane-Mele and BHZ model in Sec. 5, which might be measurable using STM.

In the next part, we start with a description of STM. Then, we again follow the historical route, and discuss the use of transport and how the group of Molenkamp was able to verify the existence of the quantum spin Hall effect. Finally, we go 3D and summarize the main findings of ARPES for the strong topological insulator.

### 2.2.1 Scanning Tunneling Microscopy (STM)

A method largely employed for experimentally detecting topological phases is Scanning Tunneling Microscopy (STM), a specific branch of Scanning Tunneling Spectroscopy (STS). STM and STS have largely contributed to our understanding and experimental verification of conventional superconductivity, and in more recent years also of high- $T_c$  superconductivity [46]. STM originates from the tunneling of electrons through insulating barriers between two electrodes. The number of electrons which tunnels through the barrier depends on the thickness of the insulating gap and on the electronic structure of the electrodes. When the thickness of the gap is known, one can measure the tunneling current and obtain information about the electronic structures of the electrodes. In this way, STM provides information

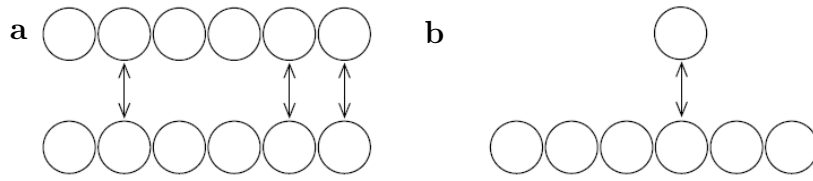


Figure 2.19: **a** Sketch of a planar-junction, where it is not possible to identify the underlying atomic structure because electrons can tunnel between the material at different sites. **b** Sketch of a point-junction where it is possible to identify the underlying atomic structure since electrons can only tunnel near the probe. Image retrieved via Ref. [50].

about the underlying topography and atomic structure of the materials. Moreover, one can measure the local electron density of states (LDOS) by using this technique.

The first experiment in which quasiparticle tunneling was used is a famous experiment in 1960 performed by Ivar Giaever. He investigated the electronic structure of low- $T_c$  superconductors, for which he later received the Nobel Prize in 1973 [47], using an aluminum and a lead sheet separated by an aluminum oxide plane. By varying the bias-voltage, he was able to measure the differential tunneling conductance. The metals can either be in a superconducting or in a normal state, and by varying the magnetic field, which controls whether lead is in a superconducting state or not, he confirmed the BCS theory by showing that the tunneling conductance of lead had a functional dependence on the bias-voltage.

The first experiments concerning tunneling were done with two systems of approximately the same size, in which tunneling was possible between the two materials. This so-called planar junction, which is shown in Fig. 2.19a, can only provide information on the bulk of the materials, since it is not possible to determine from which (lattice) site the electrons are tunneling. This all changed in 1982, the year STM was invented by Binnig and Rohrer [48, 49]. Their new method opened up new possible applications within STS, for which they later were awarded the Nobel Prize. Within STM, the planar junction is replaced by a point-contact junction of ideally one atomic width, which is shown in Fig 2.19b. In this way, the probe with the point-contact junction allows one to determine more precise where the atoms tunnel. This new method enormously improved the resolution of the underlying atomic structure of a material.

STM especially showed its value in researching high- $T_c$  superconductors [46]. After the discovery of high- $T_c$  superconductors, it was clear that the superconductivity of these systems differs from low- $T_c$  superconductors. Experimentally, it was quite clear that STS was one of the most promising techniques to investigate these high- $T_c$  superconductors in more detail.

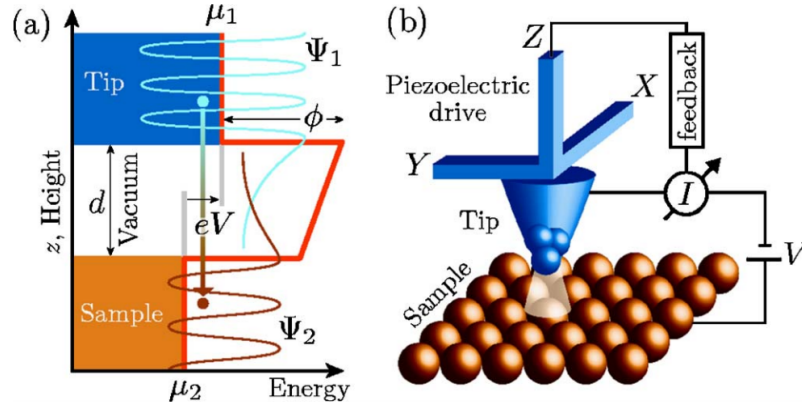


Figure 2.20: Graphical representation of an experimental STM setup. (a) Tunneling process between the tip and the sample through a vacuum barrier of width  $d$  and height  $\phi$ . The electron wave functions  $\Psi$  decay exponentially in the vacuum, but still overlap, which means that electrons can tunnel to the other system. (b) The metallic tip of the probe scans the sample. Due to the piezoelectric drive, the probe can move over small distances above the sample and determine the local atomic distribution [46].

However, due to the poor control of the tunnel barrier and material inhomogeneities, it was difficult to use a planar-junction for this research. On the other hand, STM was able to handle these difficulties and experiments resulted in reproducible spectra for high- $T_c$  superconductors [51]. Another major breakthrough in STM occurred when the distance between the tip of the probe and the sample reached picometric precision [46].

The principle of STM is based on the tunneling of electrons, see Fig. 2.20a. The electron wave-functions of the metals decay exponentially into the vacuum, but have a small overlap due to which the electrons can tunnel to the other material. This tunneling induces a current, which can be measured. STM uses a sharp metallic tip on a piezoelectric metallic drive, as displayed in Fig. 2.20b. The tip is used as a probe and can be controlled in the X and Y directions to scan the sample and in the Z direction to adjust the height from the sample. The tunneling regime depends on the following parameters: the tunneling current  $I$  ( $\sim 0.01$ - $10$  nA), the bias voltage  $V$  ( $\sim 0.01$ - $2$  V) and the electrode spacing  $d$  ( $\sim 5$ - $10$  Å), although only relative height differences between the tip of the probe and the sample can be measured. The main result of an STM experiment is the differential tunneling conductance  $dI/dV$ . By following similar steps as done in Ref. [50], we can find that

$$\frac{dI}{dV} \propto - \int_{-\infty}^{\infty} d\omega \sum_{k_x k_y} |T_k|^2 A(k, \omega) \frac{\partial N_{\text{FD}}(\omega - eV)}{\partial \omega}, \quad (2.47)$$

where  $T_k$  is the tunneling matrix element, which depends on the spectral function of the probe,  $A(k, \omega)$  is the spectral function of the sample, and  $N_{\text{FD}}$  is the Fermi-Dirac distribution.

This expression basically states that the differential tunneling conductance depends on the local density of states in one system and the availability of states in the other system. Furthermore,  $A(k, \omega)$  is local single particle density of states and is the imaginary part of the retarded Green's function. For the remainder of this section, we will follow the theoretical calculations that can be found in Refs. [46, 50] to determine Eq. (2.47).

An STM experiment consists of two independent systems that interact through the tunneling of electrons between them. We introduce the Hamiltonian

$$H = H_1 + H_2 + H_T, \text{ where } H_T = \sum_{pk} [M_{pk} c_{1,p}^\dagger c_{2,k} + M_{kp}^\dagger c_{2,k}^\dagger c_{1,p}] \quad (2.48)$$

is the tunneling Hamiltonian. Furthermore, the independent systems 1 and 2 are described by  $H_1$  and  $H_2$ , which have their own creation (annihilation) operators  $c_{1,p}^\dagger$  ( $c_{1,p}$ ) and  $c_{2,k}^\dagger$  ( $c_{2,k}$ ). The tunneling Hamiltonian  $H_T$  depends on operators from both systems and the tunnel matrix element

$$M_{pk} = -\frac{\hbar^2}{2m} \int dS \left[ \psi_p^* \frac{\partial \psi_k}{\partial z} - \psi_k \frac{\partial \psi_p^*}{\partial z} \right], \quad (2.49)$$

which is the expectation value of the single particle current in the  $z$  direction (perpendicular to the plane of the sample as shown in Fig. 2.20b) through a surface  $S$ . Now, we define the tunneling current operator  $\mathcal{I}$  as the rate of change in the number of particles in one of the two systems

$$\mathcal{I} = \dot{N}_1 = i[H, N_1] = i[H_T, N_1] = -i \sum_{pk} [M_{pk} c_{1,p}^\dagger c_{2,k} - M_{kp}^* c_{2,k}^\dagger c_{1,p}] \quad (2.50)$$

to calculate the total current of the system as the average value of this tunneling current operator  $I = -e\langle \mathcal{I}(t) \rangle$ . We used that  $H_1$  and  $H_2$  commute with the number operator  $N_1$  to obtain this expression. For convenience, we can define the bosonic operator  $L$ ,

$$L = \sum_{pk} M_{pk} c_{1,p}^\dagger c_{2,k}. \quad (2.51)$$

When the two samples are far apart, the tunneling between the systems is very small. Therefore we can assume that the tunneling  $H_T$  between the two systems acts as a perturbation. We use the Kubo formula to express the linear response of the system for the observable

$$\langle \mathcal{I}(t) \rangle = \langle \mathcal{I} \rangle_0 - i \int_{-\infty}^{\infty} dt' \Theta(t-t') \langle [\mathcal{I}(t), H_T(t')] \rangle_0, \quad (2.52)$$

but we can set  $\langle \mathcal{I} \rangle_0 = 0$ , since there is no tunneling without the perturbation  $H_T$ . We

substitute Eq. (2.52) into the definition of the current  $I$ , and by using Eq. (2.51) we obtain

$$I(t) = e \int_{-\infty}^{\infty} dt' \Theta(t-t') \langle [L(t) - L^\dagger(t), L(t') + L^\dagger(t')] \rangle. \quad (2.53)$$

By identifying the terms in this expression, we observe that  $[L(t), L(t')]$  and  $[L^\dagger(t), L^\dagger(t')]$  correspond to the creation and annihilation of a pair of fermions, the Cooper pairs. Cooper pairs occur in superconducting materials, and if we setup an STM experiment without a superconducting probe, we may neglect this term. Furthermore, we know that the tunneling between the systems depends on a shift in the energy due to application of a voltage. We can express this voltage in terms of the chemical potential of the systems. To do so, we switch to the Heisenberg picture and add a chemical potential to the unperturbed Hamiltonian.

Therefore, we introduce  $K_0 = H_0 - \mu_1 N_1 - \mu_2 N_2$  and rewrite

$$e^{iK_0 t} e^{i(\mu_1 N_1 + \mu_2 N_2)t} L e^{-i(\mu_1 N_1 + \mu_2 N_2)t} e^{-iK_0 t} = e^{-i(\mu_1 - \mu_2)t} e^{iK_0 t} L e^{-iK_0 t} = e^{-ieVt} \tilde{L}(t), \quad (2.54)$$

where we introduced the bias voltage  $V = \mu_1 - \mu_2$  and we used  $\exp(N)c^\dagger = c^\dagger \exp(N+1)$  and  $\exp(N)c = c \exp(N-1)$ . Now, it is possible to rewrite Eq. (2.53)

$$I(t) = -2e \operatorname{Re} \left[ \int_{-\infty}^{\infty} dt' \Theta(t-t') e^{ieV(t-t')} \langle [\tilde{L}^\dagger(t), \tilde{L}(t')] \rangle \right]. \quad (2.55)$$

It is left to calculate the commutator, and in doing so, we will rewrite the commutator in terms of Green's functions. We observe that the commutator contains the terms

$$\begin{aligned} \langle [\tilde{L}^\dagger(t), \tilde{L}(t')] \rangle &= \sum_{pkp'k'} M_{pk}^* M_{p'k'} [\langle \tilde{c}_{1,p}(t) \tilde{c}_{1,p'}^\dagger(t') \rangle_0 \langle \tilde{c}_{2,k}(t) \tilde{c}_{2,k'}(t') \rangle_0] \\ &\quad - \langle \tilde{c}_{1,p}^\dagger(t') \tilde{c}_{1,p}(t) \rangle_0 \langle \tilde{c}_{2,k'}(t') \tilde{c}_{2,k}^\dagger(t) \rangle_0 \\ &= \sum_{pkp'k'} M_{pk}^* M_{p'k'} [G_1^>(p, p', t-t') G_2^<(k, k', t-t') \\ &\quad - G_1^<(p, p', t-t') G_2^>(k, k', t-t')], \end{aligned} \quad (2.56)$$

where we introduced and the greater  $G_{1,2}^>$  and lesser  $G_{1,2}^<$  Green's functions for both the probe and the sample. We can choose single-particle states that diagonalize the Green's function, such that  $G(p, p', t-t') = \delta_{p,p'} G(p, t')$ , where we also changed the variables  $t' = t - t'$ . Finally, we rewrite the Green's functions into the spectral representation,

$$\begin{aligned} G(p, t) &= \int_{-\infty}^{\infty} \frac{d\omega}{2\pi} e^{-i\omega t} G(p, \omega), \\ G^>(p, \omega) &= -iA(p, \omega)[1 - N_{\text{FD}}(\omega)], \\ G^<(p, \omega) &= iA(p, \omega)N_{\text{FD}}(\omega), \end{aligned} \quad (2.57)$$

and by substituting this expression we obtain for the current

$$I = e \int_{-\infty}^{\infty} d\omega \sum_{pk} |M_{pk}|^2 A_1(p, \omega - eV) A_2(k, \omega) [N_{\text{FD}}(\omega - eV) - N_{\text{FD}}(\omega)]. \quad (2.58)$$

In STM, not the current but the differential conductance  $dI/dV$  is measured. In order to simplify the calculations, it is used that the probe, system 1, consists of a normal metal. In this way, the spectral function of the probe does not depend directly on the bias-voltage and thus may be treated as a constant,

$$\sum_{pk} |M_{pk}|^2 A_1(p, \omega - eV) \approx \sum_k \sum_p |M_{pk}|^2 A_1(p) = \sum_k |T_k|^2. \quad (2.59)$$

Now, we can differentiate the current with respect to the voltage and obtain Eq. (2.47). Interestingly, one can show that the local density of states (LDOS)  $N_{\text{sample}}(x, \omega)$  is proportional to the spectral function. Here  $x$  is the tip center of curvature. Therefore, Eq. (2.47) can be rewritten in terms of the LDOS

$$\sigma(x, V) = \frac{dI}{dV} \propto \int d\omega \frac{\partial N_{\text{FD}}(\omega - eV)}{\partial \omega} N_{\text{sample}}(x, \omega), \quad (2.60)$$

which states that the LDOS of a sample can be determined when measuring the tunneling conductance.

As topological insulators are concerned, STM is mainly used as an addition to ARPES, but also has interesting features by itself. Especially the materials  $\text{Bi}_{1-x}\text{Sb}_x$  [52],  $\text{Bi}_2\text{Te}_3$  [53, 54] and  $\text{Sb}$  [55] have been investigated by using STM. The first comparison was made in  $\text{Bi}_2\text{Te}_3$ , where it was shown that the integrated density of states agrees well with the differential conductance  $dI/dV$  [54]. Additionally, STM measurements provide more information about local impurities. If there are any impurities in the sample of a topological insulator, the surface states scatter and form an interference pattern around this impurity. By Fourier transforming the pattern into  $k$ -space, one is able to find which types of scattering are suppressed, and it is possible to observe the, due to time-reversal symmetry forbidden, back-scattering between  $k$  and  $-k$  surface states.

Finally, we note that with the procedure of Hill thermodynamics, one is able to calculate the DOS, which in principle can be measured via STM. We calculate the DOS for the 2D BHZ model in Sec. 5.2.1 and 2D Kane-Mele model in Sec. 5.2.2 as inspiration for new STM experiments in the field.

### 2.2.2 Transport

Perhaps one of the most important discoveries in the field can be ascribed to the transport measurements by Molenkamp in 2007, where the quantum spin Hall effect was measured via transport. In the quantum spin Hall effect, the conductivity  $\sigma_{xy}$  is quantized, and this is exactly what is measured in a transport experiment. Transport is currently also used in 3D topological insulators, but, as the only one of the available techniques, has not been able to identify the Dirac cones yet.

In general, transport properties can be measured by applying some stimulus (perturbation) on the system and determine its response. Usually for quantum systems, this involves tuning a gate voltage in the sample, which leads to an increase of the energy in the system and triggers excitations or moving electrons in the material. Theoretically, transport properties are founded in the framework of linear response theory and is often connected to the well-known Kubo formula (which we also have seen in previous section and describes the linear response of the system to a perturbation), but can also be constructed by the Liouville equation (which describes time evolution of the phase space distribution). An instructive review to calculate transport properties for topological insulators is given in Ref. [56]

By using the experimental setup BHZ proposed, the sandwiching of HgTe between two layers of CdTe (see Fig. 2.16 in Sec. 2.1.4), König et al. measured a quantized conductivity by tuning the Fermi energy via the gate voltage into the energy gap. The famous results for the conductivity are shown in Fig. 2.21. In the figure, we see the longitudinal resistance for various thickness of the quantum well  $d$  at different gate voltages for low-temperature  $T = 0.03\text{K}$  and zero magnetic field  $B$ . The gate voltage is used to tune the Fermi energy into the energy gap, where the edge states can be measured in the topological phase  $d > 6.3\text{nm}$ . Sample I (the black line) is a narrow quantum well with  $d = 5.5\text{nm}$ , and is insulating in the gap which leads to a very high resistance (which is actually bounded to this maximum value due to the equipment of the experiment). In sample II-IV, the band gap is inverted and the system is in the topological phase. Sample II (blue) is already a bit closer to the quantum spin Hall effect,  $\sigma = 0.3e^2/h$ , but the sample is too large to actually measure the correct value (scattering effects). For smaller samples, sample III (green) and IV (red), the quantum well shows the desired current  $2e^2/h$ . The samples III and IV have the same lengths between the wells, but a different width, indicating that the current is indeed at the edge of the material and independent of the width of the material. The inset shows the results of sample III at different temperatures, where black indicates a temperature of  $T = 1.8\text{K}$ . At higher temperatures, the quantum spin Hall effect is less visible.

After this great success for transport measurements in 2D, it turned out to be more difficult

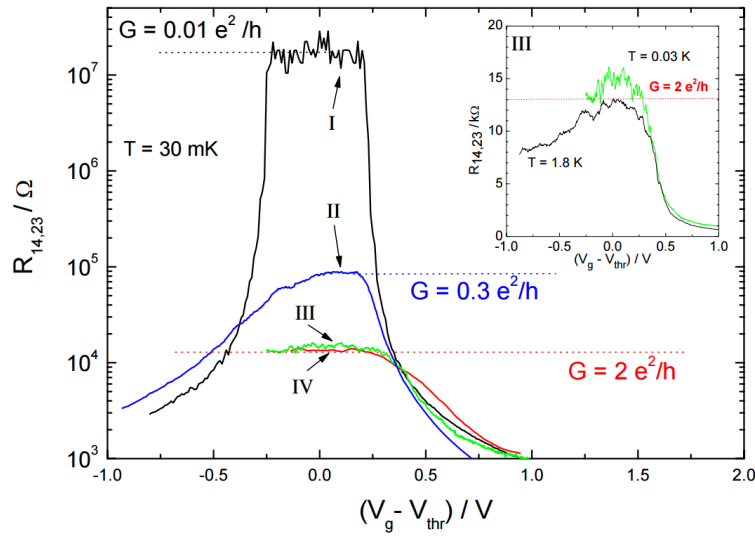


Figure 2.21: The longitudinal four-terminal resistance of the quantum well for various thickness  $d$  as a function of the gate voltage at  $T = 0.03K$  and  $B = 0T$ . Sample I is in the trivial phase and has a high resistance, whereas sample II-IV are in the topological phase and show a quantized conductivity  $e^2/h$ . The inset shows the resistance at higher temperature  $T = 1.8K$  (black line), where the effect is less visible.

to measure the quantized Hall conductance in 3D. The main issue for transport are the considered materials that have a very large static dielectric constant. In order to observe the Dirac cone, the chemical potential must be lowered via the gating voltage, but this is extremely difficult for materials with this high dielectric constant [56]. To cope with this problem, the 3D materials need to be heavily doped. Furthermore, the synthesis of these materials comes along with impurities, such as defects and vacant sites, due to which the materials are no longer perfectly crystalline [6]. However, in theory, the materials are only insulating when there is a perfect crystalline structure, which means that in experiments with these impurities there is always a finite residual bulk carrier density that is measured in transport. This bulk contribution is dominant in the measurements and it turns out to be very difficult to filter out. Although these problems also arise for ARPES, ARPES measures the surface structure, and not the resistance in the whole material and thus can more easily cope with this problem.

Due to these problems, transport has not been able to describe 3D topological insulators. Until now, the Dirac cones still have not been observed via transport measurements, but a great effort is still being done in order to find the quantized conductivity. See for example Qi and Zhang [6] and Culcer [56] for an overview of experiments.

### 2.2.3 Angle-Resolved PhotoEmission Spectroscopy (ARPES)

Probably the most influential method to observe the topological phase is by considering the single surface Dirac cone by using ARPES. Not only does this method results in beautiful pictures of Dirac cones, it also resulted in the first proof of the existence of a 3D topological insulator  $Bi_xSb_{1-x}$ . In an ARPES experiment, a photon is used to eject an electron out of a crystal and then its behavior in momentum space is analyzed. ARPES has mainly been used to study superconductors, but in the recent years it has also been applied to topological insulators. Also here, a large amount of literature is available, and we refer the interested reader further towards Ref. [57, 58].

ARPES stands for Angle-Resolved PhotoEmission Spectroscopy and is a direct method to observe the density of single particle electrons in reciprocal space. The technique is based upon the photoelectric effect, which was originally observed by Hertz in 1887 and explained by Einstein in 1905, where he described the photoelectric effect as a consequence of the quantum-behavior of light. An electron in a crystal can escape the material when it absorbs a photon. The maximum kinetic energy of the electron is  $hf - \phi$ , where  $f$  is the frequency of the photon and  $\phi$  the material work function, which indicates how much energy the valence electrons need to escape the energy barrier of a material.

Within an ARPES experiment, a beam of monochromatized radiation is send towards a crystalline-shaped sample, see also Fig. 2.22. The photons are absorbed by the electrons, and in its turn the electrons escape the sample into the vacuum in all directions. These electrons are registered by an electron energy analyzer, which is characterized by a finite-acceptance angle. In this way, the analyzer measures the kinetic energy for a given emission angle, and gives all the information about the momentum  $p$ , which are its modulo  $\sqrt{2mE_{\text{kin}}}$  and its perpendicular and parallel components. Within a non-interacting picture and by neglecting the low-energy photon momenta in the conservation laws, the kinetic energy of the electron and its momentum can be related to the crystal momentum  $\hbar k$  within the solid and the binding energy  $E_b$  of the electron

$$E_{\text{kin}} = hf - \phi - |E_b|, \quad (2.61)$$

$$p_{\parallel} = \hbar k_{\parallel} = \sqrt{2mE_{\text{kin}}} \sin(\theta), \quad (2.62)$$

where  $\theta$  is the polar emission angle (see Fig. 2.22) and  $\hbar k_{\parallel}$  is the component parallel to the electron crystal momentum such that  $k_{\parallel} = \sqrt{k_x^2 + k_y^2}$ .

We follow the same route as Ref. [58] to arrive at a theoretical understanding of ARPES. From a this point of view, an ARPES experiment is approximated via Fermi's golden rule, where the transition probability  $w_{f,i}$  between the  $N$ -electron ground state  $\psi_i^N$  and one of the

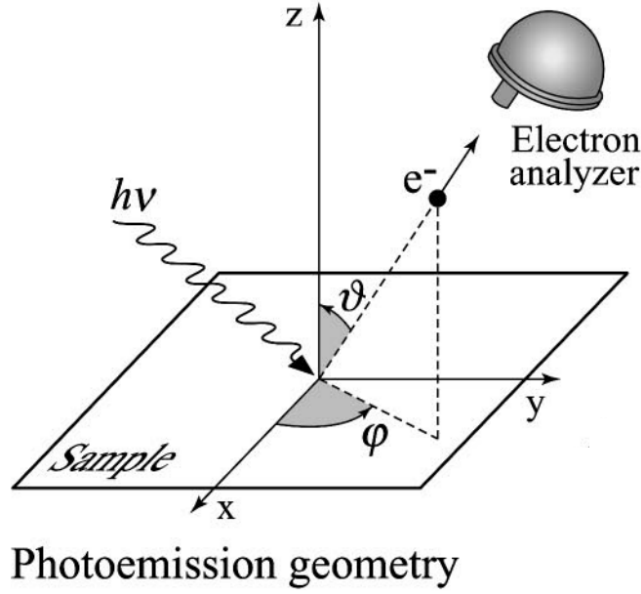


Figure 2.22: An ARPES experiment [58]. An electron is dislodged from its position in the sample due to the absorption of a photon. The electron analyzer detect the emitted electron and measures its momentum in perpendicular and parallel components.

possible final states  $\psi_f^N$  is given by

$$w_{f,i} = \frac{2\pi}{\hbar} |\langle \psi_f^N | H_{\text{int}} | \psi_i^N \rangle|^2 \delta(E_f^N - E_i^N - hf), \quad (2.63)$$

where  $E_i^N = E_i^{N-1} - E_B^k$  and  $E_f^N = E_f^{N-1} + E_{\text{kin}}$  are the initial and finite energies of the  $N$ -particle system and  $E_B^k$  is the binding energy of an electron with momentum  $k$ . The interaction with the photon is considered as a perturbation, which means

$$H_{\text{int}} = -\frac{e}{2mc} (\mathbf{A} \cdot \mathbf{p} + \mathbf{p} \cdot \mathbf{A}) = -\frac{e}{mc} \mathbf{A} \cdot \mathbf{p}, \quad (2.64)$$

with  $\mathbf{p}$  the electronic momentum operator and  $\mathbf{A}$  the electromagnetic vector potential. In deriving Eq. (2.64), the gauge of the scalar potential  $\Phi = 0$ , and we made use of the commutation relation  $[\mathbf{p}, \mathbf{A}] = -i\hbar \nabla \cdot \mathbf{A}$  and the dipole approximation ( $\mathbf{A}$  is constant in space:  $\mathbf{A}(x, t) = \mathbf{A}(t)$ ), which means  $\nabla \cdot \mathbf{A} = 0$ . The initial state of this interaction is a neutral solid, whereas the final state is a dipole due to the hole in the material that is created by the absence of the electron. When one assumes that the photoemission is instantaneous (the electron is instantaneously removed from the system and the effective potential of the system changes discontinuously at that instant), one can separate the wave-functions of the ejected electron from the electrons that remain in the system and further calculations become more simple. This assumption is called the sudden approximation, and is only applicable for escaping electrons with a high kinetic energy.

The final state can be written via this sudden approximation as  $\psi_f^N = \mathcal{A}\phi_f^k\psi_f^{N-1}$ , where  $\mathcal{A}$  is the antisymmetric operator which antisymmetrizes the entire expression according to Pauli's principle,  $\phi_f^k$  is the emitted electron and  $\psi_f^{N-1}$  is the  $(N-1)$ -electron system which is left in the material. Each possible final state can be characterized with  $\psi_m^{N-1}$  with energy  $E_m^{N-1}$ , and we need to sum over all possible states to find the total transition probability.

The initial state can also be split into an electron orbital  $\phi_i^k$  and the other particles in the system  $\psi_i^N = \mathcal{A}\phi_i^k\psi_i^{N-1}$ , where we assume that the initial state  $\psi_i^N$  is a single Slater determinant. Furthermore, the term  $\psi_i^{N-1} = c_k\psi_i^N$ , where  $c_k$  is the annihilation operator for an electron with momentum  $k$ , from which it is clear that  $\psi_i^{N-1}$  is just the wave function that remains after annihilating an electron (and is thus not an eigenstate of the initial Hamiltonian). The elements in Fermi's golden rule in Eq. (2.63) become

$$\langle \psi_f^N | H_{\text{int}} | \psi_i^N \rangle = \langle \phi_f^k | H_{\text{int}} | \phi_i^k \rangle \langle \psi_m^{N-1} | \psi_i^{N-1} \rangle, \quad (2.65)$$

in which the electron-photon interaction is given by  $\langle \phi_f^k | H_{\text{int}} | \phi_i^k \rangle = M_{f,i}^k$ , and we replaced  $\psi_f^{N-1}$  with an eigenstate  $\psi_m^{N-1}$  over which we need to sum. The total photoemission intensity is then given by summing over all transition probabilities  $I(k, E_{\text{kin}}) = \sum_{f,i} w_{f,i}$  and is proportional to

$$\sum_{f,i} |M_{f,i}|^2 \sum_m |c_{m,i}|^2 \delta(E_{\text{kin}} + E_m^{N-1} - E_i^N - hf), \quad (2.66)$$

where  $|c_{m,i}|$  is the probability to go from the initial state  $i$  into the final excited state  $m$ . For a single final state, the ARPES spectra will be given by a simple delta-function. However, for strongly correlated systems this is not the case and there will be a lot of overlapping peaks in the spectrum.

One of the main properties of ARPES is to measure this intensity of the spectrum, which can be related to the single-particle spectral function and the Green's function just as in STM. The Green's function for adding ( $G^+(k, \omega)$ ) or removing ( $G^-(k, \omega)$ ) a particle with momentum  $k$  in Fourier space reads

$$G^\pm(k, \omega) = \sum_m \frac{|\langle \psi_m^{N\pm 1} | c_{k,\sigma}^{\pm 1} | \psi_i^N \rangle|^2}{\omega - E_m^{N\pm 1} + E_i^N \pm i\eta}, \quad (2.67)$$

in which the operator  $c_{k,\sigma}^{\pm 1}$  creates an electron with momentum  $k$ , energy  $\omega$  and spin  $\sigma$  in the initial  $N$ -particle state. The summation is taking into account all possible final particle states and we added the infinitesimal  $\eta$ . In the limit  $\eta \rightarrow 0$ , we obtain the spectral functions

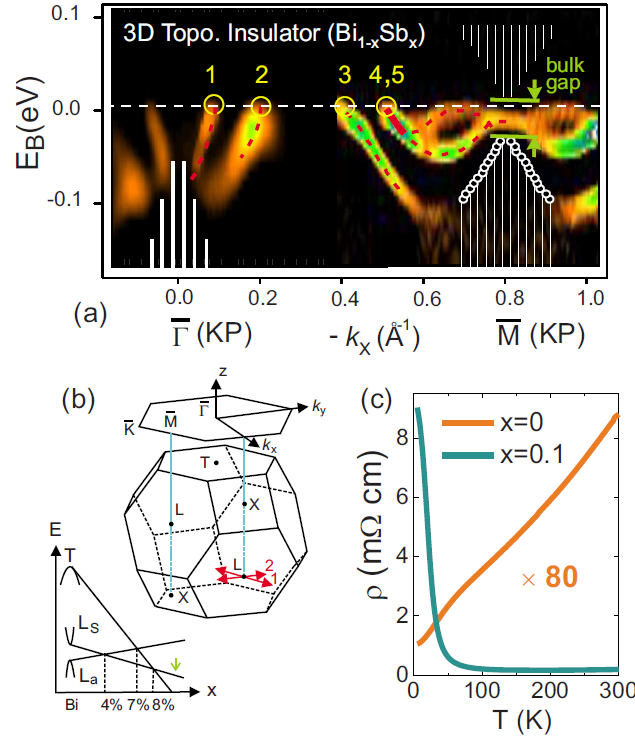


Figure 2.23: ARPES results for  $\text{Bi}_{0.9}\text{Sb}_{0.1}$ . (a) ARPES data on the (111) surface of  $\text{Bi}_{0.9}\text{Sb}_{0.1}$ . The five surface states that cross the Fermi energy are indicated with a circle and a number in the figure. The white lines indicate the filled (circle) and unfilled bulk bands. (b) A schematic drawing of the 3D Brillouin zone of the (111) projection. (c) The resistivity of pure Bi ( $x = 0$ ) and the Sb alloy ( $x = 0.1$ ). A clear drop in the resistance can be seen for the alloy. Figure taken from [5], original results in [12].

$A(k, \omega) = A^+(k, \omega) + A^-(k, \omega) = -1/\pi \text{Im} [G^+(k, \omega) - (G^-(k, \omega))^*]$ , where

$$A^\pm(k, \omega) = \sum_m |\langle \psi_m^{N\pm 1} | c_{k,\sigma}^{\pm 1} | \psi_i^N \rangle|^2 \delta(\omega - E_m^{N\pm 1} + E_i^N), \quad (2.68)$$

and these  $A^\pm(k, \omega)$  denote the one-electron removal or addition spectra functions. By using the previous formulas and the sudden approximation, one can rewrite for  $T \neq 0$  the intensity in an ARPES experiment

$$I(k, \omega) = I_0(k_{\parallel}, f, \mathbf{A}) N_{\text{FD}} A(k, \omega), \quad (2.69)$$

where  $\omega$  is the energy with respect to the Fermi level and  $I_0(k_{\parallel}, f, \mathbf{A})$  is the electron-photon intensity and is proportional to  $|M_{f,i}^k|^2$ . Moreover, the Fermi-Dirac distribution is introduced again to take into account that only occupied states can indeed attribute to the density. Therefore, in an ARPES experiment, not only the  $k$  dependence is measured, but also the intensity, which can be related to the Green's functions.

## 2.3 Conclusion

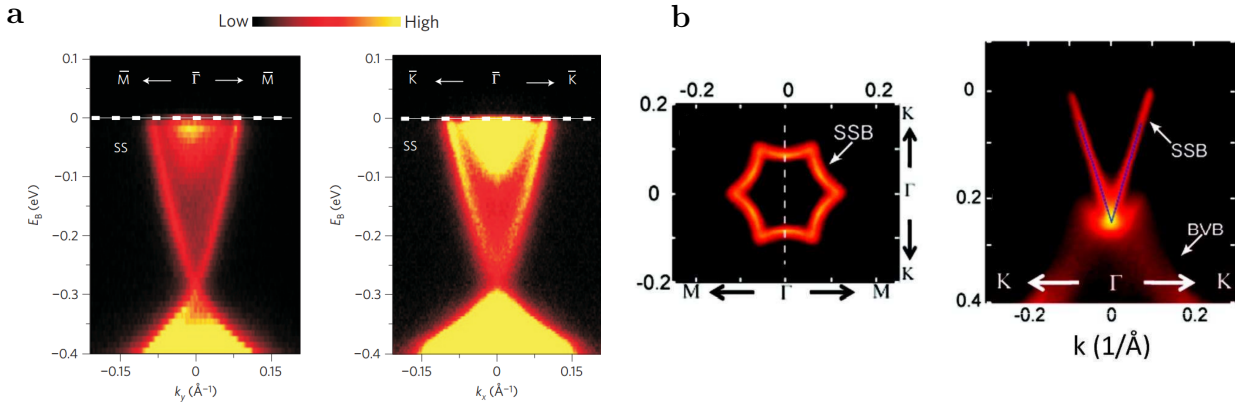


Figure 2.24: High resolution ARPES of the surface electronic band dispersion in  $\text{Bi}_2\text{Sb}_3$ . along the  $\Gamma - M$  and  $\Gamma - K$  direction. A Dirac cone is clearly visible in the spectrum. **b** The first measurements of a single Dirac cone in a topological insulator. In the left picture, the shape of the Fermi surface is depicted, whereas in the right the Dirac cone can be seen.

As mentioned, ARPES was already used quite a bit within superconductors, and is nowadays also used to measure the surface states in topological insulators. The group of Hasan in Princeton was able to verify the existence of 3D topological insulators in 2008 [12]. The main results that prove this existence are shown in Fig. 2.23. In Fig. 2.23a, we see the surface bands in the topological state indicated with a circle and a number. The bulk bands are shown in white. The figure clearly shows five surface states that cross the Fermi energy (numbers 1-5), indicating topological surface states in this material. The odd number of crossings shows the protected nature of these states [5].

After this experiment, more ARPES experiments were performed on other materials such as  $\text{Bi}_2\text{Se}_3$  [59] and  $\text{Bi}_2\text{Te}_3$  [60, 61]. Whereas the previous experimental results were relatively difficult to interpret, the results that was obtained in these measurements is very clear: a single Dirac cone at the surface state. One of the first trials is by Xia et al. [59] in 2009, and the results are shown in Fig. 2.24a. In this figure, we see a high resolution ARPES taken for two different directions for  $\text{Bi}_2\text{Sb}_3$ . The Dirac cone is clearly visible. However, from the figure it can be seen that the Fermi energy is above the conduction band, making this material actually a metal rather than an insulator. The first true topological insulator was measured by Chen et al. [60], where the material  $\text{Bi}_2\text{Te}_3$  is doped with 0.67% Sn. These results are shown in Fig. 2.24b. Also here, we see a Dirac cone, but now the material is actually an insulator in the bulk, and thus a proper topological insulator.

## 2.3 Conclusion

To summarize, we have seen in this section the relatively new research area of topological insulators and superconductors. A topological insulator is characterized by metallic edge

currents in an insulating bulk, and this phase transition is triggered by inverting the band gap. The quantum Hall effect was the first time that these edge currents appeared, leading towards the theoretical prediction of the quantum spin Hall effect in 2005, where topologically protected helical edge states appeared in the nontrivial phase. Two years later, these edge states were experimentally measured in transport experiments and this opened up the way to investigate also 3D topological insulators. These 3D topological insulators are interesting in its own way, firstly because the 2D effects can be seen, and secondly because a whole new type of strong topological insulator leading towards new effects (such as the isolated Dirac cone) have been observed in ARPES. In the meantime, the theoretical framework to classify topological insulators without interactions was developed in the tenfold way, and a topological insulator is classified according to its dimension and the protecting symmetries. Nowadays, the zero-temperature and non-interacting behavior of these materials is relatively well understood, opening the route towards new interesting effects at finite-temperatures and interaction drive topological insulators. In the next section, we focus on a procedure to describe this finite-temperature behavior by using a specific form of thermodynamics: Hill thermodynamics.

---

### 3 Hill thermodynamics: thermodynamics of finite-size systems

In the previous section Sec. 2, we have seen what topological insulators are, how the trivial phase and the topological phase can be distinguished with a topological invariant, how to classify topological phases within the tenfold way and how to detect topological phases. We have also seen that there is no sign of thermodynamics (yet) in this description of topological phases. In the thesis, we will argue that, although at first sight it might seem peculiar to use thermodynamics for finite-size systems, it is still possible to describe topological insulators within a thermodynamic framework by appropriately taking the finite-size into account. Moreover, we show universalities in the phase transitions and are able to extract finite-temperature results out of our calculations, which is exactly one of the new hot-topics in this research area. This section aims to give an introduction to the thermodynamics of finite-size systems, also called Hill thermodynamics, and to use this theory to describe the topological phase transition in the Kitaev chain in a thermodynamic way.

Thermodynamics is the part of physics which connects the heat of a system with other properties such as energy and work. Originally, thermodynamics, as a science, tried to understand and develop new engines. One of the first attempts of thermodynamics started with Otto von Guericke in 1650, who designed the first vacuum pump and who is well known for his work in the Magdeburg hemispheres. Other well-known scientists in the field of thermodynamics are Boyle, Carnot, Joule, Kelvin, Boltzmann, Gibbs, Clausius and many more: thermodynamics has always been a very important branch in physics (see also the quote on the front page, which is actually only about the second law of thermodynamics, but can be interpreted in a broader sense). In the course of years, thermodynamics developed itself from engines towards more complex systems such as colloids and superconductivity, and still is an essential part of any physics education, although nowadays perhaps better known as the slightly different subject of statistical physics. We will come back to the difference between statistical mechanics and thermodynamics in Sec. 3.2

One of the most important results of thermodynamics is to adequately describe phase transitions. A phase transition occurs when a material changes from one state of matter into another. Examples from everyday life are water turning into ice or into steam. The first theory to describe phase transitions was developed by Ehrenfest. According to his scheme, a phase transition of a system is characterized by the first discontinuous derivative of the free energy with respect to a thermodynamic variable (e.g. the pressure or chemical potential). The order of the phase transition corresponds with the number of derivatives of the free energy that are required to find this first discontinuity in the free energy. In this way, the free

energy of a first order phase transition has a discontinuity in its first derivative, whereas the free energy of a second order phase transition is continuous in the first derivative, but discontinuous in its second derivative.

Although most phase transitions can be characterized via the Ehrenfest classification, the theorem does not take into account the critical behavior of a phase transition such as the case where a derivative of the free energy diverges and, therefore, fails to describe the phase transition of e.g. ferromagnets. At the critical point, thermodynamic properties such as pressure and density are not well defined and this leads to a breakdown in the Ehrenfest classification. To avoid these ill-defined critical points, Landau developed a more general theorem which describes a phase transition in terms of the breaking of the underlying symmetries of a system. When going from water into ice for example, the system loses a part of its translational symmetry of the loosely packed fluid into a more firmly structured crystal lattice. Landau found a procedure to describe the underlying symmetry of any kind of phase transition and after him many scientists have discovered new phase transitions which were explained very accurately with this model. It is this classification that is still used in modern physics to describe phase transitions of materials.

In the course of years also new types of phase transitions were discovered, of which one of them is the topological phase transition in 2005. This discovery emerged as a black swan to oppose the view that all materials can be described with the Landau theory of symmetry breaking. It turned out that one of the interesting properties of the topological materials, the bulk boundary correspondence, can not be described by underlying symmetries. An intuitive explanation for the breakdown of the Landau theory of symmetry breaking has to do with the boundary of the system. In order to describe the underlying symmetries of a system, one needs to make use of the thermodynamic limit, the usual limit in thermodynamics in which the number of particles is taken to infinity. However, topological materials always have a boundary, making it impossible to take the thermodynamic limit because the boundary vanishes in this limit. Furthermore, topological invariant such as the Chern number are *global* parameters, whereas the Landau theory of phase transition requires a *local* order parameter. The breakdown of the normal classification makes topological materials extremely interesting and poses important questions about the validity of the classification, how the phase transition of these materials can be described and if there are also other materials (such as Weyl semimetals) where the classification scheme developed by Landau does not hold.

However, as is common in science, a well-established theory is not rejected this easily. Thermodynamics is so well-established in the description of materials and phase transitions that there might be something interesting to investigate here. The only difference between ordinary materials and topological materials is the boundary. But, luckily, the before

mentioned Hill thermodynamics can be used to adequately describe the boundary of systems by considering finite system sizes. Moreover, Quelle et al. [8] proved that actually model topological materials with this Hill thermodynamics and find their phase transitions, which means that thermodynamics might still be an at first sight unexpected way to go when describing topological materials.

This section describes the method of Quelle et al. [8] to use thermodynamics for identifying phase transitions in topological materials. We will show the procedure in detail for the Kitaev chain in this section. First, we review the theory of phase transitions in Sec. 3.1. Second, we introduce Hill thermodynamics and show how Hill thermodynamics can be used to find phase transitions in Sec. 3.2, and third, we show the thermodynamic description of phase transitions for the Kitaev chain in Sec. 3.3. In Sec. 4, we will use the general procedure developed in this section to describe the topological phase transitions for multiple topological models such as the SSH (1D topological insulator), BHZ(2D topological insulator) and tight binding graphene (2D topological insulator).

## 3.1 Theories of phase transitions

In the course of years, there have been two dominant theories to classify phase transitions: the Ehrenfest classification and the Landau theory of symmetry breaking. In this section, we review these two theories and describe how the procedures were developed and when they can be used. Furthermore, we will discuss new types of phase transitions, the quantum phase transition and topological phase transitions, and show how these phase transitions fit in the current framework.

### 3.1.1 Ehrenfest classification

The Ehrenfest classification was developed by Paul Ehrenfest in 1933 as a framework to classify phase transitions. In those days, all known phase transitions were associated with a latent heat difference between two phases of matter. This view changed with experiments in Leiden, starting with the liquefaction of helium by Kamerlingh Onnes in 1908, for which he gained the Nobel Prize [62]. In the 1920's, Dana and Onnes observed a sharp maximum in the pressure-temperature curve in liquid helium at 2.2 K [63]. This result inspired Wolfke and Keesom to measure the dielectric constant of liquid helium near this temperature, which resulted in a "rapid change of the galvanometer" near this point, indicating a phase transition in liquid helium [64]. The two phases were originally called liquid helium I and liquid helium II [65]. The group of Keesom continued to study the phase transition of liquid helium and found the interesting result that this type of phase transition did not have an associated latent heat and also had no clear surface demarcation between phases [66, 67]. In fact, the heat capacity of liquid helium would rise to a finite maximum value before, and then jump to

a much lower value. Keesom and Clusius denoted this as a  $\lambda$  phase transition - a name suggested by Ehrenfest -, due to the  $\lambda$ -shaped curve of the latent heat, as is shown in Fig. 3.1.

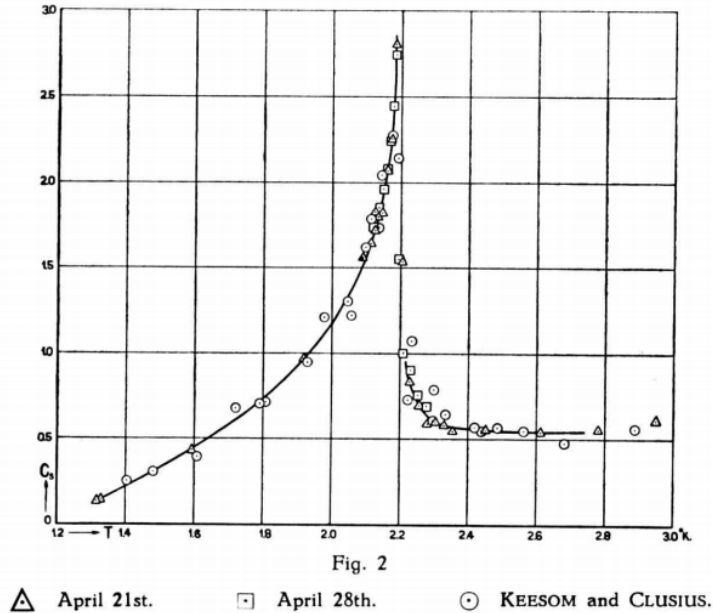


Figure 3.1: The  $\lambda$  phase transition for liquid helium as was found out by Keesom and Clusius [66]. The heat capacity (y-axis) first rises as a function of the temperature (x-axis), and then suddenly jumps towards a lower value at  $T = 2.2K$ , the point of the phase transition. A  $\lambda$ -shaped curve indicates the name of this type of phase transitions.

A year later, Ehrenfest developed a mathematical description to accommodate the difference between the liquid helium phase transition and previously observed phase transitions. The differences according to the Ehrenfest classification are shown in Fig. 3.2. He considers surfaces of constant Gibbs free energy which have continuous derivatives away from the transition points. The Gibbs free energy is given by  $G = U + pV - TS$ , where  $U$  is the internal energy,  $p$  the pressure,  $V$  the volume,  $T$  the temperature, and  $S$  the entropy. These constant  $G$  surfaces appear as curves in the  $p$ - $T$  plane. Now, a first-order phase transition is characterized by a kink in the  $G$  surface, which means that the first derivative of  $G$  with respect to a thermodynamic variable is discontinuous. A second-order phase transition is characterized by a kink in the in the first derivative of  $G$  with respect to a thermodynamic variable and a discontinuity in the second derivative. A second order phase transition therefore has a jump, or discontinuity, in the heat capacity at constant volume  $C_v = -T(\partial^2 G)/(\partial T^2)$  and explains the phase transition of liquid helium. In this way, it is even possible to obtain higher order phase transitions.

Immediately after the publication, the Ehrenfest classification got a lot of attention and was

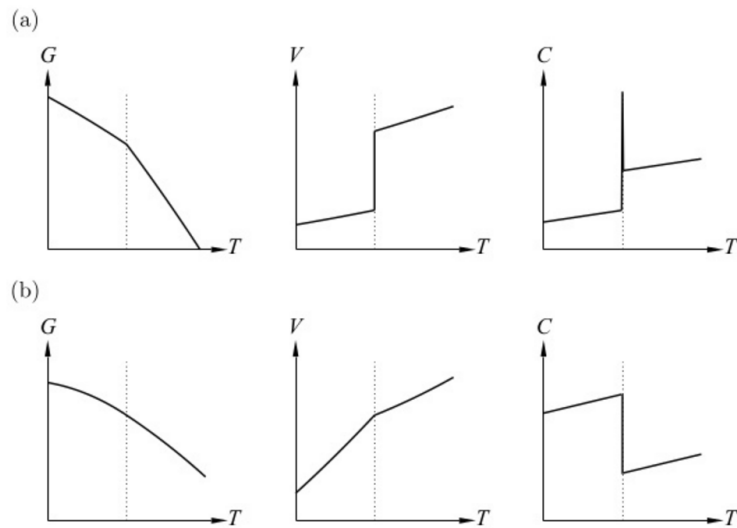


Figure 3.2: Ehrenfest's classification of phase transitions. (a) First-order phase transition. The Gibbs free energy shows a kink, which means the volume, the first derivative with respect to the pressure, shows a discontinuity. (b) Second-order phase transition. Now the volume shows a kink, meaning the heat capacity shows a discontinuity. Image retrieved from [68]

widely discussed in the scientific community [67]. Although not everyone agreed initially, new evidence of these second-order phase transitions were found, building up a solid theorem to describe phase transitions. However, a couple of years after the publication, doubts began to rise whether the most well-known example of a second-order phase transition, the liquid helium  $\lambda$  phase transition, actually satisfied the Ehrenfest definition of a second-order phase transition.

Moreover, the situation changed in 1944 when Lars Onsager solved the two-dimensional Ising model in the absence of a magnetic field exactly, showing a phase transition where the free energy derivative becomes *infinite* rather than *discontinuous*: something which did not fit within the Ehrenfest scheme. This result was the first to point out a flaw in the Ehrenfest classification. Later, also the  $\lambda$  phase transition was commonly thought to have an infinite heat capacity at the phase transition rather than having a finite jump, making the Ehrenfest classification inadequate to describe this type of phase transitions.

Although the Ehrenfest classification is generally thought to be too simple, it still gives important information about the type of phase transition and is frequently used in physics textbooks to introduce students to the different types of phase transitions: phase transitions that do involve latent heat (first-order or discontinuous phase transitions) and phase transitions that do not involve latent heat (higher-order or continuous phase transitions). However, when one needs to classify also models with infinite derivatives of the energy such as the Ising model or liquid helium, one needs to use a different classification scheme developed

by Landau. This will be discussed next.

### 3.1.2 Landau theory of symmetry breaking

The first alternative of the Ehrenfest classification was developed by Landau and Lifshitz in their classic work *Statistical Physics* in 1938 [1]. Although their classification had less influence on the debate on the classification of phase transitions, the procedure is considerably better than the Ehrenfest's classification because it can work with the ill-defined second-order phase transitions such as the two-dimensional Ising model [67]. The Landau classification, as we will briefly denote the Landau-Lifshitz, or Ginzburg-Landau, classification scheme, is a phenomenological approach to classify phase transitions based on the symmetries of a system and involves the notion of symmetry breaking. In order to get a feeling for the approach, we follow the same route as [30] and start by describing the classification of the  $D$ -dimensional Ising model as an example of how the Landau classification can be used. Within this example, the main idea of symmetry breaking, the concept of an order parameter and the Landau free energy are all introduced.

To appreciate the Landau classification scheme, it is best to consider a simple model that exhibits a second-order phase transition at nonzero temperature: the Ising model in  $D$ -dimensions, where  $D$  is more than one. The model describes the competition of spin direction  $\hat{S}_{z,i}$  at lattice sites  $x_i$  that can have values  $m_i = \pm\hbar/2$  and is considered to be one of the easiest models of magnetism. The spins on each site are coupled to their neighboring sites with strength  $J$ . The Hamiltonian of such a system is given by

$$\hat{H} = -\frac{2J}{\hbar^2} \sum_{\langle i,j \rangle} \hat{S}_{z,i} \cdot \hat{S}_{z,j}, \quad (3.1)$$

where  $\langle i,j \rangle$  denotes the summation over nearest-neighbors. For  $J > 0$  the system lowers its energy to point all spins in the same direction, the system is said to be ferromagnetic. In contrast, when  $J < 0$ , the spins tend to point in opposite direction, making the interaction antiferromagnetic. Now, it is common to introduce the magnetization, the expectation value of the average spin,

$$\langle M \rangle = \frac{1}{N} \left\langle \sum_i \hat{S}_{z,i} \right\rangle = \frac{1}{Z} \text{Tr} \left[ \left( \frac{1}{N} \sum_i \hat{S}_{z,i} \right) e^{-\beta \hat{H}} \right], \quad (3.2)$$

with  $Z$  the canonical partition function,  $N$  the total number of spins and where the trace is over all microstates of the model. The Ising model can exactly be solved for the one-dimensional and the two-dimensional case, but in more than three dimensions we need to resort to approximation methods.

We start rewriting the Hamiltonian with a fluctuation expansion of the spin around a certain fixed magnetization  $M$

$$\hat{S}_{z,i} = M + \hat{S}'_{z,i}, \quad (3.3)$$

where we assume the fluctuations  $\hat{S}'_{z,i}$  are small such that we only need to take the linear order into account. We can expand the Hamiltonian

$$\hat{H} = -\frac{2J}{\hbar^2} \sum_{\langle i,j \rangle} \hat{S}_{z,i} \cdot \hat{S}_{z,j} = -\frac{2J}{\hbar^2} \sum_{\langle i,j \rangle} (M + \hat{S}'_{z,i}) \cdot (M + \hat{S}'_{z,j}) \quad (3.4)$$

$$= -\frac{2J}{\hbar^2} z N M^2 - \frac{4J}{\hbar^2} z M \sum_i \hat{S}'_{z,i} + \mathcal{O}((\hat{S}'_{z,i})^2), \quad (3.5)$$

with  $z = 2D$  is the number of nearest neighbors in  $D$  dimensions. We can now substitute Eq. (3.3) back into Eq. (3.4) and, by neglecting higher order terms  $\hat{S}'_{z,i}$ , find the Hamiltonian in terms of  $\hat{S}_{z,i}$

$$\hat{H} \approx \frac{2J}{\hbar^2} z N M^2 - \frac{4J}{\hbar^2} z M \sum_i \hat{S}_{z,i}. \quad (3.6)$$

From this expression, we are able to approximate the partition function of the model in terms of the average magnetization

$$Z(M) = \sum_{\{m_i\}} \left\langle \{m_i\} \left| \exp \left\{ -\frac{\hat{H}}{k_B T} \right\} \right| \{m_i\} \right\rangle \quad (3.7)$$

$$\approx \sum_{\{m_i\}} \left\langle \{m_i\} \left| \exp \left\{ \frac{2zJNM^2}{k_B T \hbar^2} + \frac{4zJM}{k_B T \hbar^2} \sum_i \hat{S}_{z,i} \right\} \right| \{m_i\} \right\rangle \quad (3.8)$$

$$= \exp \left\{ \frac{-2zJNM^2}{k_B T \hbar^2} \right\} \prod_i \sum_{m_i = \pm \hbar/2} \exp \left\{ \frac{4zJM m_i}{k_B T \hbar^2} \right\} \quad (3.9)$$

$$= \exp \left\{ \frac{-2zJNM^2}{k_B T \hbar^2} + N \log \left( \exp \left\{ \frac{2zJM}{k_B T \hbar} \right\} + \exp \left\{ \frac{-2zJM}{k_B T \hbar} \right\} \right) \right\} \quad (3.10)$$

$$= \exp \left\{ -\frac{F_L(M)}{k_B T} \right\}, \quad (3.11)$$

where in the last line we introduced the Landau free energy

$$F_L(M) = \frac{2zJNM^2}{\hbar^2} - N k_B T \log \left( \exp \left\{ \frac{2zJM}{k_B T \hbar} \right\} + \exp \left\{ \frac{-2zJM}{k_B T \hbar} \right\} \right). \quad (3.12)$$

In order to obtain the average value of the magnetization, we can expand the free energy in terms of power  $M$

$$F_L(M) = -N k_B T \log(2) + \frac{1}{\hbar^2} \left( 2zJNM^2 - \frac{2Nz^2J^2}{k_B T} \right) M^2 + \frac{1}{\hbar^4} \frac{4Nz^4J^4}{3(k_B T)^3} M^4 + \dots \quad (3.13)$$

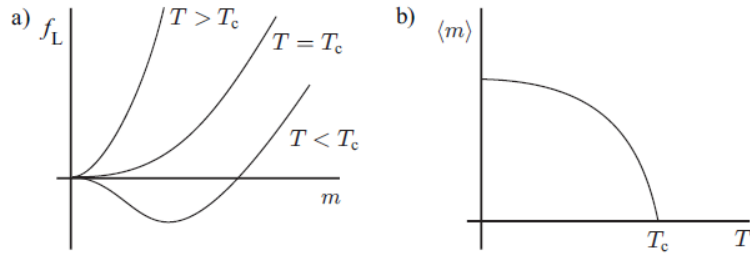


Figure 3.3: Qualitative sketch of a) the Landau free energy as a function of  $m$  for  $T < T_c$  and  $T > T_c$  and b) the order parameter for a continuous phase transition. A phase transition between the ordered and disordered phase occurs for  $T = T_c = Jz/k_B$ . Image retrieved from [30]

The first term in this expression is independent of  $M$  and is the entropy contribution to the free energy at zero magnetization. The second term is quadratic in  $M$  and the third term is quartic in  $M$ . By denoting the coefficient in front of the second term as  $\alpha(T)$  and the coefficient in front of the third term by  $\beta(T)$ , we can examine the behavior of the free energy. When both  $\alpha(T)$  and  $\beta(T)$  are positive, we have a global minimum in the free energy at  $\langle M \rangle = 0$ , which is also called the disordered phase because the spins are not aligned. The coefficient  $\alpha$  can also become negative at low temperatures, making the free energy at  $M = 0$  a maximum and the minimum at a nonzero value of  $M$ . This transition from positive to negative  $\alpha(T)$  is also called a continuous phase transition, because a phase change from a disordered system to an ordered system has occurred in a continuous way, which is the same as the second order phase transition from Ehrenfest. This phase change occurs at the critical temperature  $T_c = Jz/k_B$ . The expectation value of the magnetization is given by minimizing the free energy

$$\left. \frac{dF_L(M)}{dM} \right|_{M=\langle M \rangle} = 0, \quad \langle M \rangle = \frac{\hbar}{2} \tanh \left( \frac{2zJ \langle M \rangle}{k_B T \hbar} \right), \quad (3.14)$$

which needs to be solved numerically.

In this example, we encountered the order parameter  $M$  in which we could expand the free energy. This is the main idea of the Landau-Ginzburg classification. In principle, any free energy can be expanded in series of an order parameter, which discriminates the different phases of the phase transition (the disordered from the ordered phase). This means the free energy of a system with volume  $V$  is given by

$$F_L(m) = V f_L(m) = \frac{V}{2} \left\{ \alpha(T) m^2 + \frac{\beta(T)}{2} m^4 + \frac{\delta(T)}{3} m^6 + \dots \right\}, \quad (3.15)$$

where  $f_L(m)$  is the Landau free energy density and  $m$  is the order parameter of the system. Due to spin reversal symmetry, only even powers occur in this expansion. Depending on the

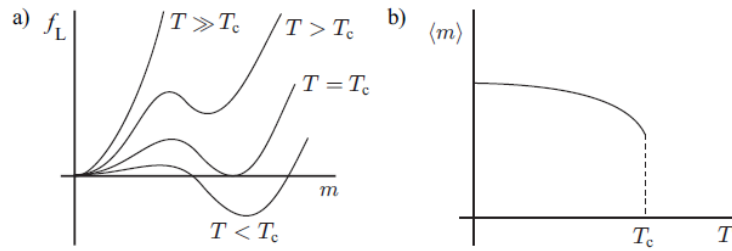


Figure 3.4: Qualitative sketch of a) the Landau free energy as a function of  $m$  for  $T < T_c$  and  $T > T_c$  and b) the order parameter for a discontinuous phase transition. A phase transition between the ordered and disordered phase occurs for  $T = T_c = Jz/k_B$ . Image retrieved from [30]

sign of  $\beta(T)$ , the transition between the phases is continuous (positive  $\beta(T)$ , see Fig. 3.3) or discontinuous (negative  $\beta(T)$ , see Fig. 3.4).

In the continuous phase transition, the free energy either has one global minimum for zero (disordered) or nonzero (ordered)  $m$ . When  $\alpha(T)$  changes sign, the order parameter shifts continuously from  $m = 0$  to  $m \neq 0$  and vice versa.

In the discontinuous phase transition, the free energy has more minima for temperatures near  $T_c$ . At the phase transition, the free energy has two minima for two different values of the order parameter. When the temperature is lowered from  $T > T_c$  to  $T < T_c$ , a discontinuous phase change occurs where the value of  $m$  jumps from zero to a nonzero value. This is depicted in Fig. 3.4b.

To summarize, the Landau-Ginzburg classification uses an order parameter to expand the free energy in series of this order parameter. By analyzing its behavior in terms of the coefficients in front of the order parameter, it is possible to classify whether a phase transition is continuous or discontinuous, in the same sense as Ehrenfest's classification, but now from a phenomenological perspective. In experiments, only first and second order phase transition seem to occur, which increased the scientific focus on the difference between a continuous and discontinuous phase transition, leaving the differences between higher-order phase transitions relatively untouched.

### 3.1.3 Quantum and topological phase transitions

In the previous sections, we saw the different types of classification schemes for phase transitions at finite temperature. The phase transitions were driven by a change in the temperature and could be distinguished in either a continuous or a discontinuous phase transition. In the course of year after the introduction of the classification schemes, more strange phase were encountered, including phase transitions *at* zero temperature. These

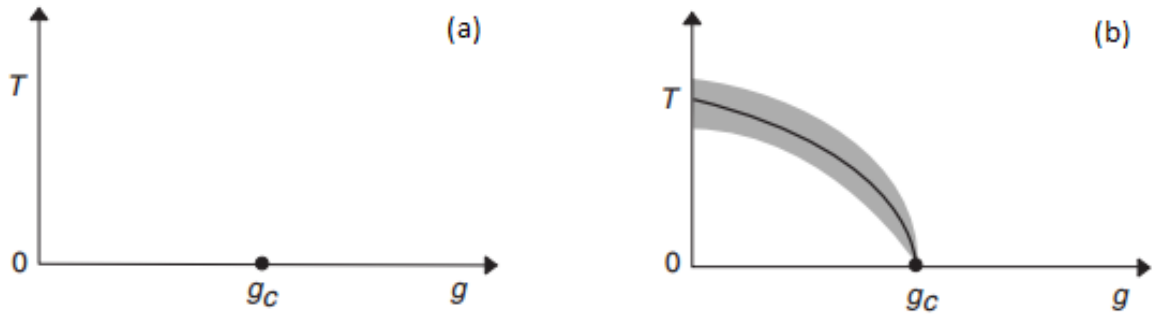


Figure 3.5: Two phase diagrams of a quantum phase transition. In both figures, the quantum critical point is given by  $g_c$  at  $T = 0$ . In (a), the quantum phase transition only occurs at  $T = 0$ , whereas in (b) there is an additional line of  $T > 0$  second-order phase transitions. The Ehrenfest classification of phase transitions are valid in the shaded region in (b) [69].

so-called quantum phase transitions occur at zero temperature and therefore cannot be driven by the usual thermal fluctuations, but by quantum fluctuations ( $\hbar\omega > k_B T$ ) driven by the Heisenberg uncertainty principle. The system has a degenerate ground state, and can switch phases by tuning a physical parameter such as doping, magnetization or chemical potential (but not the temperature).

One can get an intuitive picture of a quantum phase transition by considering a Hamiltonian  $H(g)$  in a finite lattice which varies as a function of the dimensionless coupling  $g$  [69]. An interesting case occurs when  $g$  couples to a conserved quantity such that  $H(g) = H_0 + gH_1$ , where  $H_0$  and  $H_1$  commute. The energy of the system can be calculated by diagonalizing  $H_0$  and  $H_1$  independently. Now, the energy spectrum depends on  $g$ , such that at  $g = g_c$  there is a level crossing  $H_0 = gH_1$ , where an excited energy level becomes a ground state energy in a non-analytic way. This is the main idea of a quantum phase transition, by tuning the parameter  $g$ , a phase change from, in this example, the excited state to the ground state occurs. The critical value  $g_c$  is referred to as the quantum critical point. For an infinite lattice, the avoided crossing is sharper than for a finite lattice, making the possibilities even richer for larger system sizes.

Strictly speaking, quantum phase transitions only occur at zero temperature. However, it is impossible to actually measure materials at zero temperature, and therefore we are interested what happens at small finite temperatures. In general there are two important phase diagrams near a quantum critical point, both depicted in Fig. 3.5. The first type, Fig. 3.5a, only has a thermodynamic singularity at  $g_c$  and zero temperature, whereas all other (thermodynamic)  $T > 0$  properties are analytic functions. The second type, Fig. 3.5b, contains a  $T > 0$  line, indicating a second-order phase transition, that is terminated in  $g_c$ . In the

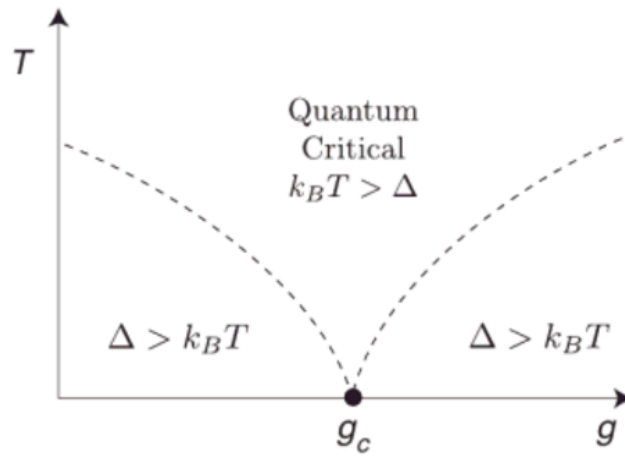


Figure 3.6: The quantum critical phase. In this figure,  $\Delta = \hbar\omega$  indicates the energy scale of the quantum fluctuations and  $k_B T$  the scale of the thermal fluctuations. When  $\Delta > k_B T$ , the quantum fluctuations dominate. In the quantum critical phase, the energy scales compete  $\Delta < k_B T$  [69].

shaded area, the theory of classical phase transitions driven by thermal fluctuations, the Ehrenfest classification, can be applied.

Often associated with quantum phase transitions is the quantum critical region: the region where the quantum and thermal fluctuations are equally important [69]. The typical energy scales for the quantum fluctuations  $\hbar\omega$  compete with the thermal fluctuations  $k_B T$  and this leads to interesting and often surprising physics. The quantum critical region is depicted in Fig. 3.6. Note that these lines do not indicate a quantum phase transition, but a smooth crossover between two regions in which quantum and/or thermal fluctuations are important.

The difference between a topological phase transition and a quantum phase transition is the following: in a quantum phase transition, just as in a normal phase transition, a symmetry is broken, whereas in a topological phase transition this is not the case. As we have already seen in Sec. 2.1.2 and Sec. 2.1.3, topological phase transitions do not break any global symmetries, and are rather defined by a topological invariant that is either present or not present. As Hasan and Kane state:

*The state responsible for the quantum Hall effect does not break any symmetries, but it defines a topological phase in the sense that certain fundamental properties (such as the quantized value of the Hall conductance and the number of gapless boundary modes) are insensitive to smooth changes in material parameters and cannot change unless the system passes through a quantum phase transition [5].*

Therefore topological phase transitions do not involve symmetry breaking, but are defined by “non-smooth deformations” that involve closing the gap [70]. Although this difference,

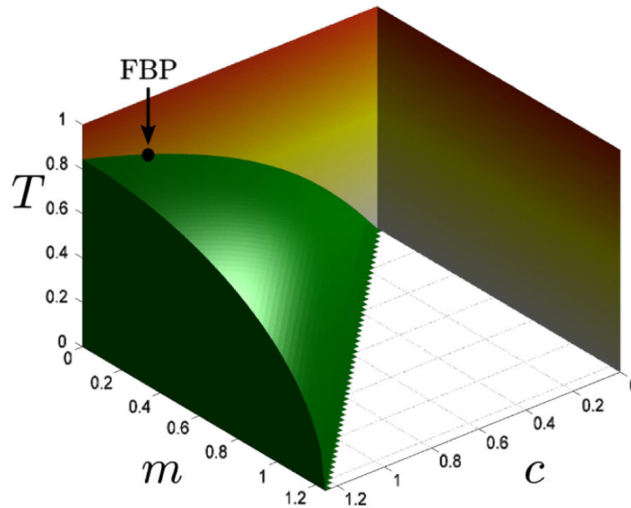


Figure 3.7: Finite-temperature topological phase diagram as calculated via the Uhlmann phase. In this figure,  $m = 2\mu$ ,  $c = t$  and  $\Delta = 1$ . The FBP (flat-band point) indicates the point in which the Kitaev chain of infinite length has a flat band in the spectrum.

topological phase transitions are often considered to be a special type of a quantum phase transition and are believed to follow the same low temperature phase diagram as depicted in Fig. 3.5.

Only two years ago, the first finite-temperature phase diagram for different topological models was obtained by Viyuela et al. [71, 72]. As discussed in Sec. 2.1.3, the difference between the topological and trivial phase at zero temperature can be identified with a Chern number via the Berry curvature. This procedure only works at zero temperature because the Berry phase is calculated via pure quantum states. At finite temperatures, mixed quantum states come into play and therefore this procedure breaks down, although a slightly different procedure that involves the Uhlmann phase can be used. The Uhlmann phase makes use of mixed quantum states, and Viyuela et al. worked out a procedure to define a winding/Chern number even at nonzero temperature. We will discuss the details of this procedure in more depth in Sec. 5, where we compare our finite-temperature results for the Kitaev chain with the ones obtained via the Uhlmann phase. As a teaser, the finite-temperature topological phase diagram for the Kitaev chain is depicted in Fig. 3.7.

Now, we have all the ingredients. We introduced the different types of classification schemes and discussed the different types of phase transitions and indicated where the topological phase transitions fits in. It is time to start with a new old way to describe these topological phase transitions. New in the sense that the method has not been used before Quelle et al. [8] and old because the technique has already been available since 1963.

## 3.2 Hill thermodynamics

In order to investigate the topological phase transition, we need to work with the boundaries of the system within the framework of thermodynamics. Normally, in statistical physics, these systems with boundaries often lead to tedious calculations, because one needs to imply boundary conditions, but at least these calculations can be performed. This is because statistical physics is about the *microscopic* description of a system from which we can calculate macroscopic properties. However, thermodynamics analyzes the *macroscopic* behavior of a macroscopic system and derives thermodynamic functions and mathematical interrelations between these functions. This indirectly means that the finite-size effects are generally not taken into account in thermodynamics, which is also due to the thermodynamic limit  $N \rightarrow \infty$ . Almost 60 years ago, the chemist Terrell Hill recognized this problem and developed a new thermodynamic framework which makes use of thermodynamics to describe systems with a boundary. In this section, we describe Hill's framework and show how it can be used to properly calculate thermodynamic variables for finite-size systems.

Hill conveniently makes use of the extensive and intensive variables that thermodynamics has to offer. An intensive variable is independent of the system size or the amount of material in the system. Examples are the pressure, temperature and density. In contrary, extensive variables scale *linearly* with the system size. Examples are the volume, mass and energy of a system. According to Hill, we will see that when considering a boundary in the system, extensive quantities such as the energy need not necessarily scale linearly with the system size. Instead, Hill introduces an additional subdivision potential, which in principle can be anything, that needs to be added to the appropriate thermodynamic energy of the system

Hill starts his analysis of small systems by considering an ensemble of  $\mathcal{N}$  distinguishable, independent subsystems, all characterized by the volume  $V$ , temperature  $T$  and chemical potential  $\mu$ . In the conventional thermodynamic limit of  $\mathcal{N} \rightarrow \infty$ , the whole ensemble is a macroscopic thermodynamic system, although each individual subsystem is not. The total energy of the system, besides the usual terms, also depends on  $\mathcal{N}$ , and therefore one can write for the internal energy

$$dE_t = TdS_t - p\mathcal{N}dV + \mu dN_t + Xd\mathcal{N}, \quad (3.16)$$

where  $p$  is the mean pressure,  $S$  is the entropy,  $N$  is the number of particles within the system and the sub-index  $t$  denotes properties of the whole ensemble. He also introduced the term  $X = -\hat{p}V$ , which can be regarded as another  $pV$  work term that adds to the internal energy. Indeed,  $Xd\mathcal{N}$  corresponds to changing the volume of the system by increasing the number of subsystems with volume  $V$ , rather than changing  $V$  per subsystem. By integrating Eq. (3.16)

in the grand canonical ensemble (keeping  $\mu, V$  and  $T$  constant), one finds

$$E_t = TS_t + \mu N_t - \hat{p}V\mathcal{N}, \quad (3.17)$$

and one identifies  $X = -\hat{p}V = (E_t - TS_t - \mu N_t)/\mathcal{N}$ . The next step is an important one, as it characterizes the essential mechanism of Hill thermodynamics. We define  $\bar{E} = E_t/\mathcal{N}$  and  $\bar{N} = N_t/\mathcal{N}$  as the appropriate thermodynamic ensemble averages of  $E$  and  $N$  per subsystem and  $S = S_t/\mathcal{N}$  as the appropriate  $S$  per subsystem. Notice that we did not put a bar over  $S$  because it is a property of the complete probability distribution and not an average value in the same sense as  $\bar{N}$  and  $\bar{E}$ . By using these definitions, we can rewrite Eq. (3.16)

$$\begin{aligned} d(\mathcal{N}\bar{E}) &= Td(\mathcal{N}S) - p\mathcal{N}dV + \mu d(\mathcal{N}\bar{N}) + Xd\mathcal{N} \\ \mathcal{N}d\bar{E} + \bar{E}d\mathcal{N} &= T(\mathcal{N}dS + Sd\mathcal{N}) - p\mathcal{N}dV + \mu(\mathcal{N}d\bar{N} + \bar{N}d\mathcal{N}) + Xd\mathcal{N} \\ d\bar{E} &= TdS - pdV + \mu d\bar{N}, \end{aligned} \quad (3.18)$$

where in the last line we substituted  $X = \bar{E} - TS - \mu\bar{N}$  and we divided by  $\mathcal{N}$  to obtain the differential equation for a single subsystem. Notice that the thermodynamic identity for a subsystem is still given by the usual thermodynamic expression. However, when comparing Eq. (3.18) with Eq. (3.17), we observe that upon integrating the expression in the grand canonical ensemble, the internal energy per system is

$$\bar{E} = TS + \mu\bar{N} - \hat{p}V = TS - pV + \mu\bar{N} + \mathcal{E}, \quad (3.19)$$

where  $\mathcal{E} := (p - \hat{p})V$  defines the subdivision potential, which states that the internal energy is *not* a linear homogeneous function of  $S, V$  and  $\bar{N}$ . Eq. (3.19) is the main result of Hill's analysis and captures the full non-extensive behavior of a finite-size subsystem in the grand-canonical ensemble. For a macroscopic system, the mean pressure and the integral pressure are equal  $\hat{p} = p$ , but this does not hold in general for a finite-size system, where doubling the volume  $V$  will not double the internal energy because of the finite size and edge effects. As a result, the subdivision potential vanishes in the thermodynamic limit and we obtain the usual expressions for the macroscopic system.

### 3.2.1 Gibbs thermodynamics

We should note that, although the procedure looks trivial, it differs in an important way from the conventional approach developed by Gibbs when considering boundaries in a system. In Gibbs' procedure, one can split the contribution from the bulk ( $B$ ) and the boundary ( $b$ ), such that the internal energy of the bulk is

$$dE_B = dS_B T_B - pdV + \mu_B dN_B, \quad (3.20)$$

and the energy for the boundary is

$$dE_b = dS_b T_b - \gamma dA + \mu_b dN_b, \quad (3.21)$$

where  $\gamma dA$  is the analogue of work ( $pdV$ ) of a 2D material. In equilibrium,  $T_B = T_b = T$ ,  $\mu_B = \mu_b = \mu$ , and the total energy of the system reads

$$dE_{B+b} = dE_B + dE_b = Td(S_B + S_b) - pdV - \gamma dA + \mu d(N_B + N_b), \quad (3.22)$$

where we encounter an additional  $-\gamma dA$  term in the thermodynamic identity. This is a crucial difference when comparing Gibbs' and Hill's approaches. Whereas Gibbs assumes that the boundary contributes in the above way, Hill connects the boundary to the bulk in a natural way and finds that the subdivision potential *might* correspond to  $\gamma A$  and additional terms. Therefore, Gibbs' procedure works perfectly well when the bulk and the boundary can be considered independent, or when an effective theory can be written down for both parts. However, this theory is not useful when considering a system with a boundary phase transition, in which the boundary merges with the bulk, as it is the case for topological phase transitions.

### 3.3 Thermodynamics and statistical physics

In this section, the correspondence between the statistical physics and thermodynamics will be made in order to investigate whether thermodynamic signatures can indicate the topological phase transition in the Kitaev chain in Sec. 3.4. As usual for quantum phase transitions, we will describe the phase transition according to the Ehrenfest classification.

In Ref. [8], it was shown that we can use Hill's formalism to describe topological models, and that the subdivision potential provides a thermodynamic description of the edge states. To connect Hill thermodynamics to topological models, one considers a system of finite size  $V$  in contact with an environment characterized by  $T$  and  $\mu$ . The grand potential is

$$\Phi = \bar{E} - TS - \mu \bar{N} = \Phi_c + \Phi_0, \quad (3.23)$$

with  $\Phi_c = -pV$  and  $\Phi_0 = \mathcal{E}$  the subdivision potential. One of the strengths of Hill's approach is that the thermodynamic identities are kept the same as in conventional thermodynamics. The grand potential of this system in the framework of statistical mechanics reads

$$\Phi(T, \mu, V) = -k_B T \log[Z], \quad (3.24)$$

where  $k_B$  is Boltzmann's constant,  $T$  the temperature and  $Z = \sum_n e^{-\beta[E_n - \mu N]}$  the grand

partition function with energy  $E$  of state  $n$  of the system. To obtain the grand potential of the infinite Kitaev chain it is possible to calculate the outcome of this equation with the values that were found for the energies in the previous section. For a finite Kitaev chain, the Hamiltonian of the Kitaev chain from Eq. (2.21) needs to be diagonalized to find the corresponding energies. For a general diagonalized Hamiltonian, we will find

$$H = \sum_i [\epsilon_i a_i^\dagger a_i - \epsilon_i a_i a_i^\dagger] - \mu N/2 = \sum_i [2\epsilon_i a_i^\dagger a_i - \epsilon_i] - \mu N/2. \quad (3.25)$$

Now this factor  $\mu N/2$  is a constant which can be shifted out of the partition function. We obtain

$$\begin{aligned} Z = \text{Tr}(e^{-\beta H}) &= \sum_{\psi_i} \left\langle \psi_i \left| e^{-\beta \sum_i [-\epsilon_i + 2\epsilon_i a_i^\dagger a_i]} \right| \psi_i \right\rangle \\ &= e^{\beta \sum_i \epsilon_i} \sum_{\psi_i} \left\langle \psi_i \left| e^{-\beta \sum_i [2\epsilon_i a_i^\dagger a_i]} \right| \psi_i \right\rangle \\ &= \prod_i [e^{\beta \epsilon_i}] \prod_i [1 + e^{-2\beta \epsilon_i}], \end{aligned}$$

where  $\psi_i$  are the fermionic wave functions, which either result in a 0 or a 1 when acted on with the creation and annihilation operators and  $\beta = \frac{1}{k_B T}$ . By using Eq. (3.24) we calculate

$$\Phi(T, \mu, V) = - \sum_i \epsilon_i - k_B T \ln \left[ \prod_i (1 + e^{-2\beta \epsilon_i}) \right] = - \sum_i [\epsilon_i + k_B T \ln(1 + e^{-2\beta \epsilon_i})]. \quad (3.26)$$

Now, by comparing this equation with Eq. (3.23), one finds an expression for the subdivision potential. In principle,  $\Phi_0$  can take any form, since it does not scale with the volume. However, we take the Ansatz proposed in Ref. [8]

$$\Phi(\mu, T, V) = \Phi_c(\mu, T)V + \Phi_0(\mu, T)V/W, \quad (3.27)$$

where  $V$  is the D dimensional volume and  $W$  is the distance between the boundaries, such that the subdivision potential  $\Phi_0$  scales with the boundary of the system and captures its topological properties [8]. This is an important step because it basically states that for long enough systems, the bulk and the boundary can indeed be separated, but for smaller distances the finite-size effects also come into play. By calculating the eigenvalues of the Hamiltonian, a linear fit is used to find the correspondence between Eqs. (3.24) and (3.27), and to obtain the topological behavior in a thermodynamic description.

### 3.4 The topological phase transition for the Kitaev chain

We follow procedure from Sec. 3.3 for the Kitaev chain near an interesting point: the topological phase transition. A phase transition occurs when  $\mu = 2t$ . Therefore, we fix  $t = \Delta$

$=0.25$  while varying  $0.3 \leq \mu \leq 0.7$  with step-size  $\Delta\mu = 0.001$ . To analyze the quantum phase transition, we set  $\beta = 1000$ , which corresponds to a very low temperature, and calculate the grand potential for 50 different lengths in order to make a linear fit ( $\Phi = \Phi_c L + \Phi_0$ ) to extract the coefficients  $\Phi_c$  and  $\Phi_0$ . We indeed observe that the Ansatz 3.27 is only applicable for larger lengths ( $L \approx 200$ ) for values of  $\mu$  far away from the phase transition. Therefore we vary the length between  $200 \leq L \leq 250$  to find a linear model in  $L$  for  $\Phi$ . The results are shown in Fig. 3.8.

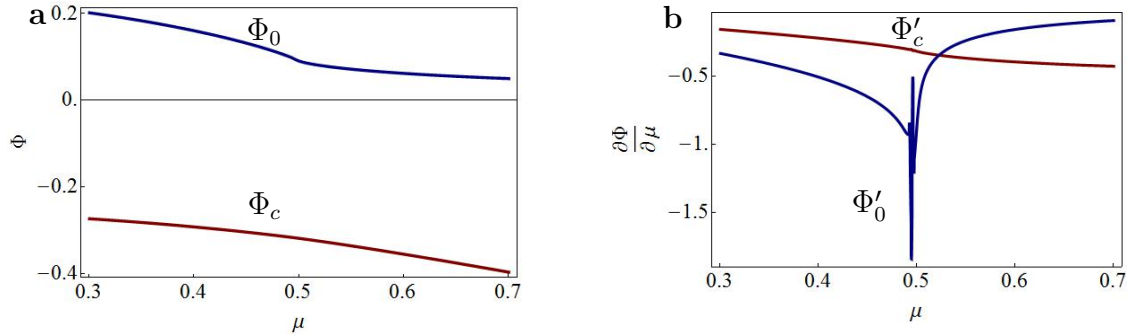


Figure 3.8: The potential  $\Phi$  and subdivision potential  $\Phi_0$  for the Kitaev chain with  $t = \Delta = 0.25$ ,  $200 \leq L \leq 250$ ,  $\beta = 1000$  and  $0.3 \leq \mu \leq 0.7$ . The topological phase transition occurs at  $\mu = 0.5$ . **a** The potential  $\Phi_c$  and the subdivision potential  $\Phi_0$ . **b** The derivatives of  $\Phi_c$  and  $\Phi_0$  with respect to  $\mu$ .

A couple of interesting features of the model can be seen in Fig. 3.8. First of all, although the total grand potential is negative, the subdivision potential is positive. This means the boundary term increases the total energy of the system. Furthermore, at the phase transition  $\mu = 0.5$ , we already see critical behavior for both the subdivision potential  $\Phi_0$  (discontinuous in first derivative) as well as the potential  $\Phi_c$  (kink in the first derivative). However, as can be seen in Fig. 3.9, the linear model fit breaks down near the phase transition. Near the phase transition, the system is more ill-defined and therefore the linear regime of the potential (extensive scaling with the length) is not applicable for these relatively small length scales. Therefore we increase the length between  $0.45 \leq \mu < 0.48$  and  $0.51 < \mu \leq 0.52$  to  $500 \leq L \leq 550$  and for  $0.48 \leq \mu \leq 0.51$  to  $1000 \leq L \leq 1050$  and this indeed increases the accuracy of the linear model. The results are shown in Fig. 3.10.

According to the Ehrenfest classification, we can determine the order of the phase transitions of the potentials by looking at the first discontinuous derivative. In Fig. 3.10, we therefore observe that the order of the phase transition at the boundary is first order, whereas the phase transition in the bulk is second order. This means different thermodynamic variables will behave differently at the bulk than at the boundary, which is something that could be measured.

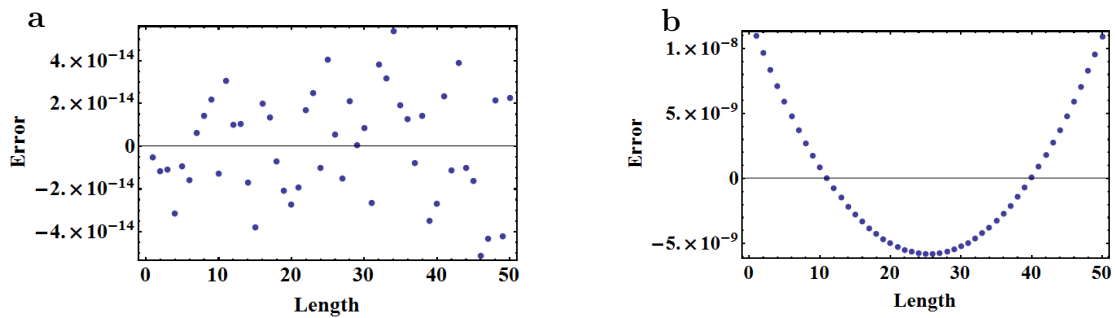


Figure 3.9: Error of the linear model fit for the 50 values of  $L$ . **a** The errors for  $\mu = 0.415$ . **b** The errors for  $\mu = 0.498$ . The error in **a** are numerical errors following from the numerical calculation of the energies, whereas the errors in **b** are structural errors following from the fact that the linear regime is not reached yet for these values of the length due to the critical behavior of the potential near the phase transition.

Next, we verify that the subdivision term indeed arises from the boundary. One insightful way of showing this, is by considering the infinite Kitaev ring, in which we connect the boundaries of the Kitaev chain to each other and we can use the Bloch waves to find the energy of the system. In this way, the contribution of the boundaries is no longer present, since there are now boundaries in the system anymore, which means the subdivision potential should vanish. We showed in Sec. 2.1.2 that the energy of such a system is given by  $\sqrt{(2t \cos(2\pi m/N) + \mu)^2 + 4|\Delta|^2 \sin^2(2\pi m/N)}$ , where  $0 \leq m \leq N - 1$ . We can follow the same procedure as before to obtain the potential and subdivision potential for the Kitaev ring. The results are the dashed lines in Fig. 3.10. Indeed, as expected, we find no subdivision potential, whereas the conventional potential is the same for the Kitaev chain as for the Kitaev ring.

We further note that similar results for the phase transitions are obtained when changing phases in different ways, for example by varying the hopping parameter  $t$  instead of the chemical potential  $\mu$  (not shown), thus indicating that the order of the phase transition is robust to a variation of the parameters driving it.

### 3.5 Conclusion

Taken all together, we have shown in this section that there are different ways to classify a phase transition, the Ehrenfest classification and the Landau classification, and that in the recent years new types of phase transitions were discovered, including the rich quantum phase transitions and topological phase transition. Whereas quantum phase transitions can be identified via symmetry breaking, topological phase transitions cannot be identified in the same manner since there is no broken symmetry. Therefore, to describe topological phase

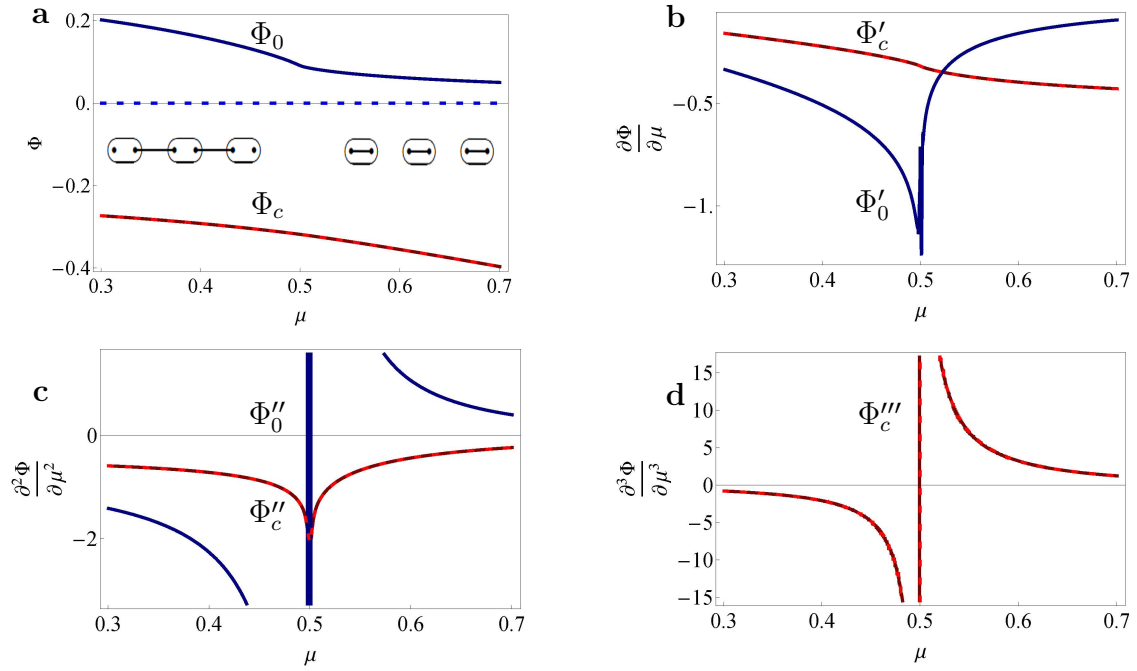


Figure 3.10: Behavior of the thermodynamic potentials and their derivatives for the Kitaev chain. **a** The conventional potential  $\Phi_c$  (red) and subdivision potential  $\Phi_0$  (blue) and **(b, c, d)** their derivatives with respect to  $\mu$  for the Kitaev chain (solid lines) and the Kitaev ring (dashed lines), for  $t = \Delta = 0.25$ . In the thermodynamic limit, the subdivision potential of the Kitaev ring indeed vanishes, whereas the conventional potential does not change. The inset in **a** shows the topological (left) and trivial (right) phase of the Kitaev chain. The phase change occurs at  $\mu = 2t = 0.5$ . **b** The subdivision potential shows a discontinuity in the first derivative, **c** whereas the conventional potential shows a discontinuity in the second derivative. **d** The third derivative is displayed to help the visualization of the discontinuity in the second derivative.

transitions, we make use of the Ehrenfest classification, and with the application of Hill thermodynamics, we can appropriately take the edge states into account in a natural way, where we can separately calculate the bulk and the edge contributions. Furthermore, we find that the phase transition is of a different order: a first-order phase transition at the edge and a second-order phase transition in the bulk. In the next section, we use this formalism to identify the order of the phase transitions for different topological models.

## 4 Classification of topological phase transitions: universalities

In the previous section we have seen how Hill thermodynamics is able to capture a thermodynamic description of the topological phase transition for both the bulk and the boundary in the Kitaev chain. In this section, we apply the procedure described in Sec. 3.3 on different topological models of different Cartan classes in different dimensions  $D$  that we already encountered in Sec. 2.1 and we show that for all these models, we observe the same behavior: a phase transition of order  $D$  at the boundary and one of order  $D + 1$  in the bulk, where  $D$  is the spatial dimension. This can be considered as a new approach in describing these topological phases, which also results in interesting physics, namely universalities. We start with the 1D SSH model, then proceed to the 2D Kane-Mele model and the 2D BHZ model, and finally present the results for the 3D BHZ model.

### 4.1 One dimension

In 1D, we show the results for the SSH model. Together with the results for the Kitaev chain, we observe that for one-dimensional topological models there occurs a first-order phase transition at the edge and a second-order one in the bulk.

#### 4.1.1 Su-Schrieffer-Heeger model

The SSH model is a 1D model, which was first used to describe the dimerization of polyacetylene [73]. It describes electrons hopping between two neighboring sites of a bipartite lattice, and has proven to be an adequate tight-binding model for capturing the behavior of conjugated polymer chains. The SSH Hamiltonian reads

$$H_{\text{SSH}} = \sum_n [t_1 c_{A,n}^\dagger c_{B,n} + t_2 c_{A,n+1}^\dagger c_{B,n} + h.c.], \quad (4.1)$$

where  $t_1$  and  $t_2$  denote unequal hopping amplitudes between the even and odd links for the even (odd) sites  $A$  ( $B$ ). It is common to rewrite  $t_1 = t(1 + \Delta)$  and  $t_2 = t(1 - \Delta)$ , which makes the Hamiltonian only dependent on the parameter  $\Delta$ , and thus there is a phase change between the topological ( $\Delta < 0$ ) and trivial ( $\Delta > 0$ ) phases for  $\Delta = 0$ .

In Fig. 4.1, we show the results for the SSH chain for  $t = 3/2$ . We observe a first-order phase transition at the edge and a second-order phase transition in the bulk, which is the same behavior obtained for the 1D Kitaev chain.

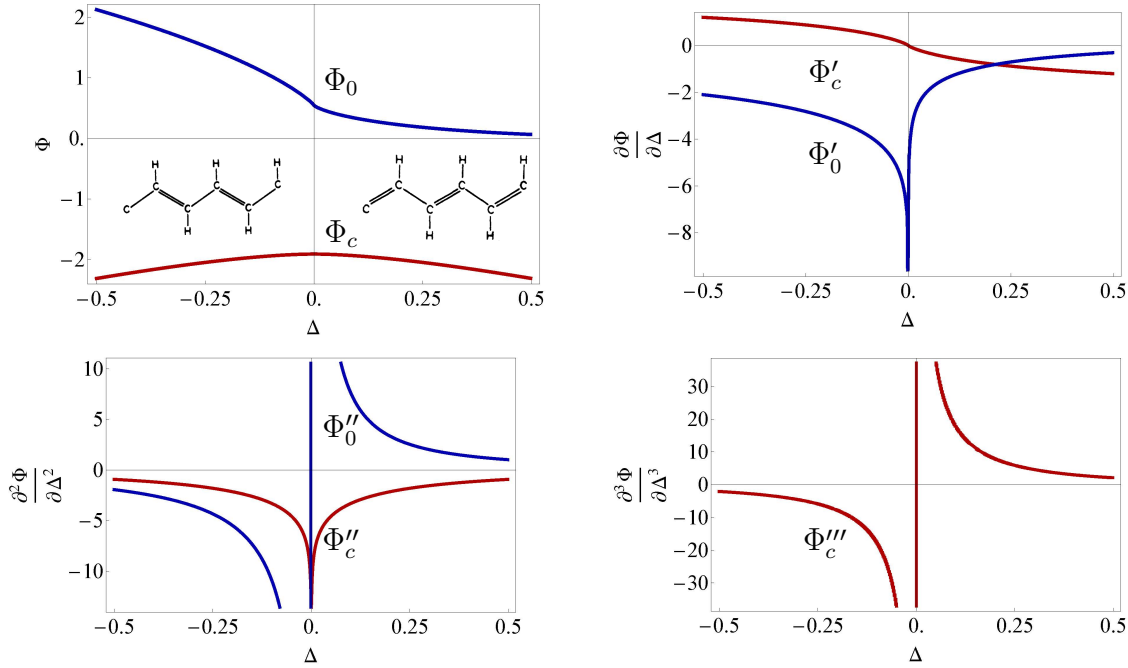


Figure 4.1: Behavior of the thermodynamic potentials and their derivatives for the SSH model. **a** The conventional potential  $\Phi_c$  (red) and subdivision potential  $\Phi_0$  (blue) and **(b, c, d)** their derivatives with respect to  $\Delta$ , for with  $t = 3/2$ . The figures show a similar behavior as the Kitaev chain, a first-order phase transition for the edge and a second-order phase transition in the bulk. The inset in **a** shows the topological (left) and trivial (right) phase of polyacetylene.

## 4.2 Two dimensions

In 2D, we discuss the Kane-Mele model and the 2D BHZ model. The 2D BHZ model was already presented in Quelle et al. [8]. We show a second-order phase transition at the boundary and a third-order one in the bulk.

### 4.2.1 Kane-Mele model

As we have seen in Sec. 2.1.4, the Kane-Mele model is a paradigmatic 2D model to describe graphene in the presence of strong spin-orbit coupling (SOC) [4], see Fig. 2.14. We recall the Hamiltonian

$$H_{\text{KM}} = \sum_{\langle ij \rangle \alpha} t c_{i\alpha}^\dagger c_{j\alpha} + m \sum_i \epsilon_i c_i^\dagger c_i + \sum_{\langle\langle ij \rangle\rangle \alpha\beta} it_2 \nu_{ij} \sigma_{\alpha\beta}^z c_{i\alpha}^\dagger c_{j\beta}, \quad (4.2)$$

where the first term describes the nearest-neighbor hopping with amplitude  $t$ , the second describes a staggered on-site potential  $m$  with opposite signs  $\epsilon_i = \pm 1$  for sublattices  $A$  and  $B$ , and the third describes the intrinsic spin-orbit coupling (SOC), with  $t_2$  the SOC parameter,  $\sigma^z$  a Pauli matrix representing the electron's spin and  $\nu_{ij} = -\nu_{ji} = \pm 1$  describes clock- or

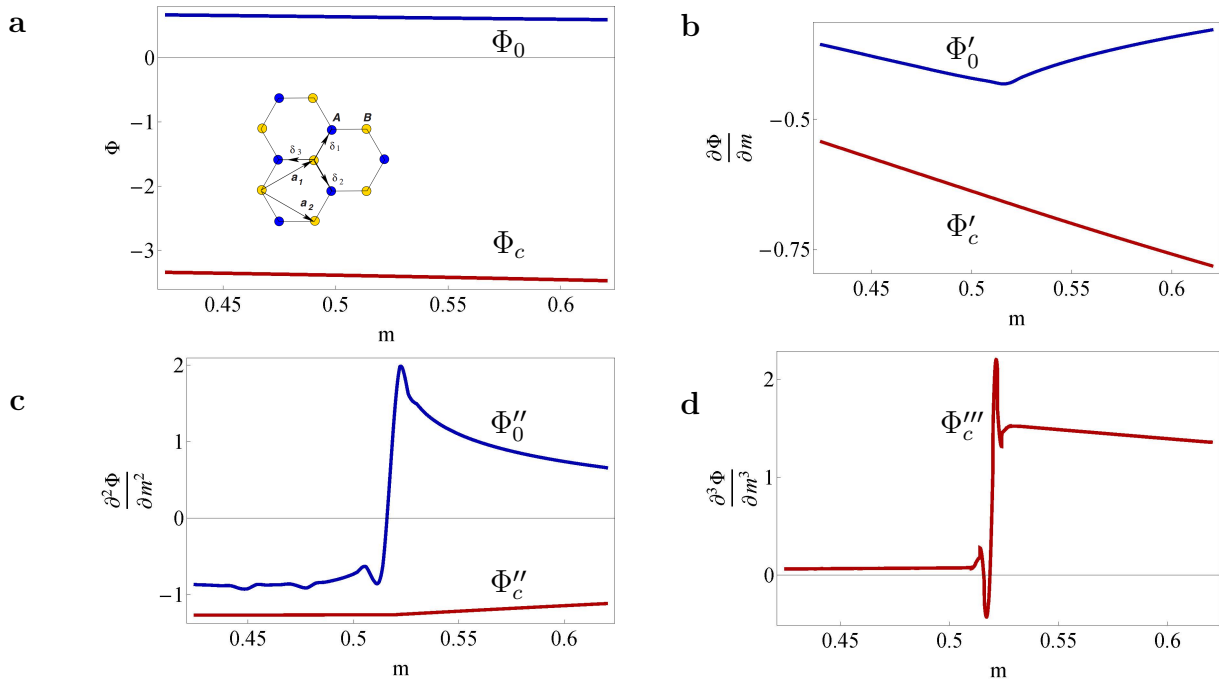


Figure 4.2: Behavior of the thermodynamic potentials and their derivatives for the Kane-Mele model. **a** The conventional potential  $\Phi_c$  (red) and **(b, c, d)** the subdivision potential  $\Phi_0$  (blue) and their derivatives with respect to  $m$  for the Kane-Mele model with  $t = 2t_2 = 0.2$ . The phase change occurs at  $m = 0.52$ . The subdivision potential shows a discontinuity in the second derivative, whereas the conventional potential shows a discontinuity in the third derivative.

counter-clockwise electron hopping. For simplicity, we omit a possible Rashba term. Kane and Mele showed by using this model that graphene with a strong SOC hosts counter-propagating quantized spin currents at the edges of the material (the quantum spin Hall effect). Unfortunately, graphene did not possess these strong intrinsic spin-orbit coupling and therefore it was not able to measure this effect in experiments.

In Fig. 4.2, we display the results for the conventional potential and its derivatives for  $t = 2t_2 = 0.2$  and different values of  $m$ . We observe a second-order phase transition at the edge (Fig. 4.2c) and a third-order one in the bulk (Fig. 4.2d).

#### 4.2.2 Bernevig-Hughes-Zhang model

As discussed in Sec. 2.1.4, the BHZ model is a theoretical model, first proposed to describe the appearance of a quantum spin Hall effect in mercury telluride-cadmium telluride quantum wells, upon tuning the thickness of the quantum well above a critical value [9]. This theoretical prediction was promptly followed by the first experimental observation of this effect in 2007 [11]. Quelle et al. [8] show in this model how Hill thermodynamics can be applied on topological models.

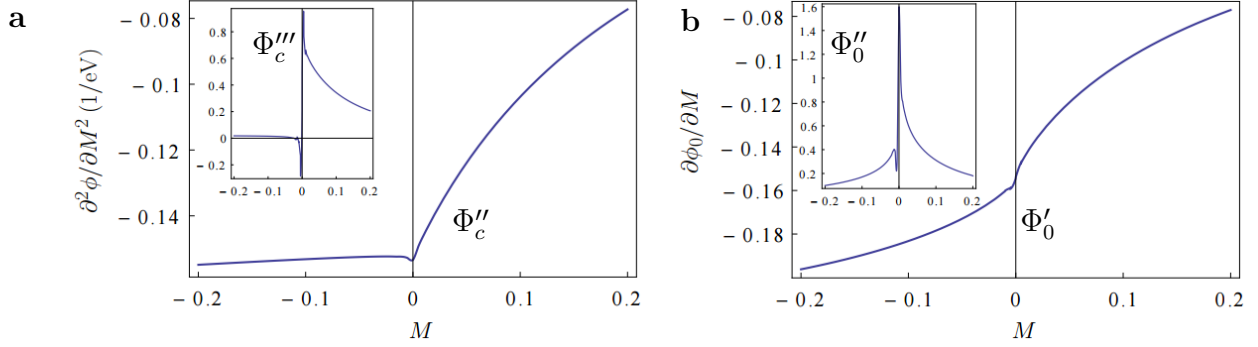


Figure 4.3: **a** The second derivative  $\partial^2\phi/\partial M^2$  is shown as a function of  $M$ . A kink is visible at  $M = 0$ , indicating that the bulk undergoes a third-order phase transition (see the inlay, where the discontinuity in the third derivative is depicted). **b** The first derivative  $\partial\phi_0/\partial M$  is shown as a function of  $M$ . A kink is visible at  $M = 0$  indicating that the edge undergoes a second-order phase transition (the discontinuity in the second derivative is depicted in the inlay), which can be considered the order of the topological phase transition [8].

The Hamiltonian of the 2D BHZ model is given by

$$H_{\text{BHZ, 2D}}(\mathbf{k}) = \epsilon_0(\mathbf{k})\mathbb{1}_{4\times 4} + \begin{pmatrix} M - B\mathbf{k}^2 & A(k_x + ik_y) & 0 & 0 \\ A(k_x - ik_y) & -M + B\mathbf{k}^2 & 0 & 0 \\ 0 & 0 & M - B\mathbf{k}^2 & -A(k_x - ik_y) \\ 0 & 0 & -A(k_x + ik_y) & -M + B\mathbf{k}^2 \end{pmatrix}$$

where  $\mathbf{k}^2 = k_x^2 + k_y^2$  and we decomposed the Hamiltonian for the spin-up electrons (left, above) and the spin-down electrons (right, below) in the two  $2 \times 2$  block matrices. This effective Hamiltonian describes the interactions between the lowest conducting band and the highest valence band of the quantum-well model. In this expression, we did not include the bending  $\epsilon_k \cdot \mathbb{1}$  of each of the bands, since this does not influence the phase transition. The Hamiltonian can be rewritten in a tight-binding description

$$H_{\text{BHZ, 2D}} = A \sin(k_x)\sigma_x - A \sin(k_y)\sigma_y + \{M - 2B[2 - \cos(k_x) - \cos(k_y)]\}\sigma_z, \quad (4.3)$$

where  $k_i$  denotes the momentum in the  $i$ -direction and  $\sigma_i$  are the Pauli matrices. Furthermore, the parameters  $A, B$  and  $M$  denote the thickness of the quantum well, in which the parameter  $M$  denotes the topological ( $M < 0$ ) and trivial ( $M > 0$ ) phase. By Taylor-expanding the  $k_i$  dependencies, we obtain the original Hamiltonian.

Although not known at that time that there were hidden universalities in these topological phases, Quelle et al. already calculated the order of the phase transition. Their results for

$A = B = 1$  are shown in Fig. 4.3. Indeed, there occurs a second-order phase transition at the edge and a third-order one in the bulk.

### 4.3 Three dimensions

In 3D, we only consider the BHZ model due to numerical limitations. We find a third-order phase transition at the edge and a fourth order one in the bulk.

#### 4.3.1 Bernevig-Hughes-Zhang model

Although the BHZ model was originally proposed to describe 2D systems, it has immediately raised the question whether an inversion of bulk bands could also arise in 3D materials, such as  $\text{Bi}_x\text{Sb}_{1-x}$  [43]. The Hamiltonian to describe these 3D models in reciprocal space reads

$$H_{\text{BHZ}}(\mathbf{k}) = \epsilon_0(\mathbf{k})\mathbb{1}_{4 \times 4} + \begin{pmatrix} M(\mathbf{k}) & A_2(k_x + ik_y) & 0 & A_1k_z \\ A_2(k_x - ik_y) & -M(\mathbf{k}) & A_1k_z & 0 \\ 0 & A_1k_z & M(\mathbf{k}) & -A_2(k_x - ik_y) \\ A_1k_z & 0 & -A_2(k_x + ik_y) & -M(\mathbf{k}) \end{pmatrix}, \quad (4.4)$$

where  $\epsilon(\mathbf{k}) = C + D_1k_z^2 + D_2(k_x^2 + k_y^2)$ ,  $M(\mathbf{k}) = M - B_1k_z^2 - B_2(k_x^2 + k_y^2)$  and  $M$ ,  $A_1$ ,  $A_2$ ,  $B_1$ ,  $B_2$ ,  $C$ ,  $D_1$  and  $D_2$  are constant parameters in the model. In the numerical calculations, we set fitting parameters to one and rewrite the matrix into a tight-binding description. In Fig. 4.4, we show the results for the potentials for the 3D BHZ model. The phase transition occurs for  $M = 0$  and is third-order at the edge and fourth-order in the bulk.

### 4.4 Conclusion

All shown models exhibit the same behavior in the order of the dimension: a phase transition of order  $D$  at the boundary and of order  $D + 1$  in the bulk. This is interesting because all models are different in dimension and in Cartan class. The results are all numerical, and therefore it might be fruitful to investigate further whether this can also be done analytically. One way to do this is by finding critical exponents. An idea is to consider the Kitaev chain, which can be mapped to the Ising model [74], and of which the analytic result is well-known. We will come back to this idea in Sec. 6.

A possible interpretation of the universal results, is to see the  $2D$  boundary of a  $3D$  topological material as the  $2D$  bulk of a  $2D$  topological material. In this way, it is only necessary to find the bulk contributions, because the boundary contributions can be considered as the bulk contribution in one lower dimension  $D - 1$ . This is not the same as the conventional bulk-boundary correspondence, because in the correspondence the actual bulk

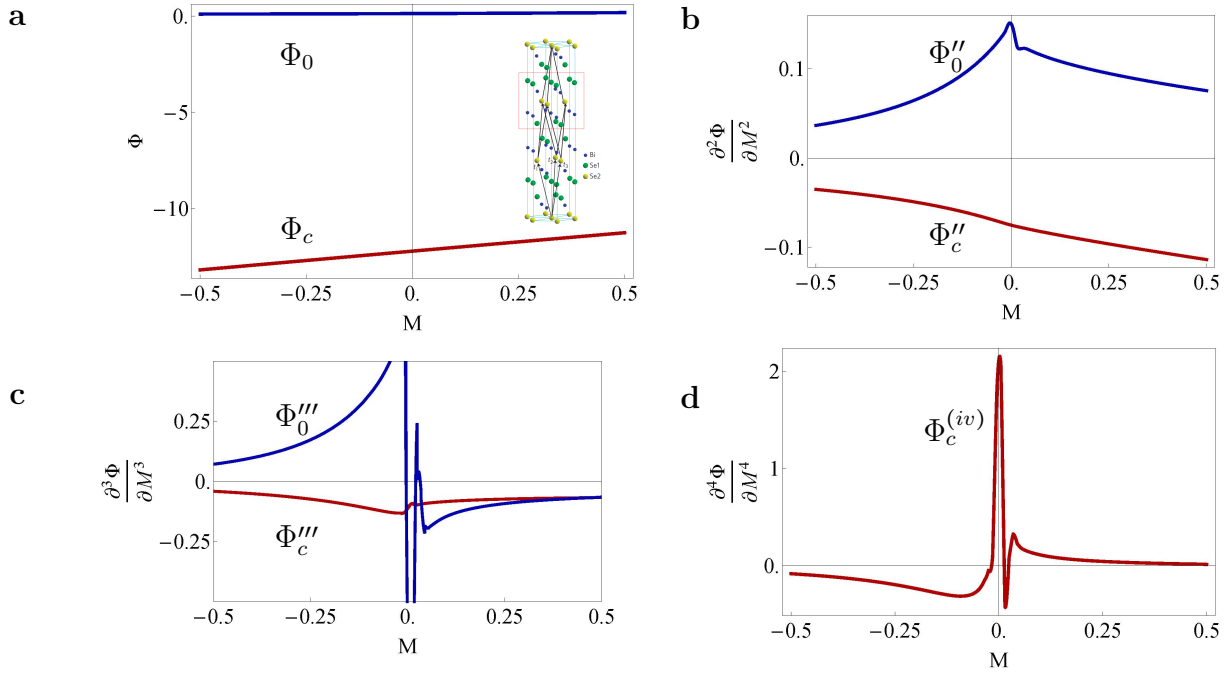


Figure 4.4: Behavior of the thermodynamic potentials and their derivatives for the BHZ model. **a** The conventional potential  $\Phi_c$  (red) and subdivision potential  $\Phi_0$  (blue) and **(b, c, d)** its derivatives with respect to  $M$  for the BHZ model with  $A_1 = A_2 = B_1 = B_2 = C = D_1 = D_2 = 1$ . The phase change occurs at  $M = 0$ . The subdivision potential shows a discontinuity in the third derivative, whereas the conventional potential shows a discontinuity in the fourth derivative. We should note that in **b**  $\Phi_0''$  shows a spurious discontinuity near the phase transition (same for  $\Phi_c'''$  in **c**). Therefore we considered the infinite system and verified that indeed a fourth-order phase transition occurs in the bulk (not shown).

gives information about the properties of the boundary, whereas here we propose to interpret the boundary as a lower dimension bulk.

These results are all at zero-temperature. However, as mentioned previously, the finite-temperature behavior of topological insulators has not been researched frequently yet. Therefore, although the results explicitly show a thermodynamic interpretation on the topological phase change, it is also interesting to heat things up and investigate what happens at finite-temperatures. This is the topic of the next section.

## 5 Finite-temperature effects

Apart from the phase transitions in the previous section, Hill thermodynamics also allows us to investigate thermodynamic variables at finite-temperature, from here on finite- $T$ , via Eq. (3.24). By increasing the temperature, we can calculate all thermodynamic quantities of interest e.g. the entropy and heat capacity.

Why should we study the finite- $T$  behavior of topological phase? One of the most important reasons is because nowadays topological insulators are well understood at zero- $T$ , but their finite- $T$  behavior is still unclear. Does it act like a quantum phase transition or is the behavior different? Furthermore, it is physically not possible to perform experiments at zero temperature, and therefore a finite- $T$  description is needed. Finally, to calculate the finite- $T$  quantities, we can check whether the results make any sense.

Therefore, we analyze the finite- $T$  behavior of topological insulators in this section in order to check our results via the entropy and heat capacity, to find the finite- $T$  topological phase diagram for the Kitaev chain and to calculate measurable quantities such as the heat capacity and density of states in 2D topological insulators. Specifically, we also saw in Sec. 3.1.3 that quantum phase transitions have an interesting finite- $T$  behavior. As mentioned, Viyuela et al. [71] showed recently how to construct the finite- $T$  phase diagram for different topological models. By using Hill thermodynamics, we can compare these results with the ones obtained via the Uhlmann phase and show that they exhibit similar behavior.

In this section, we first zoom in on the Kitaev chain and show the finite- $T$  entropy and compare the heat capacity with the heat capacity of a conformal field theory (CFT) in Sec. 5.1.1. Then, we display the results for the finite- $T$  phase diagram and compare our results with the ones obtained via the Uhlmann phase in Sec. 5.1.2. Finally, we show the heat capacity and the density of states for the 2D BHZ model in Sec. 5.2.1 and calculate these for the Kane-Mele model in Sec. 5.2.2.

### 5.1 Finite-temperature effects in the Kitaev chain

#### 5.1.1 Entropy and heat capacity

From the thermodynamic equation  $d\Phi = -SdT - Nd\mu - pdV$ , we calculate the entropy for the bulk and boundary separately. We present the entropy in Fig. 5.1  $S_i = -\partial\Phi_i/\partial T$ , where  $\Phi_i$  denotes either  $\Phi_c$  (bulk, red solid line) or  $\Phi_0$  (edge, blue dashed line), for different values of  $\mu$ . Especially the entropy at the edge shows an interesting behavior near the phase transition, as it jumps from the initial value  $\log(2)$  in the topological phase towards zero in the trivial phase (Fig. 5.1). For low  $T$ , one would indeed expect this behavior because of the Majorana zero-modes at the edge of the system in the topological phase, each contributing  $1/2\log(2)$ ,

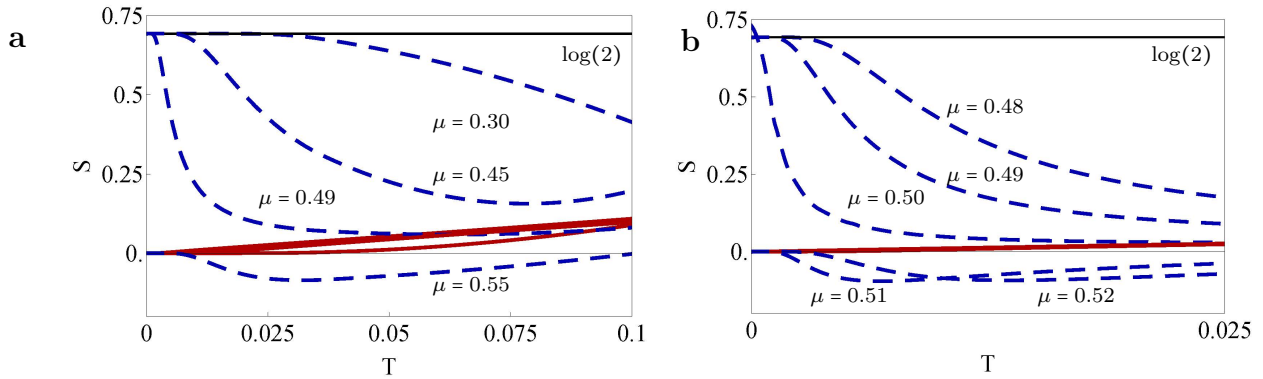


Figure 5.1: **a** Thermal entropy per lattice site in the bulk (red, solid) and at the edge (blue, dashed) for different values of  $\mu = \{0.30, 0.45, 0.49, 0.55\}$ . The other parameters are the same as before. Upon increasing  $\mu$ , the entropy at the edge decreases at lower  $T$  from the zero  $T$  value  $\log(2)$  (black, solid), and suddenly jumps towards zero at the phase transition  $\mu = 0.5$  (see also **b**). The entropy in the bulk becomes a linear function of  $T$  near the phase transition, because the Kitaev chain is conformal at that point. **b** The same as **a**, but now for parameter values  $\mu = \{0.48, 0.49, 0.50, 0.51, 0.52\}$  near the phase transition. The bulk entropy only change little for these parameters.

and the absence of these modes in the trivial phase. At first glance, the negative entropy at the edge in the trivial phase seems peculiar, but it can be understood in the sense that it lowers the total entropy of the whole system. The total entropy is always positive for the considered lengths.

Another interesting thing to note is that at the phase transition,  $\mu = \pm 2t$ , the Kitaev chain is conformal. This means that the Hamiltonian of the Kitaev chain is invariant under conformal transformations, the class of transformations that preserve the angles locally. From the Hamiltonian in Majorana operators in Eq. (2.22), we see that at the phase transition for  $\mu = \pm 2t = \pm 2|\Delta|$ ,  $H = it \sum_j \eta_j \gamma_j \mp \gamma_j \eta_{j+1}$ , which means that the Kitaev chain reduces to a simple chain of Majorana fermions. It is known that for such conformal systems the central charge  $c = 1/2$  [75]. Furthermore, the entropy for a conformal field theory in 1D has a linear  $T$  dependence [76]. Indeed, when we calculate the entropy in the bulk, we observe in Fig. 5.1**b** a linear function of  $T$  at the phase transition. Moreover, the entropy deviates from this linear behavior further away from the phase transition.

Besides the entropy, also the heat capacity  $C_V$  of 1D quantum systems at low  $T$  is proportional to the central charge  $c$ :  $C_V = \pi c k_B^2 T L / (3 \hbar v)$  [76], with  $v$  the velocity of the excitations,  $L$  the length of the system,  $k_B$  the Boltzmann constant and  $\hbar$  the reduced Planck constant. By analyzing the low- $T$  behavior of the Kitaev chain and choosing suitable parameters such that  $k_B / (\hbar v) = 1$ , we indeed find  $C_v = \pi k_B T / 6$  per unit length, see Fig. 5.2.

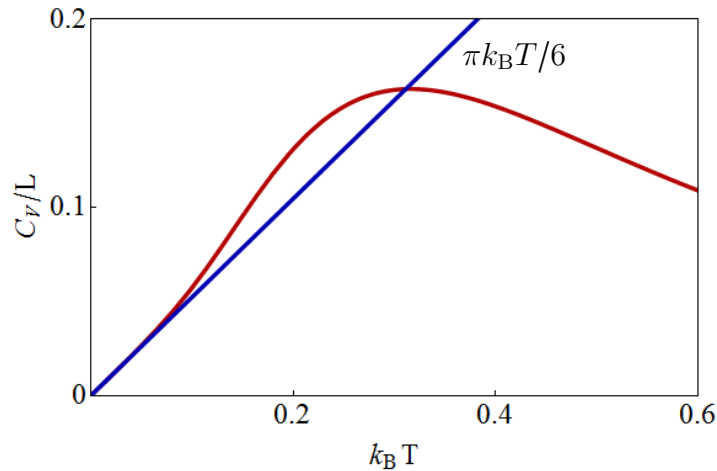


Figure 5.2: Low- $T$  heat capacity (in red) at the phase transition, for  $t = \Delta = 0.25k_B$  (in units where  $k_B/\hbar v = 1$ ). For low  $T$ , we observe a linear  $T$  dependence (in blue) with a slope  $C_V/Lk_B T = \pi/6$ , which corresponds to a central charge  $c = 1/2$ .

### 5.1.2 Finite-temperature phase diagram

Now, we proceed by extending the method to finite  $T$ , aiming at obtaining the complete topological phase diagram. Here we focus on the Kitaev chain, but a similar analysis can be done for the other models. In Fig. 5.3a, we display the discontinuous derivatives of the conventional potential ( $\Phi_c''$ , red) and of the subdivision potential ( $\Phi_0'$ , blue) for different  $T$ , using the same parameters as before. At high  $T$ , the phase transition smooths out, the discontinuity becomes less sharp, and occurs at different values of  $\mu$  than for zero  $T$ . In 5.3b, we show the third derivative of the conventional potential, which always remains at  $\mu = 0.5$ .

As this phase transition smooths out, the question arises what should be indicated as the point of the phase transition. We basically have two options. The first option is to consider the kink in Fig. 5.3a as the point that characterizes the bulk phase transition (the minima of the discontinuous derivative). Then, it is possible to construct a phase diagram for the Kitaev chain as given in Fig. 5.4, where the topological (trivial) phase lies within (outside) the red colored volume. In Sec. 3.1.3, we also mentioned another method to obtain the finite- $T$  phase diagram, by using the Uhlmann phase. In Fig. 5.4, we show the comparison between both methods, and it can be seen that they are very similar. The second option is to consider the point of inflection in Fig. 5.3b, where the “jump” in  $\Phi_c'$  is the largest. This point always remains at  $\mu = 0.5$  and can be identified with the topological invariant Budich and Diehl [77] have in mind. In the upcoming discussion, we elaborate on the current debate about the finite- $T$  behavior of the topological phase diagram, starting with the Uhlmann phase.

The Uhlmann phase is based on the idea that the amplitude for density matrices  $\rho$  is any of

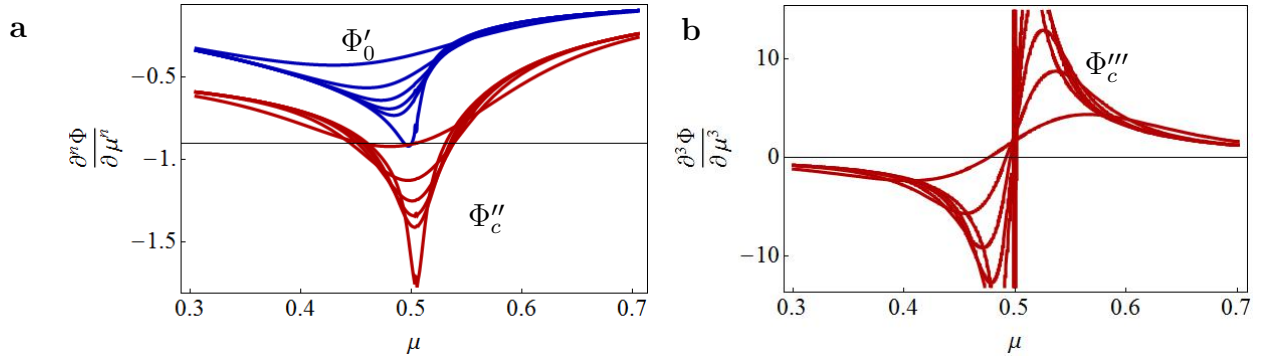


Figure 5.3: Smoothing out of the phase transition at higher  $T$ , for different inverse temperatures  $1/T = \{20, 40, 60, 80, 100, 300\}$  **a** Second derivative ( $n = 2$  on  $y$ -axis) of the conventional potential  $\Phi''_c$  (red) and first derivative ( $n = 1$  on  $y$ -axis) of the subdivision potential  $\Phi'_0$  (blue), with respect to the chemical potential  $\mu$ . For low  $T$ , the phase transition is sharp, but for high  $T$  it smooths out. **b** Third derivative of the conventional potential. When the temperature increases, the phase transition becomes smoothed out, but the inflection point always remains at the phase transition  $\mu = 0.5$ . This indicates that the largest variation in  $\Phi''_c$  is always at the phase transition, which might also indicate the position of the phase transition.

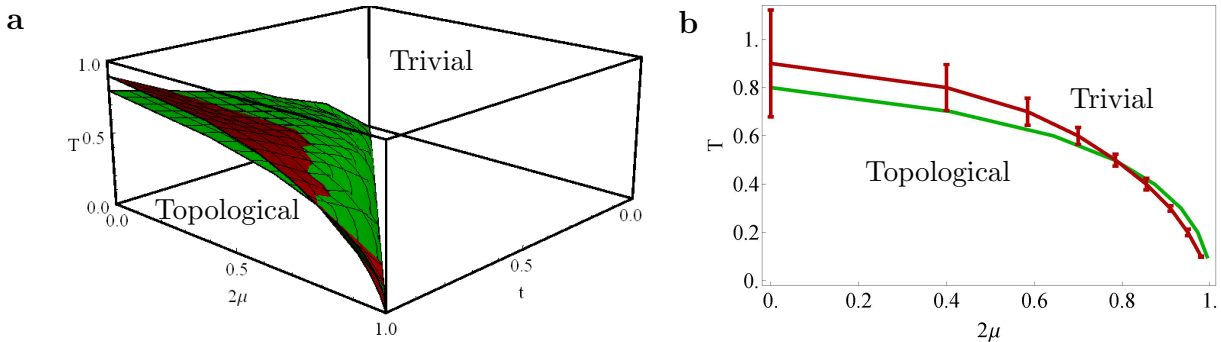


Figure 5.4: **a** Finite- $T$  phase diagram: the results obtained for the bulk phase transition using Hill thermodynamics are displayed in red, whereas the ones arising from the Uhlmann phase are given in green. Here, we use the same parameters as in Ref. [71]. **b** A slice of the topological phase diagram for  $t = 1.0$ , depicting the minima of the second derivative of the conventional potential (red) and the Uhlmann phase (green). The error bars indicate a 0.025% margin of error in identifying the minimum of the conventional potential.

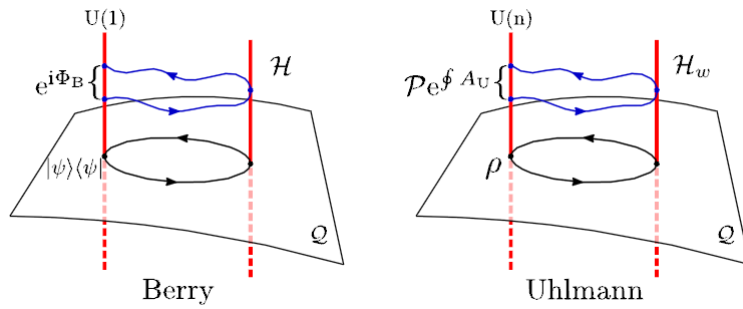


Figure 5.5: The Berry phase in comparison with the Uhlmann phase [71]. The Berry phase uses pure states, which only have a  $U(1)$ -gauge freedom and can be considered to be a special case of the more general  $U(n)$ -gauge freedom of the amplitudes in the Uhlmann phase. After a closed loop  $\gamma$ , a pure state (Berry) carries a simple factor  $\Phi_B = \Phi\gamma$ , whereas a mixed state carries a unitary matrix  $P \exp[\oint_\gamma A_U]$ , where  $A_U = U(T)U^\dagger(T)$  is the Uhlmann connection form.

the matrices  $w$ , such that  $\rho = ww^\dagger$ . In this way, we have a  $U(n)$ -gauge freedom in the choice of  $w$ , where  $n$  is the dimension of the space, instead of the usual  $U(1)$ -gauge freedom for pure states in the Berry phase, see also Fig. 5.5.

More formally, the Uhlmann phase  $\Phi_U^\gamma = \arg \text{Tr}[\rho(0)H_U^\gamma]$  over a loop  $\gamma$  between  $t = 0$  and  $t = T$  in momentum space with the Uhlmann connection  $H_U^\gamma$  and some initial density matrix  $\rho(0)$ , can be considered as an extension of the Berry phase in which mixed states can be described. The Uhlmann connection  $H_U^\gamma = P \exp[\oint_\gamma U(T)U^\dagger(T)]$ , where  $P$  is the path ordering operator and  $U$  is some unitary transformation, defining the parallel transport condition, such that the parallel transport  $w(T) = \sqrt{\rho(T)}U(T)$  of an initial purification  $w = \sqrt{\rho(0)}U(0)$  over a closed loop  $\gamma$  in Hilbert space differs a unitary transformation.

The Uhlmann phase is analogous to the Abelian Berry phase  $\Phi^\gamma = \arg \langle \psi(0) | \psi(T) \rangle$ , where  $|\psi\rangle\langle\psi|$  is a family of pure states, up to one crucial difference [77]: whereas the Berry phase is a  $U(1)$  holonomy and is *additive* in its group structure, which is essential for the construction of the invariant Chern number, the Uhlmann phase is the *trace* of a holonomy, which does not have this property of holonomy, and thus no additive group structure, making the Uhlmann phase winding number not uniquely defined in general. Nevertheless, Viyuela et al. [71] made use of this Uhlmann phase to calculate the finite- $T$  phase diagram for the Kitaev chain and other models. Due to imposed symmetries in the Kitaev chain, only two components of the unit vector  $n_k$  are nonzero, see also Sec. 2.1.2. We recall that the winding number

$$\omega_1 := \frac{1}{2\pi} \oint \left( \frac{\partial_k n_k^i}{n_k^j} \right) dk \quad (5.1)$$

in momentum space, and therefore the Uhlmann phase can be written as

$$\Phi_U^\gamma = \arg \left\{ \cos(\pi\omega_1) \cos \left[ \oint \left( \frac{\partial_k n_k^i}{2n_k^j} \operatorname{sech} \left( \frac{\hbar\omega_k}{2T} \right) dk \right) \right] \right\}, \quad (5.2)$$

where  $\hbar\omega_k$  is the energy spectrum in momentum space (see also Eq. (2.15),  $T$  the temperature and  $i \neq j$ ). For the Kitaev chain, we have already seen the unit vector and the energy spectrum, and these can be used to calculate the Uhlmann phase. In the limit  $T \rightarrow 0$ , the Uhlmann phase in Eq.(5.2) reduces to

$$\Phi_U^{\gamma,0} = \arg \{ \cos(\pi\omega_1) \}, \quad (5.3)$$

which is the standard notion to measure topological order with the winding number.

The finite- $T$   $\mu - t$  phase diagrams obtained using Hill thermodynamics to evaluate the minimum of the discontinuous derivative of the bulk potential (red) or using the Uhlmann phase (green), depicted in Fig. 5.4a, are actually quite similar (see also Fig. 5.4b, where the same results are shown only for a slice of the volume corresponding to  $t = 1.0$ ). The deviations between the two are due to the fact that, at finite  $T$ , it is less obvious to identify the onset of the phase-transition regime, since the peak broadens as  $T$  increases. We include an error bar to the bulk phase-transition points, which indicates the range of the minimum  $+0.025\%$ . The agreement between both descriptions is clear. Note that we only considered the bulk contribution because the Uhlmann phase is also a bulk property.

However, as a response to the Uhlmann phase not being a holonomy, a different topological invariant has been recently proposed in Ref. [77] to describe finite- $T$  topological phase transitions, which does not shift from the zero- $T$  value as  $T$  increases. We would like to point out that the inflection points of  $\Phi_c'''$  (the points corresponding to the largest variation of  $\Phi_c''$ ) always remain at  $\mu = 0.5$ , independently of  $T$ , see also Fig. 5.3b. Although this work does not help to settle the dispute involving finite- $T$  topological invariants, it nevertheless sheds a new light on the problem, by identifying the topological phase transition with a second-order bulk quantum phase transition. From this perspective, it is interesting to observe that the Uhlmann phase captures the smoothing of the phase transition at finite  $T$ , following the expected finite- $T$  behavior of a quantum phase transition [69].

## 5.2 Heat capacity and density of states

By applying the formalism on different topological models, we can calculate any type of thermodynamic variable for the bulk and boundary separately. However, not all of these are interesting, because it is difficult or impossible to measure these quantities in an experiment. Two variables that might be measured are the heat capacity, the response of the system in added or ejected heat upon increasing temperature, and the density of states, potentially measurable via STM (see Sec. 2.2.1). Although it is very difficult to measure these quantities for 2D systems and to separate the bulk and the edge contribution, we can already show what their behavior is in the trivial and topological phase and try to trigger new experiments in the field. We first show the results from Quelle et al. for the 2D BHZ model and then the results for the 2D Kane-Mele model.

### 5.2.1 The Bernevig-Hughes-Zhang model in two dimensions

The density of states  $\text{DOS}_i = -\partial^2 \Phi_i / \partial \mu^2$ , where  $\Phi_i$  denotes either  $\Phi_C$  or  $\Phi_0$ . The results for the 2D BHZ model are shown in Fig. 5.6 for the trivial (**a**) and the topological (**b**) phase at  $T = 0$ . The results for the bulk are shifted upwards by 0.1 and 1 respectively to increase visibility. The DOS behaves exactly as is expected for the BHZ model. The DOS in the bulk

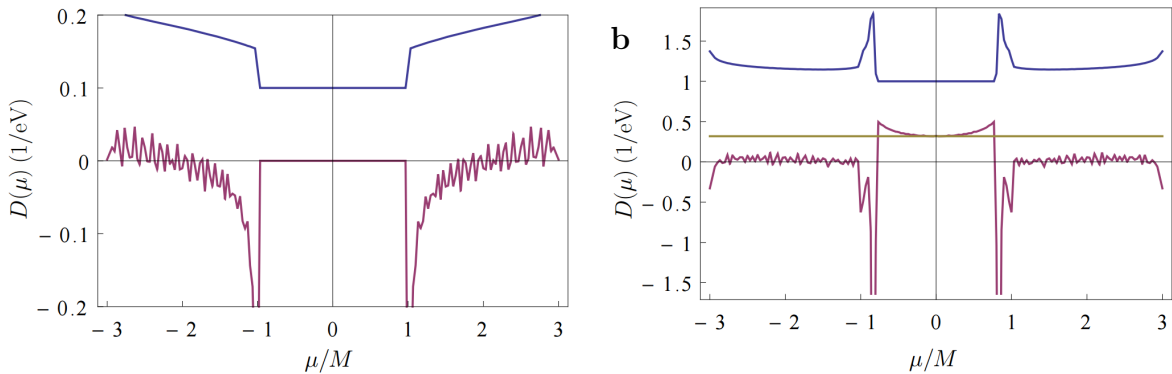


Figure 5.6: The DOS at  $T = 0$  in the trivial (**a**,  $M = 1$ ) and topological (**b**,  $M = -1$ ) phase for  $\mu = 0$ . The bulk contribution per unit width is depicted in blue, and the boundary in red.

(blue) vanishes in both the trivial as in the topological phase in the energy gap  $|\mu| < 1$  and has a nonzero contribution for different energies outside the band gap. In the trivial phase, the DOS in the energy gap is zero, but in the topological phase becomes nonzero due to the presence of the edge states. Outside the energy gap, this contribution drops to zero, which is less visible in the trivial phase due to noise in the numerical calculations.

Interestingly, it is possible to estimate the value of the DOS at the edge by disconnecting the bulk and edge contributions in the Gibbs' sense. The Dirac states in the 2D topological

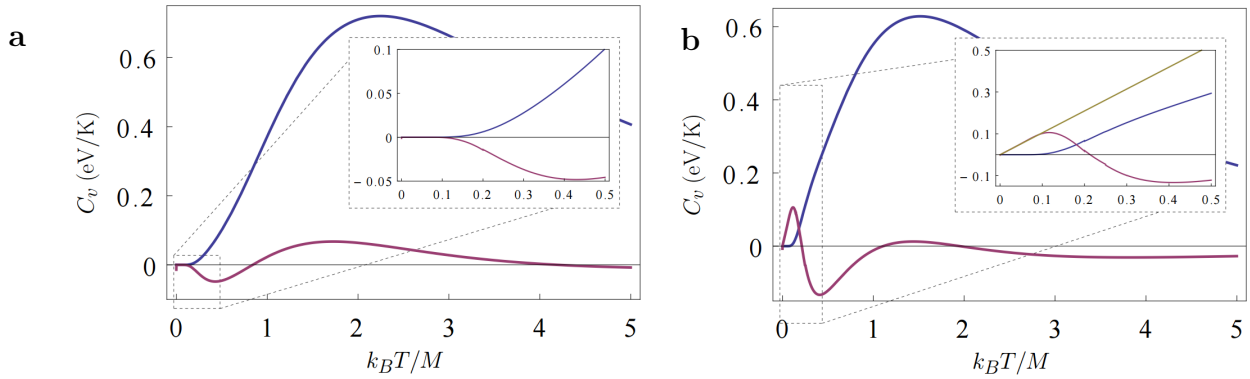


Figure 5.7: The heat capacity in the trivial (**a**,  $M = 1$ ) and topological (**b**,  $M = -1$ ) phase for  $\mu = 0$ . The bulk contribution per unit width is depicted in blue, and the boundary in red.

insulator have a dispersion relation  $E = Ak + \mathcal{O}(k^3)$  [5], where  $A = 1$  is a parameter in the BHZ model. The density of states is related with the total energy via  $N = 2/(2\pi) \int dk = 2/(2\pi) \int \text{DOS}(E)dE$ , where the integral is taken over the 2D disk in momentum space and  $N$  denotes the available energy states. The factor 2 in front is due to spin. By substituting  $dk = dE/A$ , we interpret the factor  $1/(\pi A)$  as the density of states  $\mu = 0$ . The value of  $1/\pi$  ( $A=1$ ) is depicted in yellow in Fig. 5.6b and is indeed the value of the edge state DOS.

The heat capacity  $C_{V,i} = -T\partial^2\Phi_i/\partial T^2$ . We show the  $C_v$  at  $\mu = 0$  in the trivial ( $M = 1$ , Fig. 5.7a) and in the topological ( $M = -1$ , Fig. 5.7b) phase for the bulk (blue) and edge (red) contributions. Surprisingly, the  $C_v$  is not always positive. However, this can be interpreted in a similar way as the entropy, where the total  $C_v$  for the whole system is always positive, but the finite-size effects can be negative in order to decrease the total  $C_V$ . The heat capacity at low temperatures can be understood in comparison with the DOS. For low  $T$  (inset Fig. 5.7,  $C_v = \pi^2 \text{DOS}(E)k_B T/3$  [78]). In the trivial phase, both the contributions for the bulk and boundary are zero because the DOS at  $\mu = 0$  is also zero. However, in the topological phase, the edge contribution  $\text{DOS} = 1/\pi$  and  $C_v = \pi k_B T/3$ , whereas the bulk contribution remains zero. The value  $\pi/3$  is shown in yellow in Fig. 5.7b and indeed shows a linear slope for  $C_v$  at low temperatures.

### 5.2.2 The Kane-Mele model in two dimensions

Finally, we show the DOS and  $C_v$  for the Kane-Mele model in the topological phase and we observe similar behavior as in the BHZ model in Fig. 5.8. The bulk contribution (red) for the DOS at  $T = 0$  is zero in the energy gap, and then jumps to a finite value once the energy is inside the first conduction band  $\mu = 0.52$ . On the other hand, the boundary contribution (blue) is nonzero in the gap and should go to zero in the conduction band. The heat capacity,

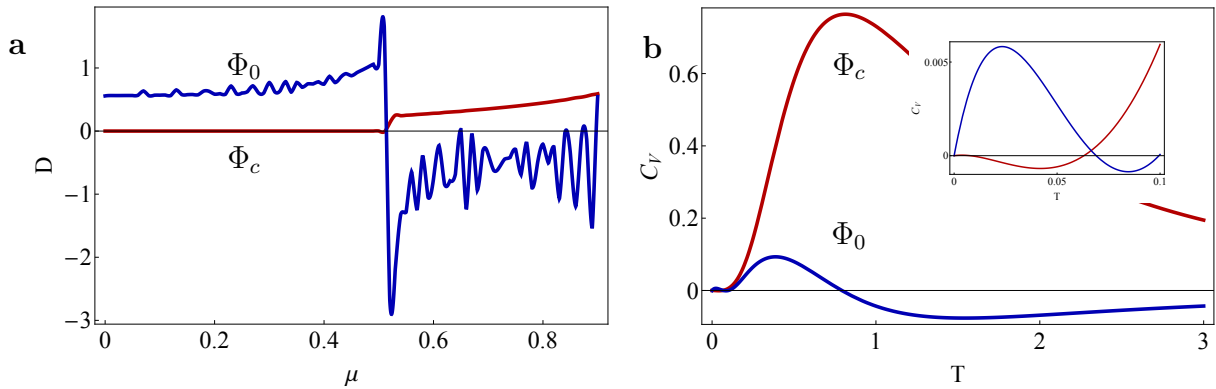


Figure 5.8: Density of states  $\text{DOS}_i = -\partial^2\Phi_i/\partial\mu^2$  and heat capacity  $C_{V,i} = -T\partial^2\Phi_i/\partial T^2$  in the topological phase for  $m = 1$ . **a** At  $T = 0$ , the density of states ( $D$  in the figure) scales with the velocity of the electrons and is zero in the bulk (red) for  $\mu < 0.52$  (before the first conduction band), whereas at the boundary, the density of states should drop to zero after  $\mu = 0.52$  (blue). The noise for the boundary is due to numerical errors. **b** The heat capacity for the bulk (red) and the boundary (blue) for  $\mu = 0$ . The inset shows the details of the low- $T$  behavior. The negative value of the heat capacity should be interpreted as a lower total heat capacity for the whole system. The total heat capacity is always positive.

just as before, is in total positive for the considered lengths, even though the bulk and boundary contributions do not have to be positive. Both the DOS as the heat capacity show a similar behavior for the Kane-Mele model as for the BHZ model.

### 5.3 Conclusion

In the previous section, we have seen how to classify the order of the phase transition in a thermodynamic way and we observed a universal behavior of the order of the phase transition for the bulk and boundary separately. By going to finite-temperatures, we wanted to confirm our results by looking at the entropy and heat capacity of the Kitaev chain, discuss our results for the finite-temperature topological phase transition and compare the results with the one obtained via the Uhlmann phase and to calculate possible measurable quantities.

The entropy and heat capacity show exactly what one would expect by separating the bulk and boundary contributions. The boundary entropy jumps from  $\log(2)$  towards zero at the phase transition and the entropy and heat capacity are a linear function of the temperature at low temperatures because the Kitaev chain is conformal with central charge  $c = 1/2$ .

Next, we showed that the phase transition smooths out for finite-temperatures. By considering the kink in the discontinuous derivative, we were able to construct the finite-temperature topological phase diagram which is comparable with the one obtained via the Uhlmann phase. However, since the Uhlmann phase is not a holonomy, we can also

indicate the biggest jump in the discontinuity as the point of the phase transition, and this always remains at the same parameter value of  $\mu = 2t$ , independent of temperature. This corresponds to the phase transition Budich and Diehl have in mind.

Finally, we calculated the density of states and the heat capacity for  $2D$  topological insulators: the Kane-Mele model and the BHZ model. By interpreting the bulk and the boundary contributions separately, we can also interpret the zero contribution to the density of states in the trivial phase, whereas a nonzero contribution emerges in the topological phase.

The main point of this section is that thermodynamics is able to capture all these important topological features, whereas it has no intrinsic knowledge about these features. The procedure only separates the bulk and the boundary, but does not include any other assumption apart from standard thermodynamics. Surprisingly, it does find all the correct (topological) results and therefore this procedure might be a new way to investigate topological insulators in a well-known framework.

## 6 Conclusion and discussion

Taken together, we have shown two main results in this thesis: Hill thermodynamics is able to identify universalities in topological phase transitions and the analysis can be extended to finite-temperatures. Our results for 1D, 2D and 3D topological models reveal that the phase transition at the edge and bulk of the materials have a different order, and that this order is related to the spatial dimension  $D$  of the quantum model: the edge phase transition is of order  $D$ , whereas the bulk is of order  $D + 1$ . Furthermore, Hill thermodynamics might play a crucial role in understanding topological phase transitions at finite-temperatures. Hill thermodynamics could turn out to be the missing link in understanding these new types of phases in a well-known framework.

In the introduction, we mentioned three aims for this project. The first aim was to unveil the thermodynamic signatures in the Kitaev chain for the Majoranas. The Kitaev chain has been investigated intensively in this thesis and we have shown the zero-temperature phase transition, compared the entropy and heat capacity with the one obtained via conformal field theory and related the finite-temperature phase diagram with the phase diagram derived from the Uhlmann phase. Unfortunately, we are not able yet to describe a new experiment in which Majorana bound-states could be measured, but this is certainly one of the topics that could be thought of as a new project in the future.

The second aim was to use the Hill thermodynamics procedure on different topological models. We have considered five paradigmatic models and showed that the topological phase transition depends on the spatial dimension  $D$  of the model, and this can be considered as a universal result.

The third aim was to extend this procedure towards finite-temperatures. By showing the finite-temperature topological phase diagram, and calculating (measurable) quantities such as the entropy, heat capacity and density of states, we were able to find numerical expressions for these quantities.

Until now, we have focused only on specific topological models, but the “big picture” is still missing. The main question is how we can use this thermodynamic approach to understand topological order in a broader sense. We propose three projects, apart from developing a new method to detect Majorana bound-states, that might help to fill this knowledge gap.

The first project concerns calculating critical exponents. In the recent years, the zero-temperature regime of topological insulators has been investigated thoroughly, and nowadays research has shifted towards finite-temperature and out-of-equilibrium physics.

---

Conveniently, thermodynamics is one of the most profound methods to describe phase transitions at finite temperatures and is capable of predicting out-of-equilibrium behavior. A first interesting project is to investigate the topological phase diagram in more detail and try to obtain (an analogue of) critical exponents. It is often thought that at higher temperatures, the topological phase disappears [79], which agrees with both the analytic Uhlmann phase description and our numerical results. An interesting point is to investigate whether one can find universalities among these topological models. Critical exponents are the key ingredient for these relations. Critical exponents describe the behavior of physical quantities near a continuous phase transition, and this is exactly what occurs in the Kitaev chain in the bulk and in the Kane-Mele and BHZ-model at the boundary. These exponents are universal, which means that they do not depend on the physical details of the system but on features such as the dimension and the range of interaction. Moreover, critical exponents are often measurable quantities via the susceptibility, heat capacity and correlation length. A good starting point is by considering the Kitaev chain. As is well-known, the Kitaev chain can be mapped into the 1D Ising model by switching from a fermionic to a bosonic model [74], thus allowing for further comparison. The critical exponents of the Ising model are well-known and by comparing the two models via e.g. a CFT, we might be able to find an analogue of critical exponents for topological insulators.

The second project focuses on impurities in topological insulators, since topological insulators necessarily come with impurities in an experiment [80]. Bound states, such as Majoranas, form at these impurities in a manner similar to the way that they emerge at the boundary of the system. One reason to investigate impurities is because recently Zhao et al. [81] showed how to use impurities in the 3D topological material  $\text{Sb}_2\text{Te}_3$  to increase the temperature of the emergence of the superconducting condensate to 60K. They claim that their method is one of the possible candidates in the race of finding Majoranas at finite temperatures, and therefore a thermodynamic description of impurities at finite temperature in topological materials is required. Moreover, to trigger new experiments in the field to measure e.g. the heat capacity, we need to be able to give a good account of the real physics in the system, which also involves impurities.

The third project involves a thermodynamic description of two newly developed ways to generate topological phases. Topological phases are usually realized via a strong spin-orbit coupling and are robust to small electron-electron interactions due to the presence of the bulk gap [4, 82]. Recently, two new kinds of topological phases were found, one driven by electron-electron interaction [83], and one driven by engineered dissipation [84, 85]. Interaction driven topological phases, such as the quantum valley Hall effect, are the result of a spontaneously broken time reversal symmetry for each valley in a graphene system. In dissipation driven topological insulators, the topological phases emerge due to a coupling with

an external heat bath, making it possible to describe these phases in terms of the out-of-equilibrium Lindblad master equation. In both cases, our approach seems beneficial because thermodynamics provides a proper description for both strongly interacting and out-of-equilibrium systems.

In my opinion, the work on thermodynamics of topological insulators is just getting started. Due to the importance of topological insulators in quantum computing, Majorana-spotting, and just because these new type of insulators are a very interesting new phase of matter, this technique might turn out to be very useful. Within this thesis, we showed how thermodynamics became one way to describe this hot topic of topological insulators, and I certainly hope a new student continues the work were this thesis ends. As Sir Eddington puts it (see title page), there is no escaping from thermodynamics, not even for topologically protected edge states.

## Acknowledgements

After a year of thermodynamics on this hot topic, this project has come to an end. I am very glad to have been supported by my two excellent supervisors Prof. Dr. Cristiane Morais Smith and Anton Quelle MSc., because of their comments and feedback this work turned into a, hopefully, interesting and novel research tool to study topological insulators. You both learned me a lot about how to put your enthusiasm and knowledge of physics into a research project, how to write proposals, give presentations and how to write an article. I am very thankful for all your help and company during this project. I would also like to thank the research group, with special thanks to Giandomenico Palumbo for his comments on our work. I am looking forward to collaborate with you all in the upcoming years.

Finally, I would also like to thank my family and friends, with a special thanks to Willemijn van Soolingen, who has been there to support my work all the time, and to my fellow Master students. It has been a wonderful year.

---

## 7 Appendix

### Numerics

Two independent calculations were performed to obtain the grand potential for the Kitaev chain, the SSH model and the BHZ model (3D), one in Mathematica and one in C++, and were shown to be exactly the same. In C++, the Eigen package was used to calculate the eigenvalues of the matrices. Due to the unstable behavior of the free energy near the phase transition, we needed to consider larger system sizes in this region to obtain an appropriate linear fit (i.e. a linear fit without systematic errors from finite-size effects). The parameter values for each system are described below (in natural units). All the data is available upon request.

**In the Kitaev chain**, the system sizes vary between  $200 \leq L \leq 250$  for  $0.3 \leq \mu \leq 0.45$  and  $0.55 \leq \mu \leq 0.7$ , between  $1000 \leq L \leq 1050$  for  $0.45 \leq \mu \leq 0.49$  and  $0.51 \leq \mu \leq 0.55$  and  $4000 \leq L \leq 4050$  for  $0.49 \leq \mu \leq 0.51$ . The datapoints are obtained via steps  $\delta\mu = 0.001$ . In the Kitaev ring, all the lengths are  $1000 \leq L \leq 1050$  with  $\delta\mu = 0.002$ . The entropy is obtained with the same parameters for a range of values for  $T$ . For calculating the heat capacity, we used  $L = 4000$  and varied  $T$  in steps of  $\delta T = 0.0001$ . The results for the finite- $T$  phase diagram were obtained for a range of values for  $t < 1.2$  with  $\delta t = 0.2$  at different  $T$  in steps of  $\delta T = 0.05$ , all between length  $200 \leq L \leq 250$  for  $0 \leq 2\mu \leq t$  and  $1000 \leq L \leq 1050$  otherwise.

**In the SSH model**, the system sizes vary between  $200 \leq L \leq 250$  for  $-0.5 \leq \Delta \leq -0.034$  and  $0.006 \leq \Delta \leq 0.50$ , between  $500 \leq L \leq 550$  for  $-0.034 \leq \Delta \leq -0.01$  and  $0.006 \leq \Delta \leq 0.022$  and  $1000 \leq L \leq 1050$  otherwise. The datapoints are obtained in steps of  $\delta\Delta = 0.002$ .

**In the Kane-Mele model**, the system sizes vary between  $600 \leq L \leq 610$  with step size  $\delta\mu = 0.001$  for the free energy. The results for the density of states is obtained for  $400 \leq L \leq 450$  and the heat capacity for  $400 \leq L \leq 450$  and in steps of  $\delta T = 0.05$ .

**In the BHZ model**, the system size  $50 \leq L \leq 60$  for  $-0.5 \leq M < -0.15$  and  $0.25 < M \leq 0.5$  and  $200 \leq L \leq 210$  is smaller than before because these calculations involve large matrices. To obtain the total energy, we summed over the wave vectors  $k_x$  and  $k_y$  for  $2\pi n/n_{max}$ , where  $0 < n \leq n_{max} = 100$ . Furthermore, all parameters, except  $M$ , are set to 1, and we used  $\delta M = 0.01$  as step-size between datapoints.

## References

- [1] L. Landau and E. Lifshitz, *Statistical Physics*. London: Pergamon, 1938.
- [2] L. D. Landau and V. Ginzburg, “On the theory of superconductivity,” *Zh. Eksp. Teor. Fiz.*, vol. 20, p. 1064, 1950.
- [3] K. v. Klitzing, G. Dorda, and M. Pepper, “New Method for High-Accuracy Determination of the Fine-Structure Constant Based on Quantized Hall Resistance,” *Phys. Rev. Lett.*, vol. 45, pp. 494–497, Aug 1980.
- [4] C. L. Kane and E. J. Mele, “ $Z_2$  Topological Order and the Quantum Spin Hall Effect,” *Phys. Rev. Lett.*, vol. 95, p. 146802, Sep 2005.
- [5] M. Z. Hasan and C. L. Kane, “Colloquium : Topological insulators,” *Rev. Mod. Phys.*, vol. 82, pp. 3045–3067, Nov 2010.
- [6] X.-L. Qi and S.-C. Zhang, “Topological insulators and superconductors,” *Rev. Mod. Phys.*, vol. 83, pp. 1057–1110, Oct 2011.
- [7] T. Hill, *Thermodynamics of small systems*. Courier Corporation, 1963.
- [8] A. Quelle, E. Cobanera, and C. Morais Smith, “Thermodynamic signatures of edge states in topological insulators,” *ArXiv e-prints*, Jan. 2016.
- [9] B. A. Bernevig, T. L. Hughes, and S. Zhang, “Quantum Spin Hall Effect and Topological Phase Transition in HgTe Quantum Wells,” *Science*, vol. 314, pp. 1757–, Dec. 2006.
- [10] A. Y. Kitaev, “6. QUANTUM COMPUTING: Unpaired Majorana fermions in quantum wires,” *Physics Uspekhi*, vol. 44, p. 131, Oct. 2001.
- [11] M. König, S. Wiedmann, C. Brüne, A. Roth, H. Buhmann, L. W. Molenkamp, X.-L. Qi, and S.-C. Zhang, “Quantum Spin Hall Insulator State in HgTe Quantum Wells,” *Science*, vol. 318, pp. 766–, Nov. 2007.
- [12] D. Hsieh, D. Qian, L. Wray, Y. Xia, Y. S. Hor, R. Cava, and M. Z. Hasan, “A topological dirac insulator in a quantum spin hall phase,” *Nature*, vol. 452, no. 7190, pp. 970–974, 2008.
- [13] V. Mourik, K. Zuo, S. M. Frolov, S. R. Plissard, E. P. A. M. Bakkers, and L. P. Kouwenhoven, “Signatures of Majorana Fermions in Hybrid Superconductor-Semiconductor Nanowire Devices,” *Science*, vol. 336, pp. 1003–, May 2012.

- [14] S.-Y. Xu, I. Belopolski, N. Alidoust, M. Neupane, G. Bian, C. Zhang, R. Sankar, G. Chang, Z. Yuan, C.-C. Lee, S.-M. Huang, H. Zheng, J. Ma, D. S. Sanchez, B. Wang, A. Bansil, F. Chou, P. P. Shibayev, H. Lin, S. Jia, and M. Z. Hasan, “Discovery of a Weyl fermion semimetal and topological Fermi arcs,” *Science*, vol. 349, no. 6248, pp. 613–617, 2015.
- [15] M. T. Deng, C. L. Yu, G. Y. Huang, M. Larsson, P. Caroff, and H. Q. Xu, “Parity independence of the zero-bias conductance peak in a nanowire based topological superconductor-quantum dot hybrid device,” *Scientific Reports*, vol. 4, p. 7261, Dec. 2014.
- [16] A. Das, Y. Ronen, Y. Most, Y. Oreg, M. Heiblum, and H. Shtrikman, “Zero-bias peaks and splitting in an Al-InAs nanowire topological superconductor as a signature of Majorana fermions,” *Nature Physics*, vol. 8, pp. 887–895, Dec. 2012.
- [17] M. T. Deng, C. L. Yu, G. Y. Huang, M. Larsson, P. Caroff, and H. Q. Xu, “Anomalous Zero-Bias Conductance Peak in a NbInSb NanowireNb Hybrid Device,” *Nano Letters*, vol. 12, no. 12, pp. 6414–6419, 2012. PMID: 23181691.
- [18] H. O. H. Churchill, V. Fatemi, K. Grove-Rasmussen, M. T. Deng, P. Caroff, H. Q. Xu, and C. M. Marcus, “Superconductor-nanowire devices from tunneling to the multichannel regime: Zero-bias oscillations and magnetoconductance crossover,” *Phys. Rev. B*, vol. 87, p. 241401, June 2013.
- [19] E. J. H. Lee, X. Jiang, M. Houzet, R. Aguado, C. M. Lieber, and S. de Franceschi, “Spin-resolved Andreev levels and parity crossings in hybrid superconductor-semiconductor nanostructures,” *Nature Nanotechnology*, vol. 9, pp. 79–84, Jan. 2014.
- [20] R. J. Coolman, “What is Topology?.” <http://www.livescience.com/51307-topology.html>, 2015. [Online; accessed 01-10-2015].
- [21] Nanite, “Band filling diagram.” [https://commons.wikimedia.org/wiki/File:Band\\_filling\\_diagram.svg#](https://commons.wikimedia.org/wiki/File:Band_filling_diagram.svg#), 2013. [Online; accessed 23-10-2015].
- [22] Sbyrnes321, “Hall Effect Measurement Setup For Electrons.” [https://en.wikipedia.org/wiki/File:Hall\\_Effect\\_Measurement\\_Setup\\_for\\_Electrons.png](https://en.wikipedia.org/wiki/File:Hall_Effect_Measurement_Setup_for_Electrons.png), 2012. [Online; accessed 13-11-2015].

- [23] B. Halperin, “Quantum Hall effect: edge states and quantized Hall conductance. Chapter written as a part of the online course Topology in Condensed Matter from the TU Delft .” <http://topocondmat.org/>, 2015. [Online; accessed 13-11-2015].
- [24] T. Ando, Y. Matsumoto, and Y. Uemura, “Theory of Hall Effect in a Two-Dimensional Electron System,” *Journal of the Physical Society of Japan*, vol. 39, no. 2, pp. 279–288, 1975.
- [25] K. von Klitzing, “The quantized hall effect,” *Rev. Mod. Phys.*, vol. 58, pp. 519–531, Jul 1986.
- [26] H. C. Manoharan, “Topological insulators: A romance with many dimensions,” *Nature nanotechnology*, vol. 5, no. 7, pp. 477–479, 2010.
- [27] R. Roy, “Topological phases and the quantum spin hall effect in three dimensions,” *Phys. Rev. B*, vol. 79, p. 195322, May 2009.
- [28] A. P. Schnyder, S. Ryu, A. Furusaki, and A. W. W. Ludwig, “Classification of topological insulators and superconductors in three spatial dimensions,” *Phys. Rev. B*, vol. 78, p. 195125, Nov 2008.
- [29] A. Kitaev, “Periodic table for topological insulators and superconductors,” *AIP Conference Proceedings*, vol. 1134, no. 1, 2009.
- [30] Stoof, H.T.C. and Gubbels, K.B. and Dickerscheid, D.B.M., *Ultracold quantum fields*, vol. 1. Springer Berlin, 2009.
- [31] S. Ryu, A. P. Schnyder, A. Furusaki, and A. W. W. Ludwig, “Topological insulators and superconductors: tenfold way and dimensional hierarchy,” *New Journal of Physics*, vol. 12, p. 065010, June 2010.
- [32] F. von Oppen, Y. Peng, and F. Pientka, “Topological superconducting phases in one dimension,”
- [33] D. J. Thouless, M. Kohmoto, M. P. Nightingale, and M. den Nijs, “Quantized hall conductance in a two-dimensional periodic potential,” *Phys. Rev. Lett.*, vol. 49, pp. 405–408, Aug 1982.
- [34] M. Nakahara, *Geometry, topology and physics*. CRC Press, 2003.
- [35] F. D. M. Haldane, “Model for a quantum hall effect without landau levels: Condensed-matter realization of the ”parity anomaly”,” *Phys. Rev. Lett.*, vol. 61, pp. 2015–2018, Oct 1988.

- [36] A. H. Castro Neto, F. Guinea, N. M. R. Peres, K. S. Novoselov, and A. K. Geim, “The electronic properties of graphene,” *Rev. Mod. Phys.*, vol. 81, pp. 109–162, Jan 2009.
- [37] J. E. Moore, “The birth of topological insulators,” *Nature*, vol. 464, no. 7286, pp. 194–198, 2010.
- [38] E. G. Novik, A. Pfeuffer-Jeschke, T. Jungwirth, V. Latussek, C. R. Becker, G. Landwehr, H. Buhmann, and L. W. Molenkamp, “Band structure of semimagnetic  $\text{Hg}_{1-y}\text{Mn}_y\text{Te}$  quantum wells,” *Phys. Rev. B*, vol. 72, p. 035321, Jul 2005.
- [39] A. Pfeuffer-Jeschke, “Ph.d. thesis,” 2000.
- [40] L. Fu, C. L. Kane, and E. J. Mele, “Topological insulators in three dimensions,” *Phys. Rev. Lett.*, vol. 98, p. 106803, Mar 2007.
- [41] J. E. Moore and L. Balents, “Topological invariants of time-reversal-invariant band structures,” *Phys. Rev. B*, vol. 75, p. 121306, Mar 2007.
- [42] L. Fu and C. L. Kane, “Topological insulators with inversion symmetry,” *Phys. Rev. B*, vol. 76, p. 045302, Jul 2007.
- [43] H. Zhang, C.-X. Liu, X.-L. Qi, X. Dai, Z. Fang, and S.-C. Zhang, “Topological insulators in  $\text{Bi}_2\text{Se}_3$ ,  $\text{Bi}_2\text{Te}_3$  and  $\text{Sb}_2\text{Te}_3$  with a single Dirac cone on the surface,” *Nature physics*, vol. 5, no. 6, pp. 438–442, 2009.
- [44] A. Altland and M. R. Zirnbauer, “Nonstandard symmetry classes in mesoscopic normal-superconducting hybrid structures,” *Phys. Rev. B*, vol. 55, pp. 1142–1161, Jan 1997.
- [45] R.-J. Slager, A. Mesaros, V. Juričić, and J. Zaanen, “The space group classification of topological band-insulators,” *Nature Physics*, vol. 9, no. 2, pp. 98–102, 2013.
- [46] O. Fischer, M. Kugler, I. Maggio-Aprile, C. Berthod, and C. Renner, “Scanning tunneling spectroscopy of high-temperature superconductors,” *Rev. Mod. Phys.*, vol. 79, pp. 353–419, Mar 2007.
- [47] I. Giaever, “Energy Gap in Superconductors Measured by Electron Tunneling,” *Phys. Rev. Lett.*, vol. 5, pp. 147–148, Aug 1960.
- [48] G. Binnig, H. Rohrer, C. Gerber, and E. Weibel, “Surface studies by scanning tunneling microscopy,” *Phys. Rev. Lett.*, vol. 49, no. 1, p. 57, 1982.
- [49] G. Binnig, H. Rohrer, C. Gerber, and E. Weibel, “Tunneling through a controllable vacuum gap,” *Applied Physics Letters*, vol. 40, no. 2, pp. 178–180, 1982.

- 
- [50] N. de Jeu, “Theoretical studies of Scanning Tunneling Microscopy of high-Tc superconductors,” Master’s thesis, Utrecht University, the Netherlands, 2007.
- [51] C. Renner and O. Fischer, “Vacuum tunneling spectroscopy and asymmetric density of states of  $\text{Bi}_2\text{Sr}_2\text{CaCu}_2\text{O}_{8+\delta}$ ,” *Phys. Rev. B*, vol. 51, pp. 9208–9218, Apr 1995.
- [52] P. Roushan, J. Seo, C. V. Parker, Y. Hor, D. Hsieh, D. Qian, A. Richardella, M. Z. Hasan, R. Cava, and A. Yazdani, “Topological surface states protected from backscattering by chiral spin texture,” *Nature*, vol. 460, no. 7259, pp. 1106–1109, 2009.
- [53] T. Zhang, P. Cheng, X. Chen, J.-F. Jia, X. Ma, K. He, L. Wang, H. Zhang, X. Dai, Z. Fang, X. Xie, and Q.-K. Xue, “Experimental demonstration of topological surface states protected by time-reversal symmetry,” *Phys. Rev. Lett.*, vol. 103, p. 266803, Dec 2009.
- [54] Z. Alpichshev, J. G. Analytis, J.-H. Chu, I. R. Fisher, Y. L. Chen, Z. X. Shen, A. Fang, and A. Kapitulnik, “Stm imaging of electronic waves on the surface of  $\text{Bi}_2\text{Te}_3$ : Topologically protected surface states and hexagonal warping effects,” *Phys. Rev. Lett.*, vol. 104, p. 016401, Jan 2010.
- [55] K. K. Gomes, W. Ko, W. Mar, Y. Chen, Z.-X. Shen, and H. C. Manoharan, “Quantum Imaging of Topologically Unpaired Spin-Polarized Dirac Fermions,” *ArXiv e-prints*, Sept. 2009.
- [56] D. Culcer, “Transport in three-dimensional topological insulators: Theory and experiment,” *Physica E Low-Dimensional Systems and Nanostructures*, vol. 44, pp. 860–884, Feb. 2012.
- [57] D. W. Lynch and C. G. Olson, *Photoemission studies of high-temperature superconductors*, vol. 5. Cambridge University Press, 2005.
- [58] A. Damascelli, Z. Hussain, and Z.-X. Shen, “Angle-resolved photoemission studies of the cuprate superconductors,” *Rev. Mod. Phys.*, vol. 75, pp. 473–541, Apr 2003.
- [59] Y. Xia, D. Qian, D. Hsieh, L. Wray, A. Pal, H. Lin, A. Bansil, D. Grauer, Y. Hor, R. Cava, *et al.*, “Observation of a large-gap topological-insulator class with a single dirac cone on the surface,” *Nature Physics*, vol. 5, no. 6, pp. 398–402, 2009.
- [60] Y. Chen, J. Analytis, J.-H. Chu, Z. Liu, S.-K. Mo, X.-L. Qi, H. Zhang, D. Lu, X. Dai, Z. Fang, *et al.*, “Experimental realization of a three-dimensional topological insulator,  $\text{Bi}_2\text{Te}_3$ ,” *Science*, vol. 325, no. 5937, pp. 178–181, 2009.
- [61] D. Hsieh, Y. Xia, D. Qian, L. Wray, F. Meier, J. Dil, J. Osterwalder, L. Patthey, A. Fedorov, H. Lin, *et al.*, “Observation of time-reversal-protected single-dirac-cone

## REFERENCES

---

- topological-insulator states in bi 2 te 3 and sb 2 te 3,” *Physical review letters*, vol. 103, no. 14, p. 146401, 2009.
- [62] H. Kamerlingh Onnes, “The liquefaction of helium,” *KNAW Proceedings*, vol. 11, pp. 168–185, 1909.
- [63] L. I. Dana and H. Kamerlingh Onnes, “Further Experiments with Liquid Helium A. Preliminary Determinations of the Latent Heat of Vaporization of Liquid Helium,” *Communications from the Physical Laboratory of the University of Leiden*, no. 179c, 1926.
- [64] M. Wolfke and W. H. Keesom, “On the Change of the Dielectric Constant of Liquid Helium with the Temperature. Provisional Measurements,” *Communications from the Physical Laboratory of the University of Leiden*, no. 190a, 1927.
- [65] W. H. Keesom and M. Wolfke, “Two Different Liquid States of Helium,” *Verhandlungen der Koninklijke Akademie van Wetenschappen*, no. 190b, 1928.
- [66] W. Keesom and A. Keesom, “On the anomaly in the specific heat of liquid helium,” *Communications from the Physical Laboratory of the University of Leiden*, no. 221d, 1932.
- [67] G. Jaeger, “The Ehrenfest Classification of Phase Transitions: Introduction and Evolution,” *Archive for History of Exact Sciences*, vol. 53, no. 1, pp. 51–81, 1998.
- [68] S. Blundell and K. M. Blundell, *Concepts in thermal physics*. Oxford: Oxford University Press, 2010.
- [69] S. Sachdev, *Quantum Phase Transitions*. Cambridge University Press, 2011.
- [70] X.-L. Qi and S.-C. Zhang, “The quantum spin Hall effect and topological insulators,” *Physics Today*, vol. 63, no. 1, p. 33, 2010.
- [71] O. Viyuela, A. Rivas, and M. A. Martin-Delgado, “Uhlmann Phase as a Topological Measure for One-Dimensional Fermion Systems,” *Phys. Rev. Lett.*, vol. 112, p. 130401, Apr. 2014.
- [72] O. Viyuela, A. Rivas, and M. A. Martin-Delgado, “Two-dimensional density-matrix topological fermionic phases: Topological uhlmann numbers,” *Phys. Rev. Lett.*, vol. 113, p. 076408, Aug 2014.
- [73] W. P. Su, J. R. Schrieffer, and A. J. Heeger, “Solitons in polyacetylene,” *Phys. Rev. Lett.*, vol. 42, pp. 1698–1701, Jun 1979.
- [74] M. Greiter, V. Schnells, and R. Thomale, “The 1D Ising model and the topological phase of the Kitaev chain,” *Annals of Physics*, vol. 351, pp. 1026–1033, Dec. 2014.

- [75] A. Dutta, G. Aeppli, B. Chakrabarti, U. Divakaran, T. Rosenbaum, and D. Sen, *Quantum Phase Transitions in Transverse Field Models*. Cambridge University Press, 2015.
- [76] E. Fradkin, *Field theories of condensed matter physics*. Cambridge University Press, 2013.
- [77] J. C. Budich and S. Diehl, “Topology of density matrices,” *Phys. Rev. B*, vol. 91, p. 165140, Apr 2015.
- [78] C. Kittel, *Introduction to Solid State Physics*. Wiley, 2004.
- [79] O. Viyuela, A. Rivas, and M. Martin-Delgado, “Symmetry-protected topological phases at finite temperature,” *2D Materials*, vol. 2, no. 3, p. 034006, 2015.
- [80] S.-Q. Shen, *Topological Insulators: Dirac Equation in Condensed Matters*, vol. 174. Springer Science & Business Media, 2013.
- [81] L. Zhao, H. Deng, I. Korzhovska, J. Secor, M. Begliarbekov, Z. Chen, E. Andrade, E. Rosenthal, A. Pasupathy, V. Oganessian, and L. Krusin-Elbaum, “Emergent surface superconductivity of nanosized Dirac puddles in a topological insulator,” *ArXiv e-prints*, Aug. 2014.
- [82] C. L. Kane and E. J. Mele, “Quantum Spin Hall Effect in Graphene,” *Phys. Rev. Lett.*, vol. 95, p. 226801, Nov 2005.
- [83] E. C. Marino, L. O. Nascimento, V. S. Alves, and C. Morais Smith, “Interaction Induced Quantum Valley Hall Effect in Graphene,” *Phys. Rev. X*, vol. 5, p. 011040, Mar 2015.
- [84] S. Diehl, E. Rico, M. A. Baranov, and P. Zoller, “Topology by dissipation in atomic quantum wires,” *Nature Physics*, vol. 7, no. 12, pp. 971–977, 2011.
- [85] C.-E. Bardyn, M. A. Baranov, C. V. Kraus, E. Rico, A. mamolu, P. Zoller, and S. Diehl, “Topology by dissipation,” *New Journal of Physics*, vol. 15, no. 8, p. 085001, 2013.